Utilising High Work Function Metal Oxides as Hole Extracting Layers for Organic Photovoltaic Cells

A thesis submitted for the degree of

**Doctor of Philosophy**

at the University of Warwick

by

Ian Hancox

Supervised by Prof. Tim S. Jones

Department of Chemistry

University of Warwick, Coventry
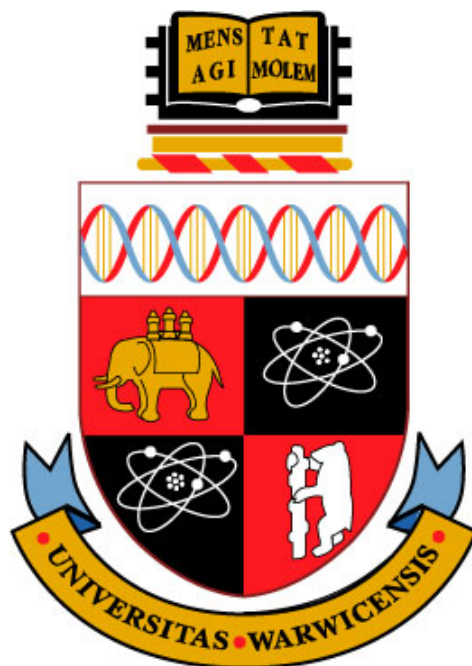
March 2013

Abstract

A substantial amount of research has already been undertaken towards creating commercially viable organic photovoltaics (OPVs). This is due to the potential use of OPV cells as an inexpensive source of renewable energy. There are many factors to consider in OPV cell design, including photo-active materials, cell architecture and electrode selection. However, additional interlayers for use between the photo-active materials and the electrodes were identified to be as important and need to be developed to optimise cell performance. The work presented here focuses on the influence of various metal oxide hole extracting layers in different OPV systems.

Metal oxides such as molybdenum oxide (MoO_x) have shown great promise in polymer cells as a hole extracting layer, and here we investigate their use in small molecule cells. An optimised MoO_x layer thickness of 5 nm provides a ~ 60 % increase in overall power conversion efficiency (η_p) for chloroaluminium phthalocyanine (ClAlPc) / fullerene (C_{60}) cells in comparison to those fabricated on bare ITO. A similar improvement of η_p is reported when using the MoO_x layer in a boron subphthalocyanine chloride (SubPc) / C_{60} system. For both high ionisation potential donor materials, the cells containing MoO_x achieve a significantly higher open circuit voltage (V_{oc}). Conversely, cells utilising the lower ionisation potential donor materials such as copper phthalocyanine (CuPc) and pentacene produce similar V_{oc} values when deposited on both ITO and MoO_x. Hence, the η_p is marginally reduced with the MoO_x layer. To attain a deeper understanding, the factors behind these performance differences were explored by UV-vis absorption spectroscopy, ultra-violet photoemission spectroscopy (UPS), X-ray diffraction (XRD) and atomic force microscopy (AFM).

Thermally evaporated vanadium oxide (V_2O_x) was used as an alternative hole extracting layer to MoO_x, achieving analogous performance to MoO_x when used in SubPc / C_{60} and CuPc / C_{60} cells. The electronic properties of the V_2O_x layer are investigated using UPS, and it is demonstrated to have substoichiometric n-type character in contrast to the p-type behaviour previously reported. Additionally, the *in-situ* fabrication and characterisation of organic layers using UPS indicate Fermi level pinning of the organic to the metal oxide.

A solution processed vanadium oxide ($V_2O_{x(sol)}$) layer was developed and characterised as an alternative method of layer fabrication. The atmospheric processing conditions are found to have a dramatic effect on cell performance, and are studied using x-ray photoelectron spectroscopy (XPS). Layers spin-coated under a nitrogen atmosphere exhibit a larger composition of V^{4+} states. Kelvin probe and UPS experiments indicate the $V_2O_{x(sol)}$ is also a high work function, n-type layer, with the $V_2O_{x(sol)}$ hole extracting layer producing similar cell performance to the thermally evaporated metal oxide layers. Cells deposited on the $V_2O_{x(sol)}$ layer demonstrate good operational stability characteristics, outperforming a commonly used solution processable hole extracting layer.

Table of contents

Declaration

The experimental work presented here on in was conducted by myself between August 2008 and August 2012, with exception of the experiments detailed below. The XRD measurements in Chapter 3 were taken by Luke Rochford on samples I had prepared. Subsequent analysis was done by myself. UPS measurements throughout were taken by or with the assistance of Luke Rochford, with analysis performed by myself. XPS data in Chapter 5 was obtained by Dr Marc Walker and James Mudd in the Department of Physics, University of Warwick. Sample preparation and analysis was performed by myself.

I can confirm that none of this work has previously been submitted for a higher degree.

Acknowledgements

I firstly would like to thank Prof. Tim Jones, for the fantastic opportunity to do this work in an interesting field. He has given me many opportunities other PhD students do not get and I appreciate this. I am thankful for Tim's support, advice and patience for putting up with my pestering. I would also like to thank all the members of staff at the Department of Chemistry for all the work they did to make the PhD project run smoothly.

I thank the Engineering and Physical Sciences Research Council (EPSRC) and Asylum Research UK for the project funding. I would also like to personally thank Dr Chris Mulcahy, Dr Mick Phillips and Dr Amir Moshar from Asylum for their help and knowledge. I look forward to working with Chris and Mick on our future projects together.

The Tim Jones group have all been great to work with and made long experiments bearable. All the Tim Jones group members deserve a sincere thank you, Paul, Stefan, Luke, Dave, Nicola, Chloe, Nat, Gavin, Edd, Tom, Raff, V, Jay, Mark, Tomasz and of course George. I would particularly like to thank Dr Paul Sullivan for his numerous proofreads of papers and my thesis, in addition to his advice in experimental disasters! I thank Luke Rochford for the XRD and UPS help, in addition to many funny conversations. I would like to thank Dr Stefan Schumann for both his scientific input to the group, his advice and for the good times we had at numerous conferences.

Life would not be the same without football, so thanks goes out to the Chemistry and Biology footballers throughout the years for providing all the times I didn't run around much. I have to thank Wolverhampton Wanderers for the 'entertainment', providing many highs and an equally as many lows. Thanks to Steve Pickerall for having to suffer with me, and doing so into the future.

My parents, Nigel and Anita, deserve more thanks than I could ever give them. They have provided unconditional love, advice and financial support throughout my existence. I could not achieved any of this without them. I would also like to thank Graham for his brotherly love and all the fun we have had. A massive thanks also goes to Tina and Tim for their love and support.

Finally, I thank Sally, who has had to put up with me on a daily basis throughout my PhD. She has helped me through the lows and been there for the highs. I love you Sally, and thank you for your love back! I look forward to our future together.

List of publications

Publications:

- **I. Hancox**, K. V. Chauhan, P. Sullivan, R. A. Hatton, A. Moshar, C. P. A. Mulcahy and T. S. Jones, *Increased efficiency of chloroaluminium phthalocyanine (ClAlPc)/fullerene (C_{60}) photovoltaic cells by insertion of a MoO_3 hole-extracting layer,* **Energy Environ. Sci**., 2010, **3**, 107 - 110.

- **I. Hancox**, P. Sullivan, K.V. Chauhan, N. Beaumont, L.A. Rochford, R.A. Hatton and T.S. Jones, *The effect of a MoO_x hole-extracting layer on the performance of organic photovoltaic cells based on small molecule planar heterojunctions,* **Organic Electronics**, 2010, **11**, 2019-2025.

- Paul Sullivan, Amelie Duraud, **Ian Hancox**, Nicola Beaumont, Giorgio Mirri, James H.R. Tucker, Ross A. Hatton, Michael Shipman, Tim S. Jones, *Halogenated Boron Subphthalocyanines as Light Harvesting Electron Acceptors in Organic Photovoltaics,* **Advanced Energy Materials**, 2011, **1**, 352.

- N. Beaumont, **I. Hancox**, P. Sullivan, R. A. Hatton and T. S. Jones, *Increased efficiency in small molecule organic photovoltaic cells through electrode modification with self-assembled monolayers,* **Energy Environ. Sci**., 2011, **4**, 1708-1711.

- **I. Hancox**, L. A. Rochford, D. Clare, P. Sullivan, and T. S. Jones, *Utilising n-type vanadium oxide films as hole-extracting layers for small molecule organic photovoltaics,* **Applied Physics Letters**, 2011, **99**, 013304.

- J. L. Yang, P. Sullivan, S. Schumann, **I. Hancox** and T. S. Jones, *Organic photovoltaic cells based on unconventional electron donor fullerene and electron acceptor copper hexadecafluorophthalocyanine,* **Applied Physics Letters**, 2012, **100**, 023307.

- Yunhua Chen, Samuel T. Jones, **Ian Hancox**, Richard Beanland, Edward J. Tunnah, and Stefan A. F. Bon, *Multiple Hydrogen-Bond Array Reinforced Cellular Polymer Films from Colloidal Crystalline Assemblies of Soft Latex Particles,* **ACS Macro. Lett.**, 2012, **1**, 603–608.

- **I. Hancox**, L.A. Rochford, D. Clare, M. Walker, J. J. Mudd, P. Sullivan, S. Schumann, C.F. McConville, T. S. Jones, *Optimisation of a High Work Function Solution Processed Vanadium Oxide Hole-Extracting Layer for Small Molecule and Polymer Organic Photovoltaic Cells,* **Journal of Physical Chemistry C**, 2013, **117**, 49-57.

Presentations:

- SID Organic Electronics UK 2009 (Imperial College London) - poster

- MRS fall 2009 (Boston) - poster

- CMMP 2009 (Warwick) - talk

- Bristol Nanoscience symposium 2010 - poster

- MRS fall 2010 (Boston) - poster

- ISSC - 18 (Warwick) - poster

- Postgraduate Research Symposium 2011 (Warwick) - talk

- Asylum Research User meeting (Edinburgh) - talk

- SID Organic Electronics UK 2011 (Imperial College London) - talk

Researcher ID:

http://www.researcherid.com/rid/D-9504-2011

List of abbreviations

General abbreviations

a-Si   Amorphous silicon

AC   Alternating Contact

AFM   Atomic Force Microscopy

AM   Air Mass

C-AFM   Conductive-Atomic Force Microscopy

c-Si   Crystalline silicon

D / A   Donor / acceptor

DSSC   Dye Sensitised Solar cell

HOMO   Highest Occupied Molecular Orbital

HOPG   Highly Ordered Pyrolytic Graphite

ICT   Integer Charge Transfer

IPES   Inverse Photoemission Spectroscopy

KP   Kelvin Probe

LUMO   Lowest Unoccupied Molecular Orbital

MIS   Metal-Insulator-Semiconductor

(O)LED   (Organic) Light Emitting Diode

OMBD   Organic Molecular Beam Deposition

(O)PV   (Organic) Photovoltaic

QCM   Quartz Crystal Microbalance

pc-Si   Polycrystalline silicon

PLD   Pulsed Laser Deposition

R2R   Roll-to-roll

SAM   Self Assembled Monolayer

UPS   Ultra-Violet Photoemission Spectroscopy

UV   Ultra-Violet

XPS   X-ray Photoelectron Spectroscopy

XRD   X-ray Diffraction

List of symbols and chemicals

Physical quantities and parameters

α	Absorption Coefficient
A	Absorption
c	Concentration
CB	Conduction Band
D	Exciton Diffusion Coefficient
d_{hkl}	Interplanar Spacing
ε	Molar Absorption Coefficient
E_{ABE}	Additional Binding Energy
E_B	Binding Energy
E_{EA}	Electron Affinity
E_f	Fermi Level
E_g	Band Gap
E_{ICT+}	Positive Integer Charge Transfer State Energy
E_{ICT-}	Negative Integer Charge Transfer State Energy
E_{IP}	Ionisation Potential
E_{KE}	Kinetic Energy
EQE	External Quantum Efficiency (measurement)
$\eta_{(A,ED,CT,CC)}$	Quantum Efficiency (of Absorption, Exciton Diffusion, Exciton Dissociation, Charge Collection)

η_{EQE}	External quantum efficiency
η_p	Power Conversion Efficiency
$f_{(E)}$	Fermi-Dirac Population Distribution
FF	Fill Factor
I	Light Intensity
I_o	Incident Light Intensity
J_m	Current Density at Maximum Power Point
J_{sc}	Short Circuit Current Densities
$J\text{-}V$	Current Density - Voltage
k_B	Boltzmann Constant
L	Path Length
L	Thickness
L_D	Exciton Diffusion Length
n	Order of Reflection
$N(\lambda)$	Monochromatic Incident Photon Flux Density
Φ	Work Function
P_{inc}	Incident Power Density
P_m	Maximum Power Point
q	Elementary Charge
r_B	Bohr Radius
r_c	Coulombic Potential Well
R_l	Load Resistance

R_q	Surface Roughness
R_s	Series Resistance
R_{sh}	Shunt Resistance
τ	Exciton Lifetime
T	Transmittance
$T80\ (T50)$	Shelf Life Time to 80 (50) % Remaining Performance
V_b	Backing Potential
VB	Valence Band
V_{bi}	Built-in Field
V_c	Capacitor Potential
V_{CPD}	Contact Potential Difference
V_l	Vacuum Level
V_m	Voltage at Maximum Power Point
V_{oc}	Open Circuit Voltage

Chemicals

Ag	Silver
Al	Aluminium
Au	Gold
BCP	Bathocuproine
CdTe	Cadmium Telluride
ClAlPc	Chloroaluminium Phthalocyanine
Cl_6-SubPc	Hexachloro Boron Subphthalocyanine Chloride
Cs_2CO_3	Caesium carbonate
Cs_2O	Caesium oxide
CuPc	Copper Phthalocyanine
F8BT	Poly[(9,9-di-*n*-octylfluorenyl-2,7-diyl)-*alt*-(benzo[2,1,3]thiadiazol-4,8-diyl)]
GaAs	Gallium Arsenide
H2TPP	Tetraphenylporphine
IPA	Isopropanol
InGaAs	Indium gallium arsenide
InGaP	Indium gallium phoshide
ITO	Indium Tin Oxide
LiF	Lithium Fluoride
MDMO-PPV	Poly(2-methoxy-5-(3',7'-dimethyloctyloxy)-*p*-phenylene vinylene)
MEH-PPV	Poly(2-methoxy-5-(2'-ethyl-hexyloxy)-1,4-phenylene vinylene

MoO$_x$ Molybdenum Oxide

N$_2$ Nitrogen

NiO   Nickel Oxide

P3HT   Poly(3-hexylthiophene)

PCBM   Phenyl-C61-butyric Acid Methyl Ester

PEDOT   Poly(3,4-ethylenedioxithiophene)

PSS   Polystyrene Sulfonic Acid

PTCBI   3,4,9,10-perylenetetracarboxylic bis-benzimidazole

PTCDA   Perylene-3,4,9,10-tetracarboxylic Dianhydride

SubPc   Boron Subphthalocyanine Chloride

TiO$_2$ Titanium dioxide

V$_2$O$_x$ Vanadium Oxide

V$_2$O$_{x(sol)}$ Solution Processed Vanadium Oxide

V$_2$O$_{x(sol,N2,N2)}$ Solution Processed Vanadium Oxide Under Stated Conditions

ZnO   Zinc Oxide

ZnPc   Zinc Phthalocyanine

Chapter 1: Introduction

1.1 Why develop photovoltaic cells?

As the world population expands, the demand for energy also increases. This is especially apparent in the large developing nations such as China and India, where high demand for energy is due to industrialisation, to build infrastructure and provide extended transportation networks.

The burning of fossil fuels is the most commonly used method of large scale energy generation worldwide. Fossil fuel sources are extracted from below the surface of Earth and include coal, oil and gas. Additional energy generation is often obtained from nuclear power.

However, the generation of energy from fossil fuels has several considerable drawbacks. We cannot solely rely on fossil fuels in the future, since there is a dwindling supply. Additionally, the burning of fossil fuels results in the release of significant quantities of CO_2 into the Earth's atmosphere. Fossil fuels are thought to be a major contributor to the greenhouse effect. It is believed that the greenhouse effect is impacting on Earth as global warming, leading to climate change and rising sea levels.[1] Energy production using fossil fuels has suffered further adverse publicity due to the considerable destruction of natural habitats caused by incidents such as the Deepwater Horizon oil spill, and loss of human life at the Texas City refinery fire. The use of nuclear power has been impacted by the Fukushima Daiichi disaster. This has also led to a negative public perception of nuclear energy generation.

The governments of developed countries are consequently facing increasing pressure politically, environmentally and economically to reduce energy consumption. Further pressure has focussed on the need to extend supply from renewable sources of energy. Renewable energy sources currently available include wind, wave, geothermal and solar.

Solar in particular shows great promise thanks to a range of interesting design concepts, from hot water panels for heating to direct electricity generation using photovoltaics (PV). PV panels can be used to provide electricity to medium size grids, remote locations and even in space. The sun predictably bathes the Earth with 10,000 times more energy than our current usage. Thus, utilising only a 10 % efficient PV cell, we would only need to cover around ~ 0.1 % of the Earth's surface in order to meet our demand. A further influence behind the growth of PV development is the relatively easy installation of panels, with many new buildings incorporating them into design plans. Hence, PVs offer the possibility of large scale energy generation in close proximity to the user with little maintenance and silent function, without necessarily the need for extensive grid supplies and land usage.

1.2 Inorganic photovoltaic cells

The PV effect was initially discovered in 1839 by Bequerel. Despite this, it was not until the mid 1940's that silicon based PV cells started to be heavily developed.[2] Currently, the majority of commercially available PV cells are based around inorganic photo-active materials. By p-n doping highly crystalline silicon (c-Si) cells have reached power conversion efficiencies (η_P) of ~ 25 %, with long operational lifetimes. PV cells based on c-Si have large energy requirements for

fabrication, leading to them being perceived as long term investments. Lower cost and higher throughput amorphous (a-Si) and polycrystalline silicon (pc-Si) PV cells have been developed to counter this, however the cell η_p suffers, with 13.7 % achieved for a-Si in a triple junction architecture.
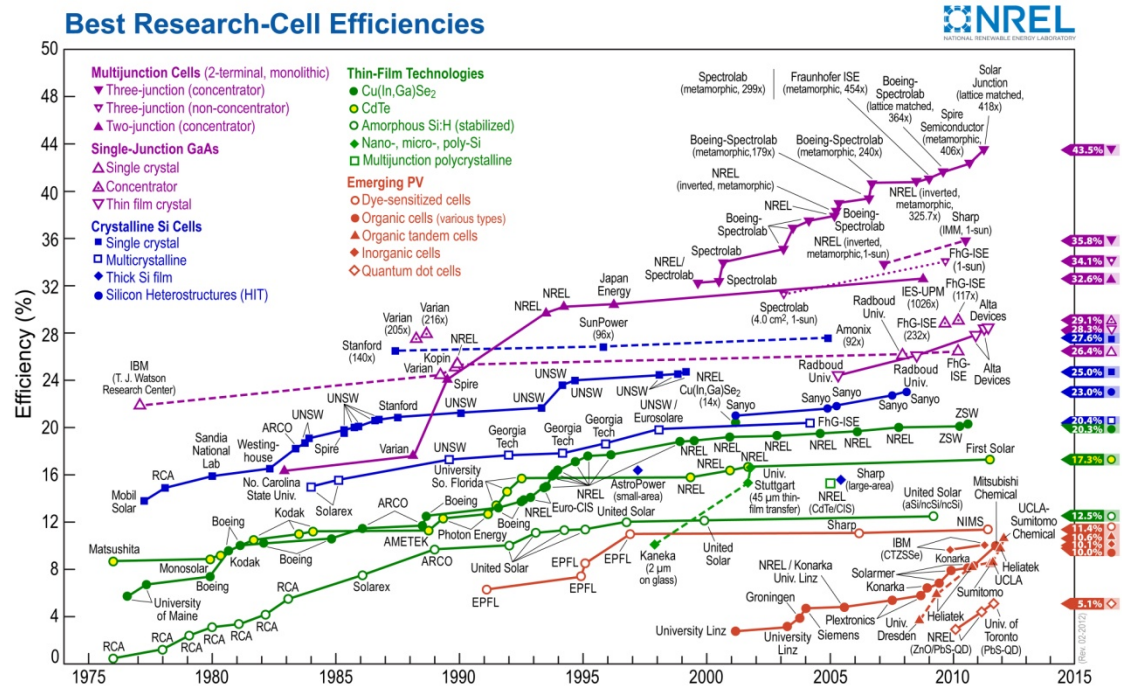
Figure 1.1: PV laboratory technology progression over time, up to the beginning of 2012.[3]

Other inorganic materials have been utilised in PV cells, with the progression of various technologies shown in Figure 1.1. These include II-VI and III-V semiconductors such as cadmium telluride (CdTe) and gallium arsenide (GaAs), achieving a η_p of 17.3 and 28.2 % respectively. Additionally, triple junction cells of complementary absorbing materials such as indium gallium phosphide (InGaP), GaAs and indium gallium arsenide (InGaAs) have been shown to produce record η_p values of 43.5 % under 418 sun concentrated sunlight.[4] However, many of these

materials have low abundance, are toxic or are too expensive in terms of cost per Watt to be useful beyond specialist needs.

For more general commercial use, electricity from PVs needs to be relatively inexpensive. This requires cells to approach the low cost of fossil fuels and nuclear power, with an easily scalable production. Hence, another PV technology based around organic photo-active layers has emerged as a potential alternative to inorganic PV cells.

1.3 Organic photovoltaics

1.3.1 Types of organic photovoltaic cells

Organic photovoltaics (OPVs) are often referred to as excitonic solar cells and can be divided into several categories: dye sensitised solar cells (DSSCs or Graetzel cells), small molecules, polymer and hybrid organic / inorganic solar cells. DSSCs contain organic based dye sensitizers and a transition metal oxide, typically nano-crystalline TiO_2, allowing efficient charge transfer. The organic dye is reduced by an electrolyte, which in turn is reduced by the counter electrode.[5] These cells have achieved 11.4 % efficiency,[6] however further research is needed to replace the liquid electrolyte to create an efficient solid state cell.[7]

In this work, the focus will be on small molecule and polymer / small molecule cells and unless stated otherwise, these are the systems being referred to by the abbreviation OPVs.

The OPV research field is continually growing due to the extraordinary industrial possibilities of the cells. In a commercial process it should be possible to

deposit the photo-active organic materials onto flexible substrates. Fabrication could use either, or a combination of, solution and vacuum processing techniques. This will allow for high throughput roll-to-roll (R2R) production. These organic layers are inexpensive in both material and the energy costs of processing compared to inorganic PV, and scalable to large areas. Additionally, the cells are ultra-thin and very light, with substantially reduced energy payback times compared to other PV technologies. Energy payback is a key factor for low cost production and the use of OPV cells in niche applications. Espinosa *et al.* modelled the production of OPV cells with payback times as low as one day.[8]

1.3.2 A brief history of OPV cells

The first OPV cells were made as early as 1959 and consisted of single crystals of anthracene, displaying very low efficiencies.[9] Initial OPV studies placed a single organic layer between two electrodes of different work functions, leading to typical cell efficiencies of ~ 0.01 %. The cell performance was improved using a merocyanine dye in a metal-insulator-semiconductor (MIS) Schottky barrier configuration, achieving an efficiency of 0.7 %.[10] The excitons produced in these photo-active layers were only able to dissociate into a hole and electron in the depletion region very close to the electrode, or at traps within the organic layer. This, combined with the transportation of both of the charges through the same organic layer, led to a substantial charge recombination and so low cell fill factors (*FF*). Consequently cell performance was poor.

In 1986 a considerable breakthrough occurred for OPV cells, with Tang's discovery of the donor / acceptor (D / A) bilayer structure.[11] Taking inspiration from the inorganic p-n type PV cells, Tang used discrete layers of copper phthalocyanine (CuPc) as an electron donor material and the perylene derivative 3,4,9,10-

perylenetetracarboxylic bis-benzimidazole (PTCBI) as an electron acceptor material. The cell exhibited a performance of 0.95 %, with both organic layers contributing to current generation. The energy offset between the donor and acceptor materials provided a favourable interface for exciton dissociation, followed by hole and electron transport through the CuPc and PTCBI layers respectively. This new heterojunction cell architecture vastly reduced the recombination of excitons and charge build-up compared to single layer OPV cells. Furthermore, a considerable increase in *FF* was achieved.

Following Tang's discovery, large improvements in OPV cell efficiencies have been achieved with changes to donor and acceptor material selection. The PTCBI acceptor has been replaced with C_{60}, discovered by Kroto in 1985,[12] which led to a cell performance of 3.6 %.[13] This was mainly attributed to the larger exciton diffusion length (L_D) of C_{60} (~ 40 nm) compared to PTCBI, in addition to a more complementary absorption profile. Also, the CuPc layer has been substituted for many different materials with a wide range of electronic properties and L_D values. These donor materials include various phthalocyanines and anthracenes, used in combination with the C_{60} acceptor.[14-18] Furthermore, phthalocyanines have also been used as acceptors.[19, 20] Indeed, Sullivan *et al.* have recently reported work replacing the C_{60} with a hexachloro boron subphthalocyanine chloride (Cl_6SubPc) acceptor. The boron subphthalocyanine chloride (SubPc) / Cl_6SubPc system demonstrates a similar performance to SubPc / C_{60} cells, but with an increased open-circuit voltage (V_{oc}) and cell stability.[21]

The bottleneck of the discrete bilayer structure is the relatively short L_D of the commonly used materials, limiting the cell to thin organic layers with low light absorption. This results in low current generation and consequently poor cell

performance. The current generation of cells can be improved by intermixing the donor and acceptor materials to form what is commonly known as a bulk heterojunction structure. Bulk heterojunction small molecule cells have been reported by Sullivan *et al.* and Uchida *et al.,* where co-deposition of CuPc and C_{60} in 1 : 1 ratios facilitated increased short circuit current densities (J_{sc}) compared to bilayer cells. However, a concomitant reduction in *FF* and V_{oc} was reported in both cases.[22, 23] Whilst co-deposition allows for improved exciton dissociation due to a larger D / A interfacial area, the V_{oc} of the cell is reduced. This is caused by increased charge recombination due to the restricted charge transport pathways to the electrodes. However, Sullivan *et al.* showed greatly improved cell performance by employing a novel combination of discrete CuPc and C_{60} layers close to the respective electrodes. Between the discrete layers three compositional ratios of bulk heterojunctions were co-deposited sequentially. This allowed improved charge collection efficiency, therefore eliminating losses in both V_{oc} and *FF*.

Another method of improving cell performance is to use multi-junction cell architectures, which stack two (tandem) or more bilayer cells on top of each other in a series connection. This architecture was first demonstrated by Hiramoto *et al.*[24] Tandem structures typically use two subcells with complementary absorption profiles to cover a wider range of wavelengths for better coverage of the solar spectrum. Tandem cells rely on excellent current matching of the subcells for optimum performance. Carefully current balanced cells achieve *FF* and J_{sc} values similar to that of the individual subcells, with the V_{oc} of the tandem cells obtained from the sum of the subcell values, thus enhancing the cell performance. Xue *et al.* achieved efficiencies of 5.7 % with a tandem cell using two subcells of bulk heterojunction CuPc / C_{60}.[25] Cheyns *et al.* clearly demonstrated that the

complementary absorption of two subcells in a tandem cell can increase the performance by 40 % over single cells, resulting in a cell efficiency of 5.15 %.[26] The significance of tandem architectures towards commercialisation of small molecule OPV cells was illustrated by Heliatek, who revealed in April 2012 a 1.1 cm^2 tandem OPV cell with a record efficiency of 10.7 %.[27]

Whilst small molecule cells are typically fabricated under high vacuum, polymer : fullerene blends are commonly processed from solution. The first solution processed bulk heterojunction architecture polymer : fullerenes cells were reported in 1995 by Yu *et al.* and Halls *et al.*[28, 29] Yu *et al.* presented a spin cast blend of a poly(2-methoxy-5-(2'-ethyl-hexyloxy)-1,4-phenylene vinylene (MEH-PPV) donor and a soluble C$_{60}$ derivative phenyl-C61-butyric acid methyl ester (PCBM) acceptor, to form a dense network of donor and acceptor material. With the development of new polymer donor materials, Shaheen *et al.* achieved a cell efficiency of 2.5 % using a 1 : 4 ratio of poly(2-methoxy-5-(3',7'-dimethyloctyloxy)-*p*-phenylene vinylene) (MDMO-PPV) donor and PCBM acceptor.[23] The potential of polymer bulk heterojunctions was further realised with optimisation of the poly(3-hexylthiophene) (P3HT) : PCBM system, with efficiencies of up to 5.2 % reported.[30] This system is of great interest to researchers, since modification of the system properties could be achieved through change of solvent, ratio of polymer to fullerene, tuning bulk heterojunction layer thicknesses, annealing temperature and conditions, and through the use of interlayers.[30-35] The relatively high efficiency and ability to tune the properties of the P3HT : PCBM blend have established it as a model system, with very well known and heavily characterised properties.

More recently low band gap (E_g) polymers have been synthesised to absorb at longer wavelengths, to harvest the near infra-red. Consequently, Li *et al.* reported a

polymer cell achieving a record efficiency of 10.6 % with NREL certification, using a tandem architecture.[36]

1.4 Fundamentals of cell operation

In this section, the physical principles behind OPV cell operation are described, including cell limitations and examples of progress from literature reports. The initial section, 1.4.1, gives a brief overview of the four processes involved in current generation, with the following sections going into further detail for each step.

1.4.1 Overview of operation

Figure 1.2 illustrates the four steps of photocurrent generation in a bilayer OPV cell.
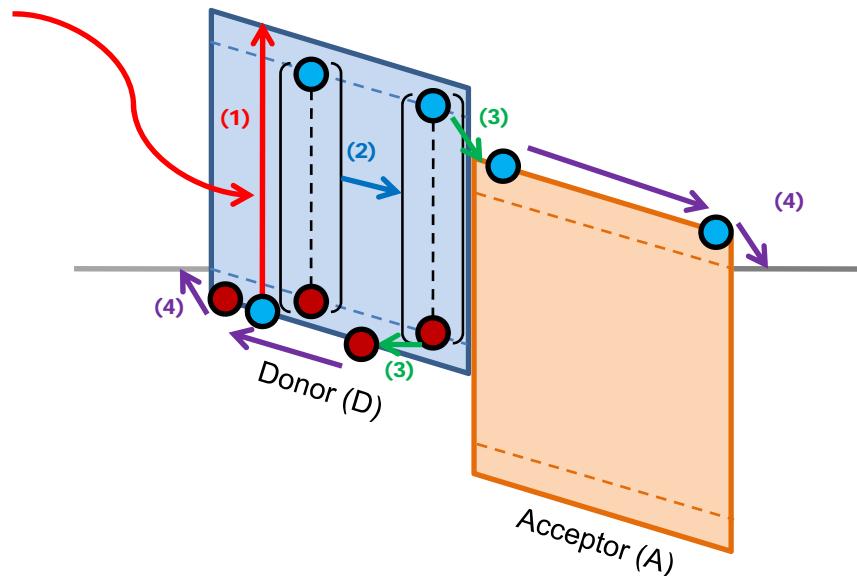
Figure 1.2: Schematic of bilayer OPV operation with light absorption and exciton generation (η_A) labelled (1), exciton diffusion (η_{ED}) (2), exciton dissociation (η_{CT}) (3) and charge collection (η_{CC}) (4).

Incoming photons of light with an energy equal to or larger than the band gap (E_g) energy of the absorber are able to excite an electron from the highest occupied molecular orbital (HOMO) to the lowest unoccupied molecular orbital (LUMO) of either the donor or acceptor material. Successful photon absorption leads to the creation of an exciton. The exciton is a neutrally charged Coulombically bound electron-hole pair. This process is known as light absorption and exciton generation, η_A. The exciton is then able to diffuse through the material, where it may preferentially reach the D / A interface, or detrimentally recombine at trap or defect sites. The probability of the exciton reaching the D / A interface is described by η_{ED}. This process is directly impacted by the L_D of the organic material, which in turn depends on the rate of the exciton diffusion and the exciton lifetime. To achieve maximum absorption, layers several times thicker than the typical L_D values are required and therefore a trade off occurs between η_A and η_{ED}.

If the exciton reaches the D / A interface, and a favourable energy level offset between the materials is present, the exciton splits into free charges. The electron is transferred to the acceptor LUMO and the hole remains in the donor HOMO. These charges still feel Coulombic interactions towards one another and are either separated by the cells internal electric field, or suffer geminate pair recombination. The efficiency of this process is known as η_{CT}. Any free charges are subsequently transported through the organic layers under the presence of the internal electric field, allowing for charge collection, with efficiency η_{CC}, at the respective electrodes.

Hence, the overall efficiency of the charge generation process, the external quantum efficiency (η_{EQE}), is defined by Equation 1.1.[37]

$$\eta_{EQE}(\lambda, V) = \eta_A(\lambda)\, \eta_{ED}\, \eta_{CT}(V)\, \eta_{CC}(V) \qquad \text{Equation 1.1}$$

1.4.2 Electronic characteristics

In order to understand the absorption characteristics of the organic semiconducting photo-active layers, the factors determining the electronic characteristics of a material need to be described.

The charge conductivity of materials is typically split into three main groups: conductors, semiconductors and insulators. For a lone atom, the discrete energy levels are separated by a relatively large energy. As several atoms are brought close together, each atom will add a further bonding and antibonding orbital, with discrete values. As additional atoms are added to form a solid, the orbitals overlap in a continuum, forming bands. This is shown schematically in Figure 1.3.[38]
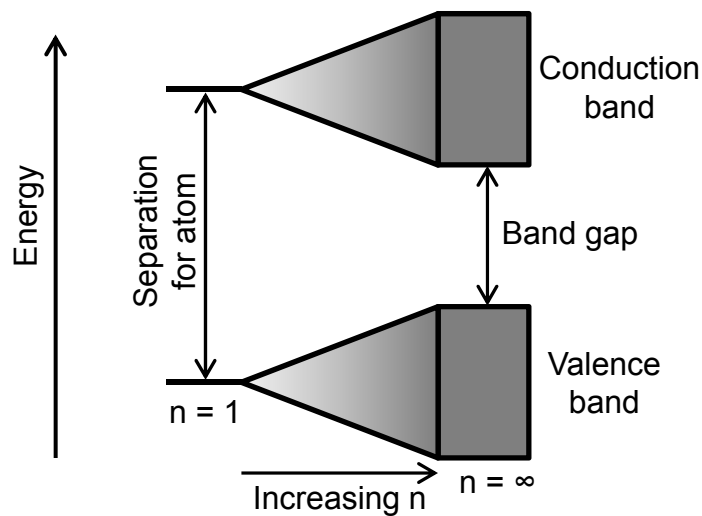
Figure 1.3: Overlap of atomic orbitals to form continuous bands with increasing number of atoms, n.

To determine the population distribution of electrons, *f(E)*, in a material, the Fermi-Dirac distribution can be used, and is shown in Equation 1.2.

$$f(E) = \frac{1}{(e^{\frac{E-E_f}{k_B T}}) + 1}$$

Equation 1.2

Where E_f is the Fermi level or Fermi energy, k_B is the Boltzmann constant and T is temperature. The Fermi energy indicates the position where the probability of finding an electron is $^1/_2$.

In a conductor, there is no energy gap between the valence and conduction band edges, or the valence band is only partially filled. At 0 K, the valence band is completely filled and the conduction band is completely unfilled. Therefore, the Fermi level of a conductor is positioned at the valence and conduction band edge overlap. Consequently, the edge of the valence band is equal to the work function (Φ) of the conductor. The work function is the minimum energy required to remove an electron from a bound state to the vacuum level, V_l, as shown in Figure 1.4(a).
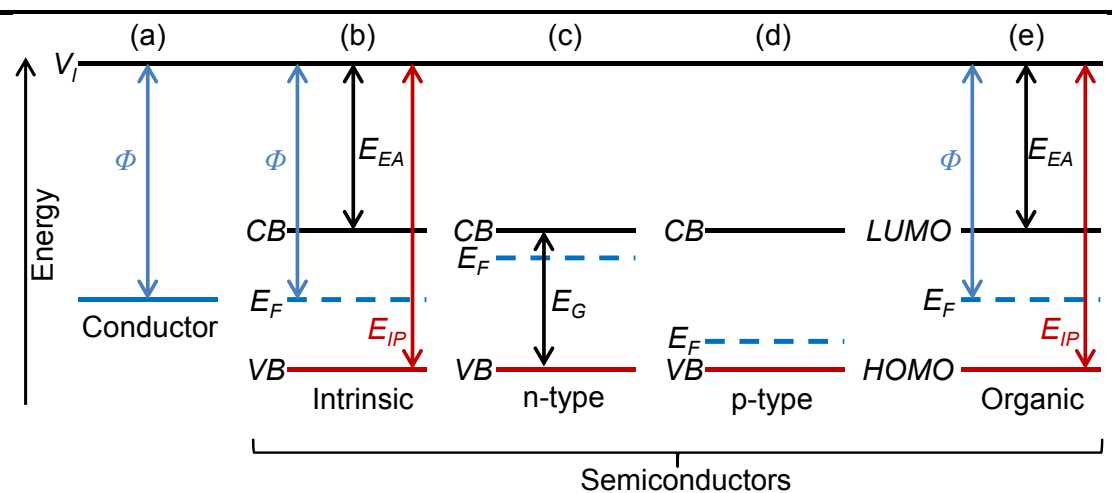
Figure 1.4: Electronic structure characteristics for (a) conductor, (b) intrinsic inorganic semiconductor, (c) n-type inorganic semiconductor, (d) p-type inorganic semiconductor and (e) an organic semiconductor.

For inorganic semiconductors, the edge of the valence and conduction bands are separated by an energy, E_g. The energy required to remove an electron from the edge of the valence band to the V_l is defined as the ionisation potential energy (E_{IP}). In semiconductors, the electron affinity (E_{EA}) is the energy difference between the edge of the conduction band to the V_l. These are shown schematically in Figure 1.4(b). Thus, for an intrinsic semiconductor with no impurities or dopants, the Fermi level is at an equal energy from the valence and conduction band edges, at the centre of the band gap.

The properties of inorganic semiconductors are often modified by doping, where dopant atoms are added substitutionally to the semiconductor lattice. Dopants, such as phosphorus in a silicon crystal, can donate electrons to the conduction band. This adjusts the Fermi level position, moving it closer to the conduction band. Semiconductors doped in this manner are known as n-type, with lower work function values than their intrinsic counterparts, as illustrated by Figure 1.4(c). Alternatively, an electron deficient dopant material, such as boron in a silicon crystal, can be used to remove electrons from the valence band. Doping in this manner increases the work function value, due to a lower lying Fermi level. Semiconductors doped by this approach are p-type, as displayed in Figure 1.4(d).

Typically, the organic semiconductors used throughout this work as photo-active layers are considered to be intrinsic, although they may be doped by defects and impurities. For organic semiconductors, the bands are more commonly referred to as HOMO and LUMO levels, illustrated in Figure 1.4(e). Compared to the continuous band structures of the covalently bound inorganic materials described above, organic semiconductors have weaker electronic coupling between molecules, leading to narrow widths for the HOMO and LUMO levels.[39]

1.4.3 Absorption and exciton formation

The absorption coefficients of organic materials are usually very high compared to Si, with intense maxima as a result of the favourable wavefunction overlap of the materials ground and lowest excited states.[40] This allows thin films of organic material to still have relatively high absorption at their maxima. However, due to the narrow HOMO and LUMO bands, the main absorption regions of organic semiconductors are typically only 200 - 300 nm wide, with well defined electronic transitions. Inorganic semiconductors benefit from a continuum of states, so photons with energy above that of the materials band gap are absorbed. For organic materials, photons with energies below that of the band gap are still lost, but further loss of absorption occurs at certain photon energies above the band gap threshold. In addition, inorganic materials have small band gaps, for example 1.1 eV for Si, whereas organic semiconductor band gaps are normally > 1.8 eV.[41]

The absorption profile of an organic layer is also extremely sensitive to morphology and crystallinity, with donors materials such as phthalocyanines having distinct aggregate and monomer peaks. Hence, structuring can affect the relative contributions of the absorption peaks, and therefore the optical properties of the layer.[42] More crystalline materials have been demonstrated to have wider windows of absorption.[43] The donor and acceptor layers used in cells are often chosen to have complementary absorption profiles, allowing a wider spectral coverage.

When a photon is absorbed to promote an electron into an excited state, the electron thermally relaxes and forms an exciton with the remaining hole. The low dielectric constant ($\varepsilon \sim 3 - 4$) of the organic material leads to the formation of a so called Frenkel exciton, shown in Figure 1.5(a). The Coulombic interaction between the hole and electron is high at several hundred meV, typically resulting in localisation of the electron and hole to a single molecule. This is illustrated in Figure 1.5(b), with the Bohr radius (r_B) of the organic semiconductor shown to be smaller than the Coulombic potential well (r_C) at room temperature. Consequently, for organic materials the exciton formed can be treated as a neutrally charged mobile species, with separation requiring an interface with favourable energy offsets.[45, 46]
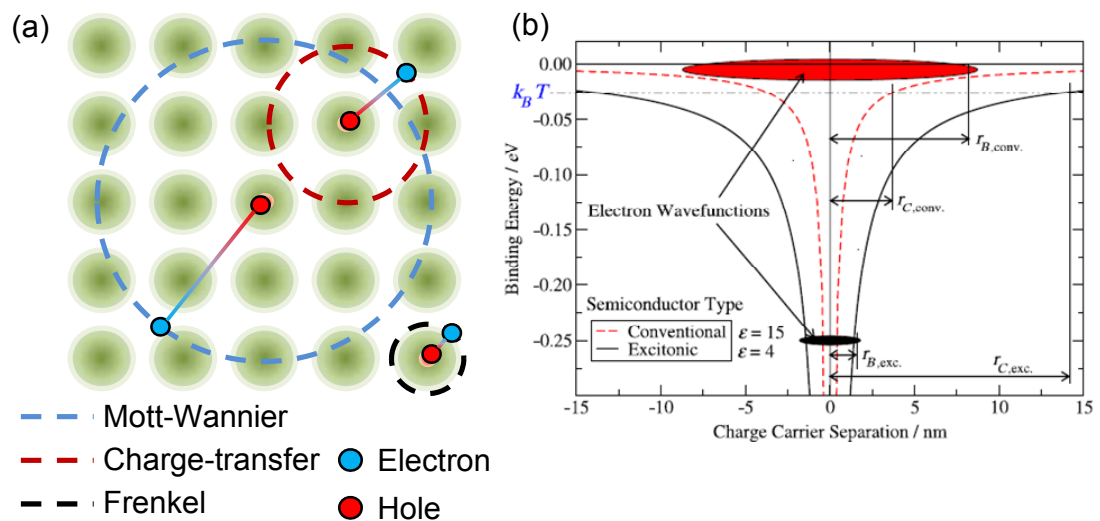
Figure 1.5: (a) Frenkel (black radius), charge-transfer (red radius) and Mott-Wannier (blue radius) excitons. (b) Exciton binding energy against the separation of the component charges for both organic and inorganic semiconductors, taken from reference [44].

This is in stark contrast to inorganic cells, which possess high dielectric constants ($\varepsilon \sim 15$) and form Mott-Wannier excitons. The high charge screening of

the covalently bound inorganic ensures a low Coulombic interaction between the hole and electron, resulting in the exciton splitting into component charges at room temperature ($k_B T \sim 26$ meV).[44]

1.4.4 Exciton diffusion

Since the Frenkel exciton can be treated as a neutrally charged species, the movement of the exciton is to a first approximation not influenced by electric fields. Instead, they diffuse by a random hopping process between molecules and grains.[47] L_D is determined by the diffusion coefficient (D) and exciton lifetime (τ) using Equation 1.3.[43]

$$L_D = \sqrt{D\tau}$$
<div align="right">Equation 1.3</div>

Due to a typically short L_D, this process is considered a bottleneck for OPV cells. If the exciton is not created within an L_D of the D / A interface, it is likely to recombine or be trapped by impurities. Indeed, a longer L_D can be achieved using organics with fewer defects and a higher crystallinity. Alternatively, cell architectures can be designed to minimise the impact of L_D.[39]

1.4.5 Exciton dissociation and charge transport

If an exciton diffuses successfully to the D / A interface, it still requires separation into its component charges. In order to be energetically favourable to split an exciton formed in the donor material, with electron transfer to the acceptor, the offset between the donor and acceptor LUMO levels must be larger than the exciton binding energy. The exciton binding energy is typically 0.1 - 0.5 eV.[39] For an exciton formed in the acceptor layer, hole transfer is likely to occur when the donor and acceptor HOMO offsets are larger than the exciton binding energy.[11] When

favourable the exciton dissociation process is fast, with charge transfer shown to take picoseconds.[48]

In order to take advantage of the efficient exciton dissociation process at the D / A interface, bulk heterojunction OPV cells were introduced. By increasing the surface area of the D / A interface and carefully controlling the domain sizes of the donor and acceptor materials, the probability of splitting excitons is enhanced. However, the disadvantage of these structures is the formation of isolated material islands within the bulk photo-active layer, increasing recombination due to compromised charge transport pathways.

After separation at the interface, electrons are transported through the acceptor and holes through the donor material. Charge carrier movement occurs through intermolecular hopping, with drift due to the built-in field (V_{bi}) of the cell and diffusion due to the charge carrier density gradient at the D / A interface.[43] A typical charge carrier mobility is much smaller compared to a covalently bound inorganic semiconductor, due to weak intermolecular interactions. Therefore, layer crystallinity, morphology, purity and cell architecture determine carrier mobility, varying between $\sim 10^{-6}$ cm^2 V^{-1} s^{-1} for an amorphous layer to $\sim 10^2$ cm^2 V^{-1} s^{-1} for a highly crystalline organic.[40]

Once the charges reach the respective electrodes, charge injection either directly into the electrode, or through a selective charge extraction layer can occur. The role and properties of interfacial layers and electrode materials are discussed in more detail in section 1.5.

1.5 Use of interfacial layers in OPV cells

1.5.1 The role of interfacial layers

The use of interfacial layers between the electrodes and photo-active material has become common place in OPV cell design. The factors behind the incorporation of the layers include:

- More favourable energetic alignment with the photo-active layer.

- Charge selectivity of the interfacial layer.

- Protection of the photo-active layer during metal deposition.

- Increase in operational cell stability.

- Favourable influence on the packing of organic photo-active material.

- Ability to reverse cell polarity in relation to the electrode properties to achieve efficient inverted cell architectures.

In addition, to be viable for use in OPV cells an interfacial layer should also be highly transparent, give a chemically stable interface and have an energetic match to the properties of the organic materials utilised. The conductivity of the interlayer must also be large enough to not be a limiting factor in towards OPV cell performance. Figure 1.6 exhibits the typical cell architectures for standard and inverted discrete bilayer OPV cells, with both incorporating hole and electron extracting layers. It is considered a necessity to integrate such layers in order to achieve high cell performances, highlighted by the number of recent reviews focused solely on the use of such layers.[49-53]
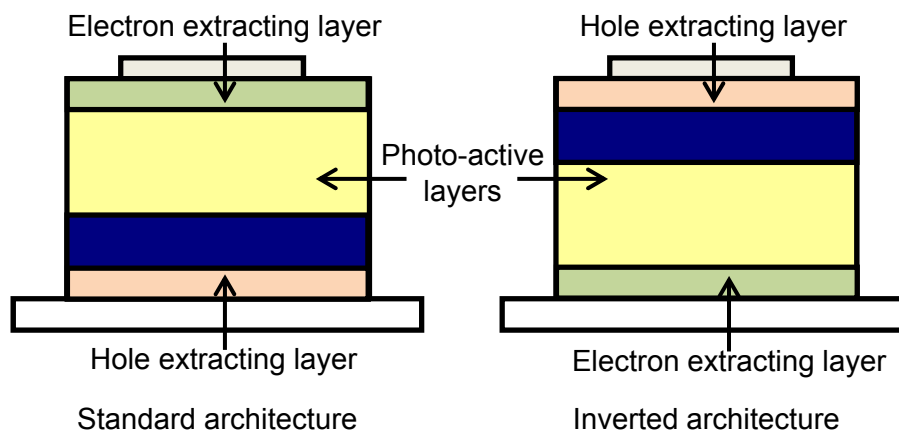
Figure 1.6: Standard (left) and inverted (right) architectures featuring hole and electron extracting interfacial layers.

1.5.2 The integer charge transfer model

When selecting an interfacial layer, the function and properties of the material used need to be carefully considered. The integer charge transfer (ICT) model highlights the importance of the interlayer work function, and is outlined in Figure 1.7.[49, 54, 55] This model predicts whether the physisorption of the organic photo-active material onto an interface will result in Fermi level pinning of the organic. The organic material has integer charge transfer states that are either positive (E_{ICT+}) or negative (E_{ICT-}) close to the HOMO and LUMO level positions respectively. The E_{ICT+} is the energy of a relaxed state when one electron is removed and transferred from the organic to the interfacial material, meaning the E_{ICT+} is lower in energy than the HOMO. The position of E_{ICT-} is the energy gained when an additional electron is transferred into the organic material and is higher in energy than the LUMO.
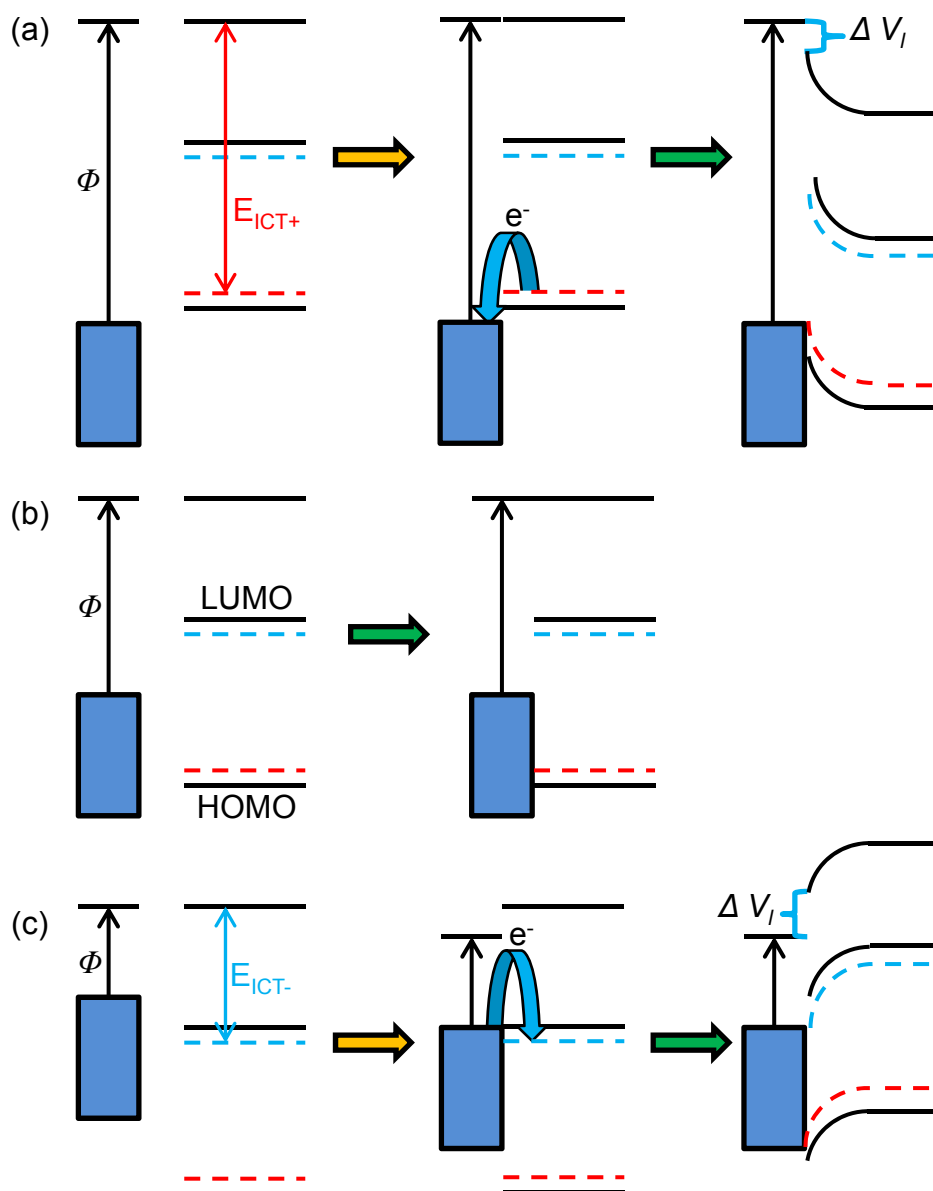
Figure 1.7: (a) Fermi level pinning of the E_{ICT+} to a high work function interfacial layer, with shift in vacuum level, ΔV_l. (b) No pinning or electron transfer when $E_{ICT+} > \Phi > E_{ICT-}$ for the interfacial layer. (c) Fermi level pinning to the E_{ICT-} with a low work function interfacial layer, with ΔV_l shift.

When the organic is brought into contact with an interfacial layer one of three possibilities occur. If the work function of the interfacial layer exceeds the E_{ICT+} of the organic, as with Figure 1.7(a), electrons are spontaneously transferred from the

organic to the interfacial layer until an equilibrium is reached. This causes Fermi level pinning of the organic to the interfacial layer and band bending, due to the formation of a space charge region,[56, 57] shown far right of Figure 1.7(a). If the work function of the interface is between E_{ICT+} and E_{ICT-}, then no electron transfer occurs and there is no Fermi level pinning at the interface, illustrated by Figure 1.7(b). However, when the interfacial layer possesses a work function value below that of the organics E_{ICT-}, there is spontaneous transfer of electrons from the interfacial layer into the organic, resulting in Fermi level pinning to the E_{ICT-}, also forming a space charge region, as displayed in Figure 1.7(c).

Consequently, a 'mark of Zorro' relationship between the organic ICT states and interface work function is formed, illustrated by Figure 1.8(a). This shows a linear dependence with a slope of 1 for interfacial layer work function values $< E_{ICT+}$ but $> E_{ICT-}$. This has been confirmed experimentally most notably by Crispen *et al.*, using a alternating polyfluorine (APFO-Green 1) polymer on a series of electrodes to demonstrate the Fermi level pinning of both E_{ICT+} and E_{ICT-}.[58] The measurements indicated the polymer obeyed the 'mark of Zorro' dependence.

The ICT model is of great importance to OPV cell design as it describes the impact of the choice of interlayer upon cell V_{oc}. When an OPV cell contains a hole extracting layer with a work function that exceeds E_{ICT+}, and an electron extracting layer with a work function smaller than E_{ICT-}, then the maximum V_{oc} obtainable is independent of the interfacial layers. If this is applicable, the contacts are often described as ohmic in the OPV literature.[49] The cell V_{oc} is therefore determined by the effective band gap of the photo-active layer minus any additional losses, such as the exciton binding energy. However, a hole extracting layer with a work function of less than E_{ICT+} or an electron extracting layer with a work function greater than E_{ICT-}

reduces the V_{oc} of the cell. In such a case, the V_{bi} of the cell is not maximised and so the upper limit of the cell V_{oc} is dependent on the work function difference between the electrodes or interfacial layers, and is also likely to lead to a reduction in cell η_p.[49, 59]
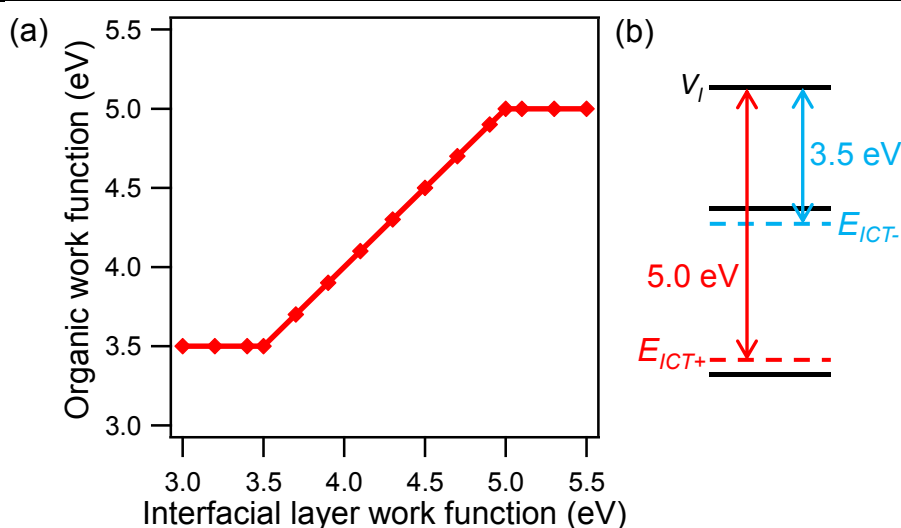
Figure 1.8: (a) 'Mark of Zorro' dependence of interfacial layer work function to organic work function, for the illustrative example organic semiconductor in (b).[58]

1.6 Interfacial layers previously used in OPV cells

1.6.1 Electron extracting layers and electrodes

Many of the interfacial layers used as electron extracting materials for OPV cells originated from previous use in organic light emitting diodes (OLEDs).[50] As presented using the ICT model in Section 1.5.2, it is favourable to utilise a low work function material for electron extraction in OPV cells. Hot metal electrodes directly deposited onto the organic photo-active layer have been shown to cause damage to the surface and result in cell degradation due to diffusion of the metal into the photo-active layers over time.[60, 61] In addition, the metal electrode work function values are

often too large to ensure Fermi level pinning of the acceptor material. This was illustrated by the work of Reese *et al.*, where a standard architecture bulk heterojunction P3HT : PCBM system was contacted with Ag, Al, Mg : Ag / Ag, LiF / Al, Ca / Al and Ba / Al.[62] Ag and Al have work function values of 4.26 and 4.28 eV respectively and resulted in poor V_{oc} and *FF* values. By using the lower work function Ca (2.87 eV) and Ba (2.7 eV) electron extracting layers with an Al top contact, both the V_{oc} and *FF* increased by ~ 50 %. Accordingly, η_p was more than doubled when using the low work function layers.[62]

The polymer OPV community make extensive use of a thin (< 1 nm) thermally evaporated electron extracting layer of lithium fluoride, LiF. The deposition of LiF on polymers was first demonstrated by Brabec *et al.*, giving higher V_{oc} and *FF* values for MDMO-PPV : PCBM cells compared to direct metal deposition.[63] Caesium carbonate (Cs_2CO_3) has been used as an electron extracting layer, fabricated using both thermal evaporation and solution processing. Li *et al.* revealed that Cs_2CO_3 could be used in standard and inverted cell architectures with P3HT : PCBM cells, ensuring the cell performance was independent of the electrode orientation.[64] Cs_2CO_3 was solution processed and used with inverted P3HT : PCBM cells by Liao *et al.*[65] When the layer was used as fabricated, inverted cells achieved a η_p of 2.31 %. However, by annealing the electron extracting layer at 150 °C the Cs_2CO_3 decomposed to give caesium oxide (Cs_2O). This modified the properties of the layer, including a decrease in work function from 3.45 eV for Cs_2CO_3 to 3.06 eV for Cs_2O. The low temperature annealing process led to increased V_{oc}, *FF* and J_{sc}. Consequently, the cell η_p increased from 2.31 % to 4.19 % by applying the annealing step to the electron extracting layer.[65]

Another group of electron extracting materials are n-type transition metal oxides, such as TiO_x and ZnO_x. These have been utilised due to their increased stability, transparency and the low cost of the materials.[66, 67] TiO_x has been used in both standard and inverted cell architectures.[35, 68, 69] In a standard cell architecture, the optical spacer effect of the layer led to an enhanced J_{sc} and η_p.[70] When using TiO_x in an inverted cell, the layer can be heat treated at high temperatures (500 °C) to form nano pillars of a distinct phase rather than amorphous layers.[71] Schumann *et al.* electrodeposited a ZnO layer onto ITO at low temperatures, enabling a high degree of control over layer fabrication.[67] In this instance, the vertical phase separation of the P3HT : PCBM blend indicated an inverted structure was favourable.
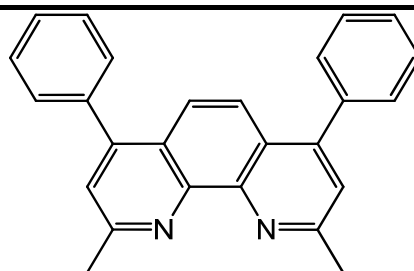
Figure 1.9: Structure of the electron extracting material bathocuproine, BCP.

The small molecule OPV community regularly use bathocuproine (BCP) as the electron extracting layer, since it can be thermal evaporated at low temperatures. BCP is a low work function, wide band gap organic semiconductor, and has the structure shown in Figure 1.9. Peumans *et al.* utilised BCP in CuPc / PTCBI cells to increase η_p.[72] Rand *et al.* demonstrated that charge transport through BCP was facilitated by defect states within the BCP band gap, induced by hot metal penetration during deposition.[73] This electron extracting layer also acts as an exciton

blocking layer due to a low lying HOMO level.[13] Gommans *et al.* incorporated BCP in a SubPc / C_{60} system, increasing the V_{bi} of the cells compared to a sole Al electrode.[74] This produced an increase in V_{oc} from 0.07 to 0.92 V, with a corresponding increase of η_p from 0.05 to 3.03 %. Despite these advantages, BCP is also known to crystallise over time, leading to cell degradation.[75]

1.6.2 Hole extracting layers and electrodes

The majority of OPV cells reported utilise ITO as the transparent conductive electrode. This is due to the excellent transparency and conductivity achieved by ITO, with a sheet resistance of ~ 15 Ω sq.[76] These advantages explain the extensive use of ITO in consumer electronics. ITO is composed predominantly of indium oxide, a wide band gap material, with tin doping in a ratio of 9 : 1 for In : Sn. The tin dopants provide additional electron rich states near the indium oxide conduction band, facilitating conductivity. Due to the variation of composition and reactivity across the ITO surface, cleaning procedures and surface treatments have dramatic effects on the surface conductivity of ITO.[77] These processes, alongside sputter deposition, result in the electrical inhomogenity of the ITO surface. This inhomogenity was verified by Armstrong *et al.* using conductive atomic force microscopy (c-AFM), highlighting the variation of surface conductivity with different ITO surface treatments.[76] An initial multiple stage solvent cleaning procedure produced conductivity 'hot spots' across the surface. After an oxygen plasma treatment, the 'hot spots' were found to be less prominent, but the surface conductivity still varied noticeably. A harsh acid treatment of the ITO etched the surface to give significantly higher conductivity. Despite this, conductivity was still not homogeneous and the enhancement was only temporary.[76] UV / ozone surface treatment is commonly employed to remove carbon contaminants and residues from

the surface. This results in a higher work function for ITO, measured between 4.6 - 4.8 eV. The UV / ozone surface treatment is also time dependent, since surface contamination increases with air exposure.

Due to the relatively low work function of the ITO surface even after treatment, the electrode does not provide the ohmic contact desired for high ionisation potential donor materials. Therefore, the photo-active layers deposited directly onto bare ITO are likely to result in reduced V_{oc} and η_p values for cells. In addition, ITO has been demonstrated to be the cause of significant degradation in OPV cells. Indium and oxygen diffusion from ITO into the photo-active layer, photo-oxidation and variation of work function over time are all detrimental side effects attributed to the surface.[77-81] From a commercial point of view, the cost of indium is continually rising due to large demand and the increased expense of mining.

Thus, there is a drive for new transparent conductive electrodes to be investigated. Promising alternatives to ITO have been demonstrated in the OPV literature, including silver nanowires,[82] thin gold films and other transparent metal oxides such as Al doped ZnO.[83, 84] However, few of these electrodes demonstrate the same sheet resistance, transparency and scalability as ITO.

In order to achieve favourable electronic properties at the interface with the donor layer, hole extracting layers are regularly incorporated in to cells regardless of the electrode used. As with the electron extracting materials in section 1.6.1, many of the hole extracting materials have previously been incorporated as hole injection layers in OLED devices.[52]

Poly(3,4-ethylenedioxithiophene) (PEDOT) : Polystyrene sulfonic acid (PSS) (Figure 1.10) hole extracting layers were first used in OPV cells to modify the ITO surface by Roman *et al.* in 1998.[85] The conductive PEDOT is doped using PSS to increase solubility in water.[49] The aqueous dispersion can be spin coated under ambient conditions, with films displaying a remarkable transparency. Indeed, the high transparency has resulted in cell performances that are largely independent of the PEDOT : PSS layer thickness.[86] Kim *et al.* revealed that even varying film thickness between 60 and 165 nm had little effect on the cell η_p.[86] Therefore, PEDOT : PSS has been used to prevent cell shorts due to protrusions of the ITO surface.[87, 88]
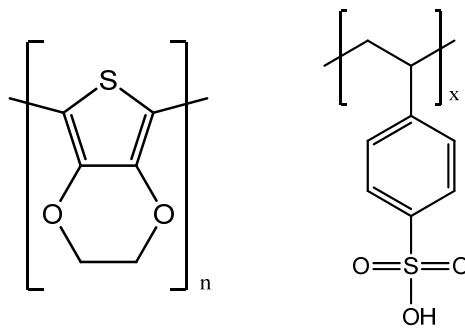
Figure 1.10: Chemical structure of PEDOT (left) and PSS (right).

It is frequently reported that a PEDOT : PSS layer possesses a higher work function than bare ITO. This has been shown to result in increased cell V_{oc} and thus η_p, due to enhanced energy level alignment with systems such as P3HT : PCBM.[61, 89, 90] PEDOT : PSS hole extracting layers can also be modified by post deposition processing treatments and additives. Films are typically annealed post deposition to remove any residual water content and to allow alterations to the surface work function.[86, 91] Other reported treatments of the surface include UV irradiation and oxygen plasma treatment.[92, 93] The composition of the PEDOT : PSS surface has

been demonstrated to significantly impact polymer light emitting diode (PLED) devices, with higher work function values obtained with increasing PSS surface concentration.[87] A number of additives have been utilised in PEDOT : PSS layers to tailor conductivity, work function and surface morphology.[52] Additives include Sorbitol,[94] glycerol,[95] gold nanoparticles and graphene oxide.[96, 97]

Despite the ease of processing and ability to modify the layer properties, PEDOT : PSS has several considerable disadvantages. The high acidity of the films has been demonstrated to corrode the surface of ITO.[80, 98, 99] The ability to process a PEDOT : PSS layer from water also leads to water retention in cells. In turn, the hygroscopic nature of the material causes delamination of photo-active material from the electrode, degrading cell performance.[100, 101] The PEDOT : PSS surface additionally suffers from inhomogeneous electrical properties.[30] The work function values commonly reported for PEDOT : PSS (5.0 - 5.2 eV) are also too low to attain ohmic contact with some high ionisation potential donor materials. Therefore, an alternative hole-extracting layer is desirable.

Self assembled monolayers (SAMs) provide a method of tailoring the work function of the surface in contact with the photo-active layers. SAMs anchor to the ITO surface and give an effective dipole that is dependent on the structure of the SAM used. Consequently, careful selection of the SAM can lead to the desired electrical properties to match the organic layers used. Khodabakhsh *et al.* demonstrated increased cell performance for a CuPc / C_{60} system with a series of SAMs, facilitating increases in J_{sc} whilst V_{oc} remained similar for each interface.[102] However, both Sharma *et al.* and Cook *et al.* incorporated SAMs into pentacene / C_{60} cells and achieved analogous performances to the cells grown on bare ITO.[57, 103] Since pentacene exhibits a relatively low ionisation potential, increasing the work

function of the surface beyond this value did not result in additional performance gains. Nevertheless, Cook *et al.* did observe an increased operational stability for the OPV cells fabricated on the SAMs.[57]

When using the high ionisation potential donor SubPc, Sarangerel *et al.* reported a correlation between higher surface work functions obtained using SAMs, and higher V_{oc} values.[104] This general trend was also revealed in studies by Beaumont *et al.*, for both the SubPc / C_{60} and Chloroaluminium phthalocyanine (ClAlPc) / C_{60} systems. The lower ionisation potential donor, CuPc, achieved similar V_{oc} values with a range of SAM work functions values. Yet, whilst SAMs offer a high degree of control over the properties and work function of a surface, the preparation of SAMs typically takes several hours to achieve reproducible electrode coverage.[57, 105] Accordingly, for realistic commercial use faster methods of coverage need to be investigated.

Metal oxide layers have also been utilised as hole extracting layers. After the use of metal oxides in OLED devices,[106] Shrotriya *et al.* demonstrated vanadium oxide and molybdenum oxide as alternative hole extracting layers, comparable to PEDOT : PSS in P3HT : PCBM bulk heterojunction cells.[107] Irwin *et al.* produced a p-type nickel oxide layer formed using pulsed laser deposition (PLD), increasing the performance of P3HT : PCBM cells from 2.40 % on PEDOT : PSS to 5.16 % with insertion of the metal oxide.[30]

Therefore, at the beginning of this PhD project, metal oxide hole extracting layers displayed great potential as hole extracting layers in OPV cells. Since late 2008 there have been many literature reports on the interfacial layers effects, characterisation of the materials and interest in the stability of cells incorporating

these layers. Metal oxide layers will be discussed in further detail in the results chapters of this thesis, Chapters 3 to 5.

1.7 Photo-active layer materials

In this work, several different photo-active layer combinations were utilised, allowing the ability to differentiate cell characteristics. Below, the general properties of the donor and acceptor materials are briefly outlined.

1.7.1 Phthalocyanine donor materials

Since the discovery of phthalocyanines by Linstead in 1934, the molecules have been widely used as dyes and colourings. Phthalocyanines consist of four isoindole sub units linked via nitrogen atoms, with excellent chemical flexibility. This flexibility arises due to the ability to functionalise the sub units, or replace the hydrogen atoms in the central cavity with one of 70 metallic and non metallic ions. Phthalocyanines are highly aromatic 18 π-electron macrocycles, that can either be planar or non planar with the variation of the central ion.[108]

The electronic properties of phthalocyanines are largely determined by both the central ion in the molecule and the functionalisation of the macrocycle with either electron withdrawing or donating substituents. The absorption profile of a phthalocyanine is dominated by Q-band absorption, producing an intense band typically in the range 550 - 750 nm. Higher energy B-band transitions give further absorption peaks below 400 nm.[39, 108]

Three phthalocyanine based molecules have been used in this work as donor materials. Each is described further below, with the chemical structures displayed in Figure 1.11.
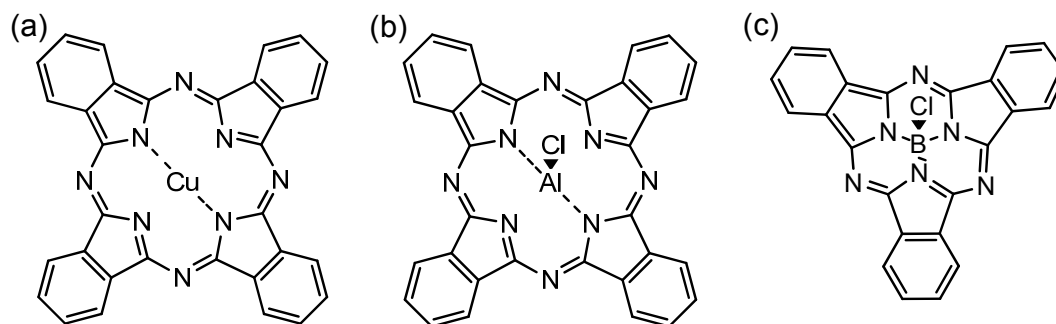
Figure 1.11: Molecular structures of: (a) CuPc, (b) ClAlPc and (c) SubPc.

1.7.2 Copper phthalocyanine

CuPc has been utilised as a donor material since Tang incorporated it in the first bilayer OPV cell, with the molecular structure shown in Figure 1.11(a).[11] Since this discovery, CuPc has become a common reference material. In solution, the main CuPc absorption peak is due to the monomer Q-band transition, producing a peak at 690 nm. When thermally evaporated into a thin film, a dimer peak at 620 nm becomes dominant, with the smaller monomer peak still present.[43] The ionisation potential of CuPc has been reported to be between 4.95 - 5.20 eV, with an electron affinity of 3.5 - 3.6 eV.[109, 110] This facilitates a favourable energy level offset for use as a donor material with a C_{60} acceptor.[13] CuPc has also been halogenated and used as an acceptor material, due to the fluorine atoms withdrawing electron density and consequently lowering the molecular HOMO and LUMO levels.[19]

Several polymorphs of CuPc are obtainable by varying the growth conditions, with the α and β most commonly reported. With deposition onto a

substrate at room temperature the α polymorph is usually obtained. The polycrystalline CuPc molecules align roughly parallel to the substrate surface, producing a herringbone structure as illustrated in Figure 1.12.[39, 42] The direction of highest charge mobility is shown to be parallel to the substrate in these cells. As a result of this, Sullivan *et al.* used templating of the CuPc layer to gain favourable charge mobility for OPV cells, with the molecules lying flat and in stacks perpendicular to the substrate.[42]
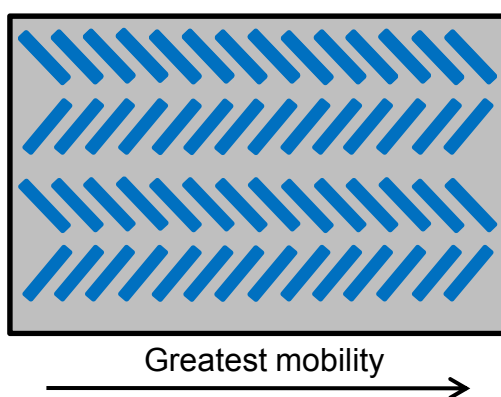
Figure 1.12: Top down illustration of CuPc deposited onto an ITO substrate, with the direction of highest charge mobility indicated to be parallel to the substrate.[42]

1.7.3 Chloroaluminium phthalocyanine

ClAlPc contains an Al metal centre with an out of plane Cl dipole as displayed in Figure 1.11(b). Due to the presence of this dipole the molecule is non planar, demonstrating weak crystallinity in a slip stack arrangement.[39] Unlike most phthalocyanine thin films, the main absorption peak of ClAlPc occurs at 740 - 755 nm, in the near infrared region.[16] Therefore, this low band gap material has a complementary absorption profile for use in tandem cells with other phthalocyanines.[26, 111]

ClAlPc has been revealed to also have a lower lying HOMO compared to CuPc, with an ionisation potential of 5.4 eV.[16] Thus, when using the same acceptor material, C_{60}, the effective band gap between the ClAlPc HOMO and C_{60} LUMO levels is larger, resulting in higher V_{oc} values. This has been demonstrated experimentally, with V_{oc} values up to 0.83 V reported for this system.[112, 113]

1.7.4 Boron subphthalocyanine chloride

The structure of SubPc is shown in Figure 1.11(c). SubPc is the only synthesised subphthalocyanine, discovered by accident in 1972 when Meller and Ossko were trying to synthesise boron phthalocyanine.[114] The removal of an isoindole group from the standard phthalocyanine macrocycle leads to the formation of the non planar, cone shaped subphthalocyanine. These three isoindole groups form the 14 π-electron aromatic macrocycle.[115, 116]

The non planar structure leads to amorphous layers, with a high solubility and a small amount of aggregation.[39] With low crystallinity, absorption in thin films is dominated by the monomer peak produced at 590 nm, with a smaller shoulder due to dimers. Much like other phthalocyanine structures, the Q-band and B-band π-π* transitions are the origins of the peaks in the visible and UV regions respectively.[117]

The low lying HOMO level of SubPc gives it a significant advantage for use as a donor material. With an ionisation potential of 5.6 eV, the HOMO resides 0.2 eV lower than ClAlPc and 0.4 − 0.65 eV below the reported CuPc values. Hence, larger effective band gap values are expected, with higher V_{oc} values likely. This was demonstrated by Mutolo *et al.*, where SubPc / C_{60} cells produced a V_{oc} of 0.97 V, compared to the CuPc / C_{60} system which achieved only 0.43 V. This resulted in a similar increase in the overall performance of SubPc / C_{60} cells.[109]

Even higher V_{oc} values have been obtained by halogenating SubPc to lower the HOMO and LUMO positions of the material for use as an acceptor. Sullivan *et al.* obtained 1.31 V from a SubPc / Cl$_6$-SubPc system.[21] The low lying HOMO of SubPc has also allowed for its use as an acceptor material in OPV cells utilising lower ionisation potential donor materials.[20]

1.7.5 Pentacene

Pentacene is one alternative donor material to phthalocyanines that can also be thermally evaporated. It is a member of the polyacene group with 5 fused aromatic rings, displayed in Figure 1.13. A pentacene layer posseses crystalline character, with a very high charge mobility of 1-2 cm^2 V^{-1} s^{-1}.[39] Additionally, a long L_d of 65 nm has allowed for a thicker pentacene layer in bilayer cells in comparison to other donor materials, enhancing cell current production.[15, 81, 118] The main absorption region of a pentacene layer is 500 - 700 nm, with two main maxima, each possessing a smaller shoulder.[81]
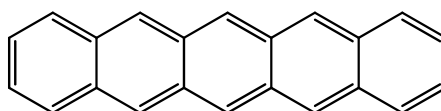
Figure 1.13: Molecular structure of pentacene.

The main disadvantage of pentacene as a donor material is the relatively low ionisation potential, with reported values between 4.8 - 5.0 eV.[15, 119-121] This only allows a small effective band gap with common acceptor materials, and consequently pentacene / acceptor cells produce relatively low V_{oc} values.[81]

1.7.6 Fullerenes

The most well known fullerene is C_{60}, discovered in 1985 by Kroto.[12] The structures were named after Buckminster Fuller, due to the resemblance to his architectural designs. C_{60} is displayed in Figure 1.14(a) and is constructed from 12 pentagonal and 20 hexagonal rings, with each pentagonal ring adjacent to 5 hexagonal rings.
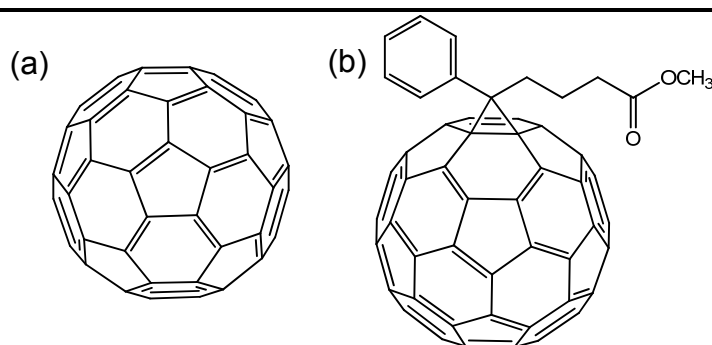
Figure 1.14: Molecular structures of (a) C_{60} and (b) PCBM.

C_{60} is most commonly employed as an electron acceptor material in OPV cells. This is because of a high electron mobility ($\sim 10^{-2}$ cm^2 V^{-1} s^{-1}), the ability to accept between 6-12 electrons and favourable energy level offsets with common donor materials.[122] The electron affinity value of 4.5 eV, and low lying HOMO at 6.2 eV, enable the favourable dissociation of excitons at most donor / C_{60} interfaces.[123] With a thermally evaporated layer having strong absorption below 500 nm, it is also complementary to the majority of thermally evaporated donor materials.

However, C_{60} has a low solubility due to a tendency to aggregate, and consequently this led to the synthesis of PCBM, shown in Figure 1.14(b). The additional organic groups are used to increase the solubility of the fullerene, facilitating the widespread use of PCBM as an acceptor with polymer donors.[39] The

breaking of the symmetry seen in C_{60} enhances the absorption profile of PCBM, with increased absorption at longer wavelengths. The position of the HOMO and LUMO of PCBM (6.1 and 4.3 eV respectively) allows for favourable exciton dissociation in polymer : PCBM blends.[124]

1.7.7 Poly(3-hexylthiophene)

P3HT is a widely used polymer donor material, often referred to as the 'work horse' of the polymer community due to its versatility and use as a reference material. With the structure depicted in Figure 1.15, P3HT is usually used in its high regioregularity form rather than a random mix of regioisomers.[125] By ensuring a high number of head to tail alternating alkyl group configurations (typically > 98 % regioregular), a red shift and an increase in the solid state absorption coefficient occurs.[126, 127] Additionally, high regioregularity enhances charge mobility to values of ~ 10^{-1} cm^2 V^{-1} s^{-1}.[128]
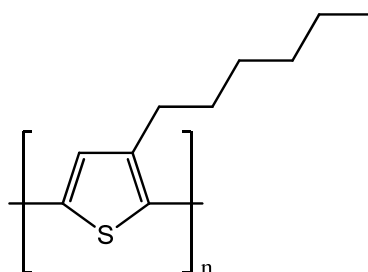
Figure 1.15: Molecular structure of P3HT.

The high miscibility of P3HT with PCBM as a blend allows a 50 : 50 composition, hence spin coated layers achieve large currents with a broad, strong absorption between 400 - 600 nm due to P3HT. The ionisation potential and electron affinity of P3HT (5.0 - 5.2 eV and 3.0 - 3.3 eV respectively) allow favourable offsets for exciton splitting at the interface with PCBM.[35, 64] Whilst not exhibiting a

particularly high ionisation potential, the effective band gap with PCBM facilitates V_{oc} values of ~ 0.60 V.[64]

By mixing P3HT : PCBM and spin coating from a weak or non polar solvent, a bulk heterojunction structure is formed. The size and crystallinity of the donor and acceptor regions can be influenced by post deposition heat or solvent annealing, improving exciton dissociation and charge transport.[31, 33]

1.8 Project outline and aims

The work presented here is focused on incorporating thin metal oxides as hole extracting layers in small molecule OPV cells. In doing so, direct comparisons will be made to the deposition of photo-active layers onto bare ITO.

Chapter 2 presents an overview of the techniques used to fabricate layers and complete devices, in addition to those utilised in the characterisation of both cells and individual films.

In Chapter 3 the use of thermally evaporated MoO_x is explored for discrete bilayer systems using donors with a variety of ionisation potentials. After optimisation of MoO_x layer thicknesses, trends found for the difference in cell performance with MoO_x on each donor / C_{60} system is rationalised by determining the electronic structure, absorption and effect of air exposure for the metal oxide. The influence of MoO_x on cell stability measurements is also evaluated.

Thermally evaporated V_2O_x was used as an alternative hole extracting layer in Chapter 4. The electronic structure of the oxide was determined using ultra-violet photoemission spectroscopy (UPS). *In-situ* growth and UPS characterisation of

organic donor materials on both bare ITO and the V_2O_x layer gave an indication of what factors influenced each cell architectures performance.

Since many groups solution process photo-active materials, a method for solution processing a V_2O_x layer was developed and is presented in Chapter 5. The processing conditions were optimised, including the atmospheric environment of spin coating and annealing. Direct comparisons of the performance of SubPc / C_{60} cells were made for bare ITO, PEDOT : PSS, thermally evaporated MoO_x and solution processed V_2O_x. Further comparisons were made for the solution processed P3HT : PCBM system on each of these interfaces, with the stability of each tested.

In Chapter 6 conclusions from each of the results chapter are made. Chapter 7 outlines possible future work is discussed.

Chapter 2: Experimental

This chapter summarises the processes and techniques that have been used to obtain the data reported in Chapters 3 - 5. Solution and thermally evaporated fabrication methods, cell testing and thin film analysis techniques are described.

2.1 Thin film and OPV cell fabrication

2.1.1 Materials and purification steps

Material purity has a large impact on the performance of OPV cells.[37, 129] Even trace impurities within the photo-active layer have been demonstrated to significantly reduce overall cell performance.[130] Therefore, the choice of material grade, material supplier and subsequent purification steps are vital to ensure reproducibility of efficient OPV cell performance. Table 2.1 outlines the materials used in this report.

Table 2.1: List of each material used within this report, stating role, supplier, purity and if the material was purified using thermal gradient sublimation.

Material(s)	Role in cell	Supplier	Purity (%)	Sublimed
PEDOT:PSS	Hole extracting layer	Sigma-Aldrich	*	No
MoO_3	Hole extracting layer	Sigma-Aldrich	99.99	No
V_2O_5	Hole extracting layer	Sigma-Aldrich	99.99	No
$V_2O_{5(sol)}$	Hole extracting layer	Sigma-Aldrich	#	No
ClAlPc	Donor material	Acros organics	98	Yes
SubPc	Donor material	Sigma-Aldrich	85	Yes
CuPc	Donor material	Sigma-Aldrich	97	Yes
Pentacene	Donor material	Sigma-Aldrich	99.9	Yes
C_{60}	Acceptor material	Nano-C	99.5	Yes
P3HT	Donor material	Rieke	rr > 98	No
PCBM	Acceptor material	Nano-C	> 99	No
BCP	Electron extracting layer	Sigma-Aldrich	96	No
Al	Electrode	Sigma-Aldrich	99.99	No

* PEDOT : PSS 1.3 % wt dispersion in H_2O, conductive grade.
# $V_2O_{5(sol)}$ used in anhydrous IPA (Sigma-Aldrich, 99.5 %).

The majority of the supplied photo-active materials were purified by thermal gradient sublimation. This is schematically illustrated in Figure 2.1. The material was transferred into the end of a disposable quartz tube, positioned inside a outer quartz tube. Glass wool was added to the end of the disposable tube in order to protect the vacuum pumps from the airborne organic material. A furnace was used to heat the organic material following a controlled heat profile, with the system held at $\sim 10^{-5}$ mbar. The furnace temperature was increased up to the sublimation point of the material, at a typical rate of 1 °C min^{-1}. At lower temperatures the impurities and residual solvents were removed. At higher temperatures the organic material sublimed and condensed on a cooler area of the inner tube. The furnace was held overnight at the organic materials sublimation temperature to give an adequate yield of pure material. Non-sublimed impurities were left at the end of the inner tube with a ring of pure material that could then be removed by cracking the inner tube, with material placed in a N_2 filled glovebox for storage.
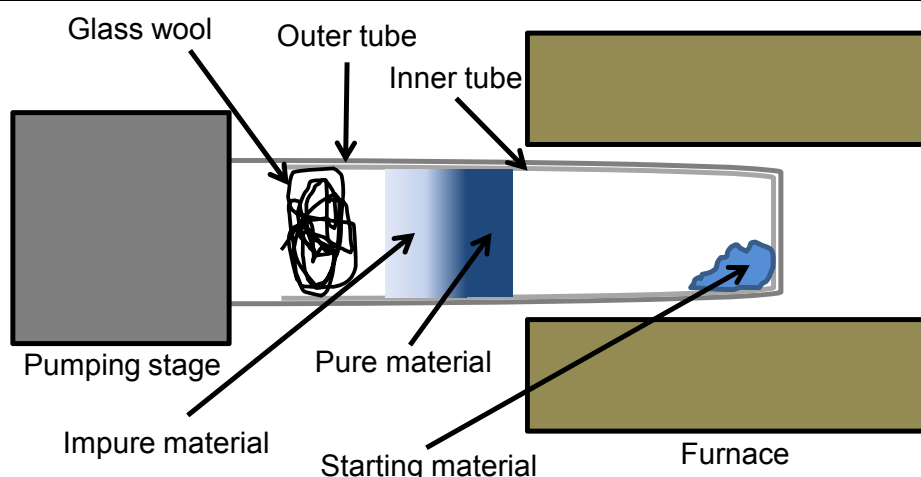
Figure 2.1: Schematic of thermal gradient sublimation purification.

2.1.2 ITO substrate cleaning

All layers for analysis and all OPV cells were deposited onto ITO coated glass. The ITO was supplied pre-patterned as 8 x 12 mm strips, on pre-cut 12 x 12 mm glass slides. Two suppliers of ITO were used. Initially Psiotec supplied substrates with a photo-resist layer (used in Chapter 3), before the supplier was changed to Thin Film Devices (used in Chapters 4 and 5). Both types of ITO provided a sheet resistance of < 15 Ω sq^{-1}.

A reproducible ITO surface was obtained using a full procedure of solvent and UV / ozone cleaning steps. The solvent cleaning step consisted of sequential substrate rinsing followed by 15 minutes sonication in acetone, 70 : 30 mixture of deionised water : decon 90, deionised water and finally isopropanol (IPA). Substrates were dried using a N_2 jet and transferred to be UV / ozone treated for 30 minutes to remove carbon residues. Immediately after this process, substrates were transferred into a N_2 filled glovebox.

2.1.3 Organic molecular beam deposition

This section describes the experimental details and principles of the organic molecular beam deposition (OMBD) system used to fabricate OPV cells and thin films throughout this report.

2.1.3.1 Overview of organic molecular beam deposition

The majority of small molecule OPV cells are fabricated using OMBD. OMBD deposition was carried out in a high vacuum Kurt J. Lesker Spectros chamber held at < 10^{-7} mbar. This provided clean and reproducible conditions for layer fabrication. Purified organic material was placed in a Knudsen cell and resistively heated between 140 - 450 °C, shown schematically in Figure 2.2. In order

to form a molecular beam through the top opening of the Knudsen cell, the material was heated to temperatures above sublimation but below that of decomposition.[131] Heating was controlled by a Eurotherm and a thermocouple sensor. Substrates were rotated in the path of the molecular beam, with molecules adsorbed onto the substrate surface. The growth of individual organic layers was controlled by both the use of a shutter, to switch the flux on and off, and by changing the rate of deposition through heater temperature settings. The technique consequently allowed for sub-nanometre control of layer thicknesses, monitored by quartz crystal microbalances (QCM) in the pathway of the molecular beam.[131] Since the deposition chamber contained several organic sources, multiple layers of materials could be processed without breaking vacuum. Several cell architectures could be fabricated without breaking vacuum by using a combination of substrate masks.
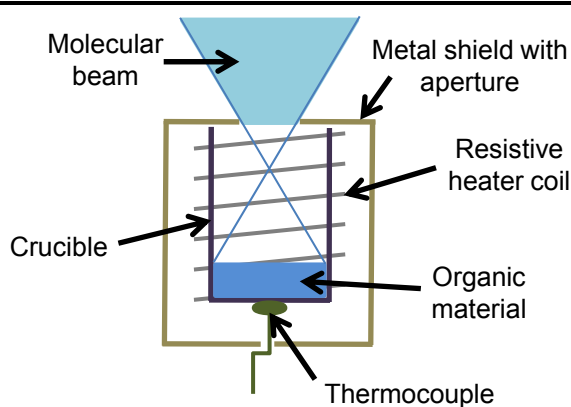
Figure 2.2: Schematic representation of a resistively heated Knudsen cell.

2.1.3.2 Metal electrode and metal oxide layer deposition

The deposition of metals and metal oxides was possible in the same vacuum chamber that was used for organic materials. These materials require much higher temperatures to sublime and therefore required separate specific sources.

Metal oxides such as MoO_3, WO_3 and V_2O_5 form clusters when thermally evaporated, rather than a molecular beam. Despite being bought in high purity form, each metal oxide required an extended period of out-gassing, with a noticeable initial rise in chamber pressure before subsequent thermal evaporation. The deposition of thin metal oxide films was monitored using a QCM.

Fabrication of device top contacts was achieved with the thermal evaporation of an aluminium pellet through a custom designed electrode mask, located in the rotating substrate cassette. Damage to the underlying organic layers was minimised by using low initial deposition Al rates. A 3 pixel arrangement was formed for each device with each pixel providing a 0.16 cm^2 area for testing. Silver paint was used to contact pixels and an ITO bottom contact to the device test setup, as illustrated in Figure 2.3.
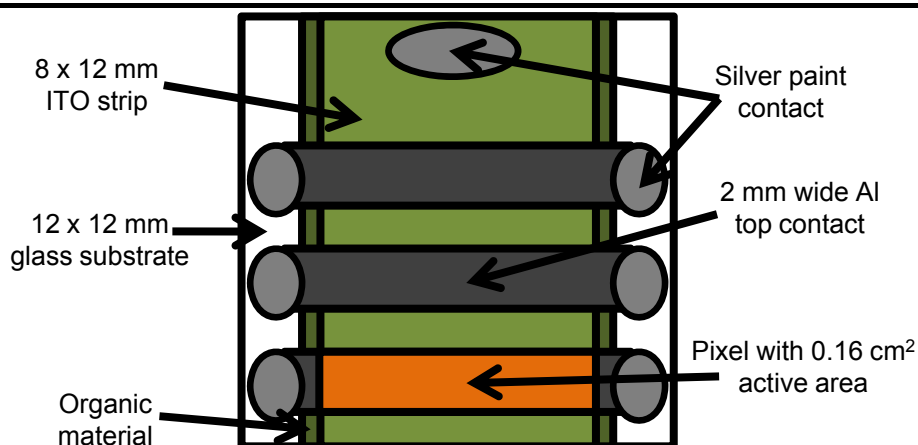
Figure 2.3: The 3 pixel device obtained via metal deposition through an electrode mask.

2.1.3.3 Layer thickness calibration and monitoring

As stated previously, the rate and thickness of both organic and metal layers was monitored *in-situ* using a QCM. The drop in frequency of the QCM oscillation is directly proportional to a known addition of quartz mass per unit area.[132, 133] This

varies with material density and the position of the source, and so in order to accurately relate the layer thickness measured by the QCM to the actual thickness of the thin film formed an *ex-situ* calibration was required for each material, known as a tooling factor.

Atomic force microscopy (AFM) step edge measurements were used for *ex-situ* thickness calibration.[132] For each material, several samples of different layer thicknesses were deposited using OMBD. Each sample was scratched several times through to the hard underlying ITO, using the tip of a needle. Tapping mode AFM images were obtained for an area containing both bare ITO and the organic layer, with an example shown in Figure 2.4. These measurements were taken for several points of each sample, for different sample thicknesses.
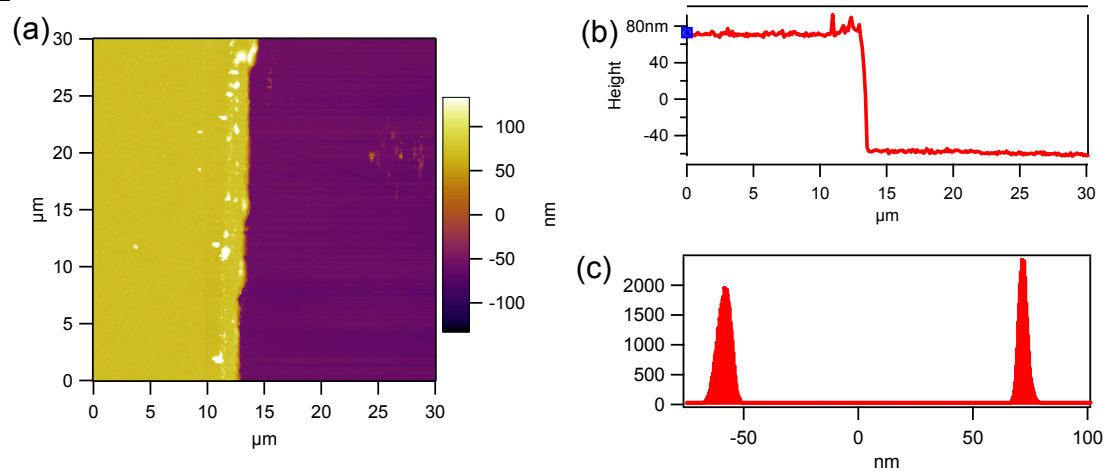
Figure 2.4: (a) AFM step edge measurement to determine the tooling factor of actual layer thickness to that measured by QCM for a V_2O_x layer. (b) cross section height profile and (c) corresponding histogram of the entire image.

2.1.3.4 Kurt J. Lesker Spectros system

A Kurt J. Lesker Spectros system was used to fabricate all thin films and cells throughout this report, unless stated otherwise. The system is schematically shown in Figure 2.5. In order to obtain high vacuum conditions, the Spectros system uses a scroll pump to achieve a rough vacuum of $\sim 10^{-2}$ mbar, before engaging a cryogenic pump to reach a base pressure of $\sim 10^{-8}$ mbar. At the top of the chamber, substrate holders are mounted onto rotating shelves, with the ability to change the substrate masking using a transfer arm. This allows for sequential *in-situ* layer deposition. With four shelves, up to three different substrate masks can be used. The main shutter acts as an on / off switch for the molecular beam, and is located just below the substrate cassette.
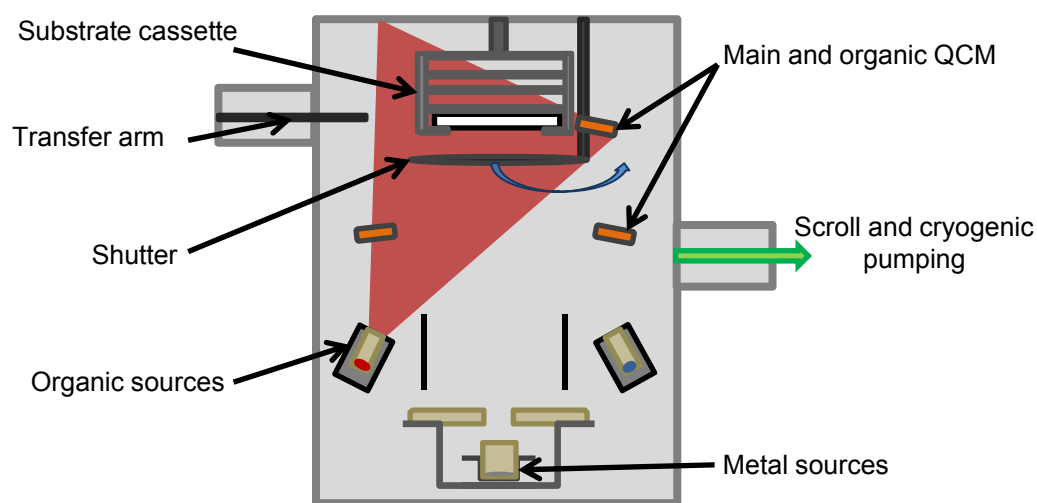
Figure 2.5: Schematic illustration of the Kurt J Lesker Spectros system.

The chamber contains three pairs of organic sources, individually monitored by a QCM. Three metal sources are positioned at the bottom of the chamber. All sources are monitored by the main QCM, level to the substrate cassette. Each pair of Knudsen cells are controlled using a Eurotherm 2408, with user input through a

computer in order to control cell temperature. The computer also monitors deposition rate, cumulative layer thickness and chamber pressure. After cell or layer deposition the substrates were removed directly into the attached glovebox, which was kept at < 1 ppm O_2 and H_2O.

2.1.4 Spin-coating

Solution processing can be an inexpensive method of forming an even thin film or to disperse nano-particles on a surface.[134] In the fabrication of OPV cells, spin-coating is commonly employed in lab-scale experiments to form solution processed layers of organic photo-active material or interlayers such as PEDOT : PSS.

Figure 2.6 shows a schematic illustration of the spin-coating process. The substrate is held on the spin-coater chuck by suction obtained using a scroll pump. The solution is then dispensed onto the motionless substrate surface using a pipette. An alternative technique, drop casting, uses the same equipment setup but the solution is dispensed onto a rotating substrate. As the substrate is accelerated at a defined rate to a set rotation speed, the centripetal forces evenly distribute the solution across the substrate surface. These forces also remove excess solution from the sides of the substrate. The solvent is evaporated during subsequent rotation of the substrate, leaving a thin film coating. Careful control of the rotation speed, solution concentration and choice of solvent is required. These parameters directly impact layer thickness, uniformity and morphology. Post-deposition drying and annealing steps are also used to influence the morphology of the spin-coated films.
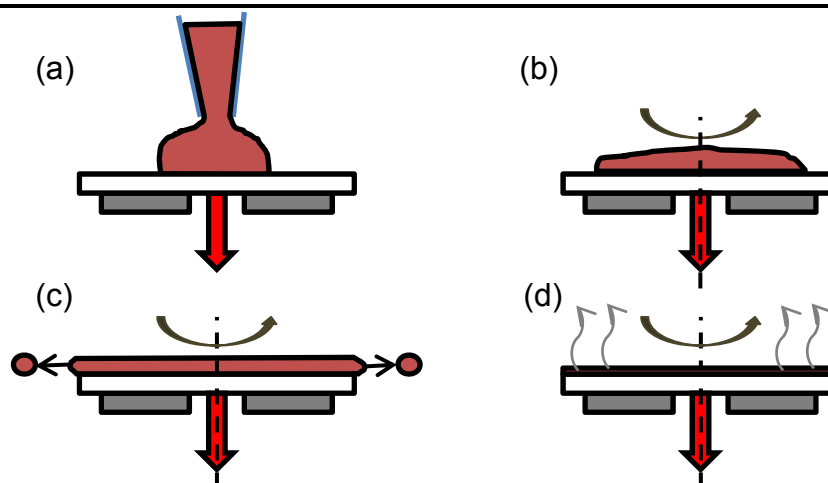
Figure 2.6: Schematic of the spin-coating process: (a) solution dispensed onto substrate, (b) substrate accelerated to even out layer, (c) removal of excess solution and (d) evaporation of solvent.

In this work Laurell Technologies spin-coaters were used in ambient conditions to fabricate PEDOT : PSS and vanadium oxide layers, and in a N_2 filled glovebox to deposit vanadium oxide and P3HT : PCBM films.

2.2 Cell characterisation and testing

OPV cell performance must be measured under defined illumination in order to allow comparisons between the photo-active materials, interlayers, electrodes and reports by other research groups. In this section the equipment required to test cells is described.

2.2.1 Solar simulation

Accurate illumination for the measurement of cell performance is critical to allow fair comparisons to be made between materials or structures. Outdoor testing in sunlight is an obvious illumination source. Unfortunately, daily changes to the intensity of the light received from the sun and variation of weather conditions result

in the need for solar simulation. Solar simulators are commonly used throughout the OPV community, allowing for consistent testing at any time of day.

In order to simulate a particular spectral response we must first consider the solar spectrum, broadly described by the black body radiation that occurs due to the surface temperature of the sun ($\sim$ 5800 K), and the spectral features originating from the passing of photons through the Earth's atmosphere. Figure 2.7 presents common standards of spectral response. Of the three standards that are shown, the first represents the solar irradiance just outside the Earth's atmosphere, indicated by the black line in Figure 2.8. This is known as air mass 0 (AM0).
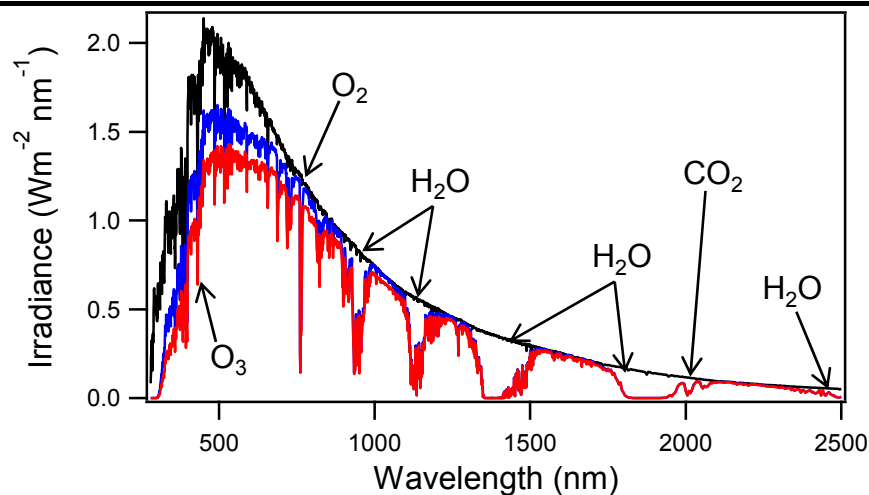
Figure 2.7: Spectral profile of AM0 (black line), AM1.5G (blue line) and AM1.5D (red line), with main atmospheric absorption regions labelled for AM1.5D and AM1.5G.

When photons travel through the Earth's atmosphere, absorption occurs due to O_2, O_3, H_2O, CO_2 and other molecules and particles. The path length for photons travelling through the Earth's atmosphere is minimised at the point the sun is directly overhead, known as the zenith. At this point the path length is defined as having an AM of 1. Any deviation from this point will increase the path length of photons

travelling through the Earth's atmosphere. Figure 2.8 displays the angular dependence of AM, with the relative AM ratio calculated using Equation 2.1.

$$AM = \frac{1}{\cos\theta}$$

<div align="right">Equation 2.1</div>

In order to take a representation of the typical solar irradiance on the surface of the Earth, international standards for the calibration of sources were outlined in the 1980s. One such standard was AM1.5, where the sun is at a 48.2 ° angle to the Earth's surface.[135] Further considerations look solely at direct sunlight, labelled D. Global considerations also take into account scattering, reflections and diffuse sources and are labelled G. Figure 2.7 demonstrates the difference between AM0 (black line), AM1.5D (red line) and AM1.5G (blue line).[3] AM1.5G is the most commonly used standard for measurements, with a light intensity of 100 mW cm^{-2}. In comparison, AM0 has an intensity of 135 mW cm^{-2}.
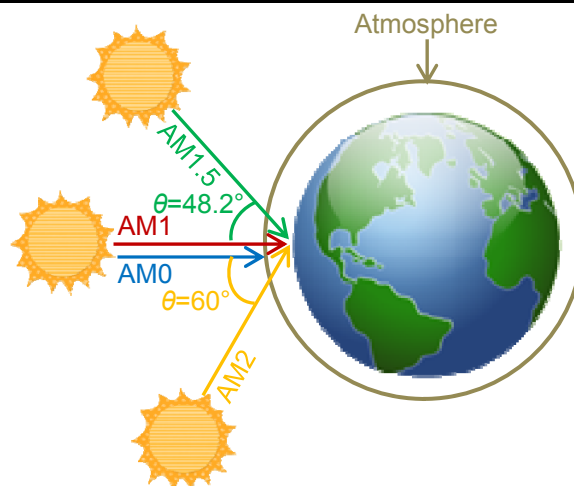
Figure 2.8: Air mass dependence of the angle of the sun to a single point on the Earth's surface.

Careful choice of the source of illumination is required in order to recreate the AM1.5G spectral profile. Mercury and metal halide lamps are utilised by some groups due to their relatively low cost. However, whilst they are able to produce 100 mW cm^{-2}, they have a poor spectral match to the AM1.5G standard. Both contain a large number of sharp, narrow spikes in their spectral profiles. OPV cells are particularly sensitive to spectral mismatches during testing, due to the relatively narrow absorption maxima compared to the broad absorption of inorganic PV cells. Therefore, even small mismatches can have a dramatic effect on the reliability of measurements, especially when comparing photo-active materials or even the same cell architectures fabricated by other research groups using different sources.

A xenon arc lamp is preferential for lab-scale testing, particularly when fitted with spectral filters. The main drawbacks of xenon arc lamps are the high cost and the need to change lamp bulbs at ~ 750 hour intervals. In this report, cell performance measurements and 1 hour degradation tests were carried out using a Newport Oriel solar simulator with a xenon arc lamp and spectral filters. The intensity of the light produced was measured using a Fraunhofer calibrated PVM482 photodiode with a KG-5 filter. Neutral density filters were used to achieve the desired light intensity, typically 100 mW cm^{-2}. 24 hour cell stability measurements were performed using a quartz halogen lamp with additional 450 nm LEDs to improve spectral coverage. The intensity of this source was calibrated using a Si photodiode.

2.2.2 *J-V* Performance characterisation

In order to assess and compare OPV cells, the *J-V* characteristics are measured. These measurements involve sweeping an applied bias across an operational range and measuring the current density produced, either in dark

conditions or / and under illumination. Figure 2.9(a) shows a typical *J-V* curve. Under dark conditions (dotted line) the OPV cell would ideally show diode behaviour, with no current produced at reverse bias and an exponential rise in current for forward bias larger than the cells V_{bi}. When illuminated, (solid line) the *J-V* characteristic is a combination of the dark curve and an offset due to the cells photo-generated current.
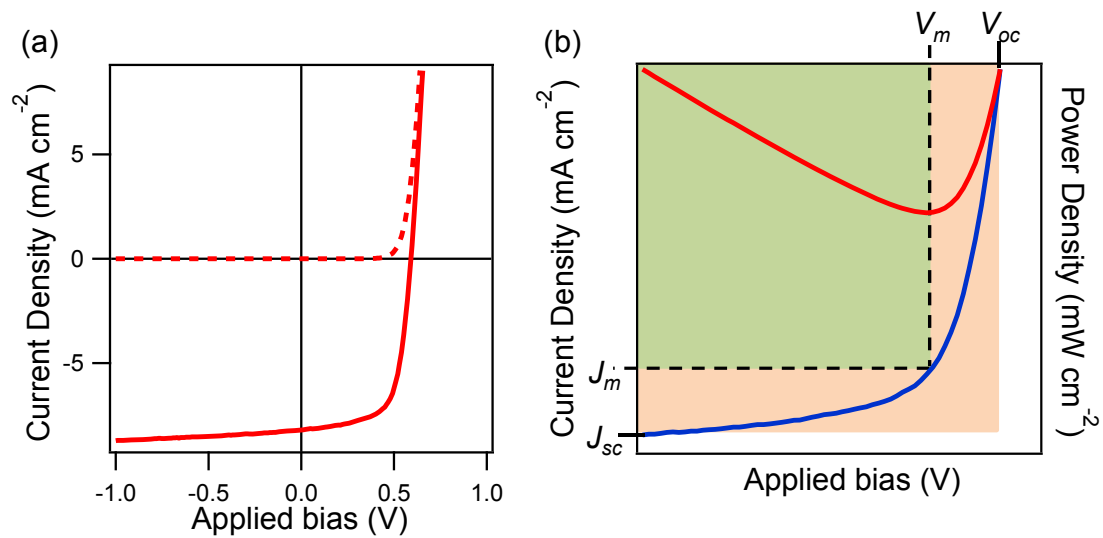
Figure 2.9: (a) Typical *J-V* measurement for an OPV cell, under dark (dotted line) and illumination (solid line) conditions. (b) Fourth quadrant of the *J-V* curve, highlighting key parameters with current density (blue line) and cell power density (red line) against applied bias.

Figure 2.9(b) shows the fourth quadrant of an *J-V* curve, with the key cell parameters V_{oc}, J_{sc}, and the voltage and current density measured at the maximum power point, V_m and J_m respectively. Inverted cells display these key cell parameters in the second quadrant of a *J-V* curve. Figure 2.10 shows an equivalent electric circuit diagram of a cell, including the shunt resistance (R_{sh}), load resistance (R_l) and R_s.
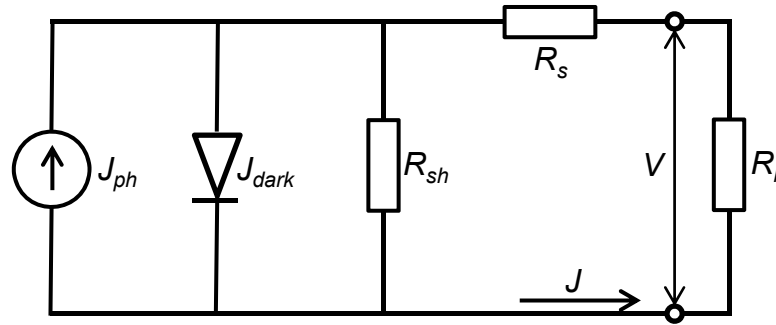
Figure 2.10: Equivalent circuit diagram of a photovoltaic cell with the current source J_{ph}.

The cells V_{oc} is the voltage measured under open circuit conditions, where R_l is infinite. It occurs at the bias where the photocurrent generated is equal to the current flow in the opposing direction, resulting in no net current flow.[136, 137] J_{sc} is found when $V = 0$ V. It indicates the cells photocurrent generation under short circuit conditions, where R_l is 0 Ω.

The maximum power point (P_m) of an OPV cell is achieved at the bias where the product of the cells voltage and current density is highest, $V_m J_m$, with $V_m < V_{oc}$ and $J_m < J_{sc}$. These parameters determine the *FF*, with the relationship in Equation 2.2. The *FF* gives the ideality factor of the *J-V* curve, with *FF* < 1. Higher *FF* values indicate a more square *J-V* shape.

$$FF = \frac{V_m J_m}{V_{oc} J_{sc}}$$

Equation 2.2

The η_p of a cell is defined as the ratio of the maximum power output of the cell to the incident power (P_{inc}). It can be calculated using Equation 2.3.

$$\eta_p = \frac{V_{oc} J_{sc} FF}{P_{inc}} = \frac{V_m J_m}{P_{inc}}$$

Equation 2.3

As shown in Figure 2.10, parasitic resistances R_s and R_{sh} lead to reductions of the cell *FF* and hence lower the η_p of a cell. Figure 2.11 gives an illustration of the effect that these parameters can have on the *J-V* curve of a cell. Ideally, R_s should be close to 0 Ω. The resistance encountered at contacts and through the photo-active layer commonly increases R_s. On the other hand, it is desired that R_{sh} is infinite, with the reduction of R_{sh} caused by current leakage due to pin holes in the cell, non ideal leaky contacts and charge recombination.[37, 138]
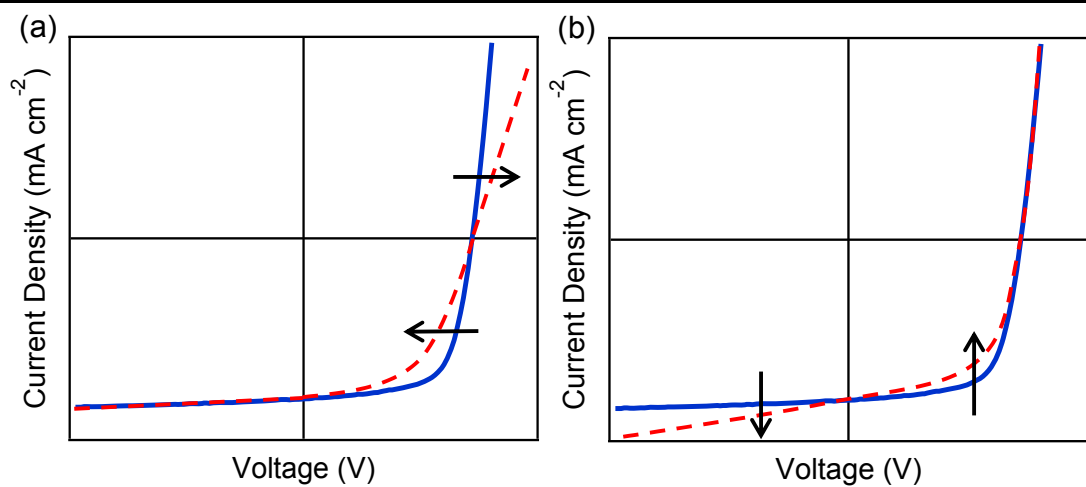
Figure 2.11: The effect of parasitic resistances on cell *J-V* curves: (a) an increase in R_s from the blue solid *J-V* curve to the dotted red, (b) a reduction in R_{sh} from the blue solid *J-V* curve to the dotted red.

All *J-V* measurements were collected using a computer controlled Keithley 2400 sourcemeter, connected to a Labview program written by Dr Paul Sullivan. Cells were loaded into a custom cell test holder that was held under a N_2 atmosphere unless stated otherwise. Contact was made to each of the cell pixels and ITO. Degradation measurements were carried out in the same manner, with constant illumination and the collection of one *J-V* curve per minute.

2.2.3 External quantum efficiency measurements

External quantum efficiency (*EQE*) measurements indicate the current generation of an OPV cell at individual incident monochromatic wavelengths. An *EQE* spectrum therefore provides the spectral response of a cell. The measurement can be used as an indication of the relative performance of the photo-active materials, demonstrating exactly how much photocurrent each material contributes to the J_{sc} of the cell. *EQE* measurements can be used in cell and material development to suggest strategies that minimise the spectral overlap of photo-active materials and increase the spectral coverage of cells. *EQE* spectra can also highlight any problems of a given OPV cell architecture, such as detrimental optical effects.[111]

An *EQE* measurement gives the ratio of the charges generated by an OPV cell for each incoming photon of light at a specific wavelength (λ), using the relationship in Equation 2.4

$$EQE(\lambda) = \frac{J_{sc}(\lambda)}{qN(\lambda)}$$

Equation 2.4

where *q* is the elementary charge and *N(λ)* is the monochromatic incident photon flux density. In order to measure an *EQE* for an OPV cell, a Si photodiode with a known spectral response has to be used as a reference. The current generation of the reference ($J_{sc}(\lambda)_{(ref)}$) is measured at each λ. The OPV cell current generation ($J_{sc}(\lambda)_{(OPV)}$) is then measured in the same manner. The known spectral response of the reference ($EQE_{(ref)}$) allows for determination of the OPV cell *EQE* response ($EQE_{(OPV)}$) using Equation 2.5.

$$EQE_{(OPV)} = \frac{EQE_{(ref)} \times J_{sc}(\lambda)_{(OPV)}}{J_{sc}(\lambda)_{(ref)}}$$

Equation 2.5

The experimental *EQE* setup utilised a Sciencetech SF150 xenon arc lamp as the light source, with a PTI monochromator. The monochromatic light intensity was calibrated using a Newport 818-UV Si photodiode reference. The light was chopped at 510 Hz, with signal detection controlled using a Femto DHPCA-100 current-voltage preamplifier and Stanford Research SR830 DSP lock-in amplifier. Data collection was controlled by a Labview program written by Dr Paul Sullivan. OPV cells were typically tested between 350 - 800 nm, dependent on the photo-active materials used.

2.3 Material and thin film analysis

In this section the analysis techniques used for the characterisation of thin layers of material are briefly outlined. These techniques are key for further understanding of trends seen for the OPV cells in this report. The techniques provide additional information on how specific cell architectures function and highlight the material properties that are desired to increase OPV performance.

2.3.1 Kelvin Probe

The Kelvin probe (KP) is a non-contact technique used to measure the work function of a surface. The work function is described in Section 1.4.2. The technique is schematically illustrated in Figure 2.12. A Kelvin probe measures the contact potential difference (V_{CPD}) between a sample and an oscillating tip, calibrated against a reference material.
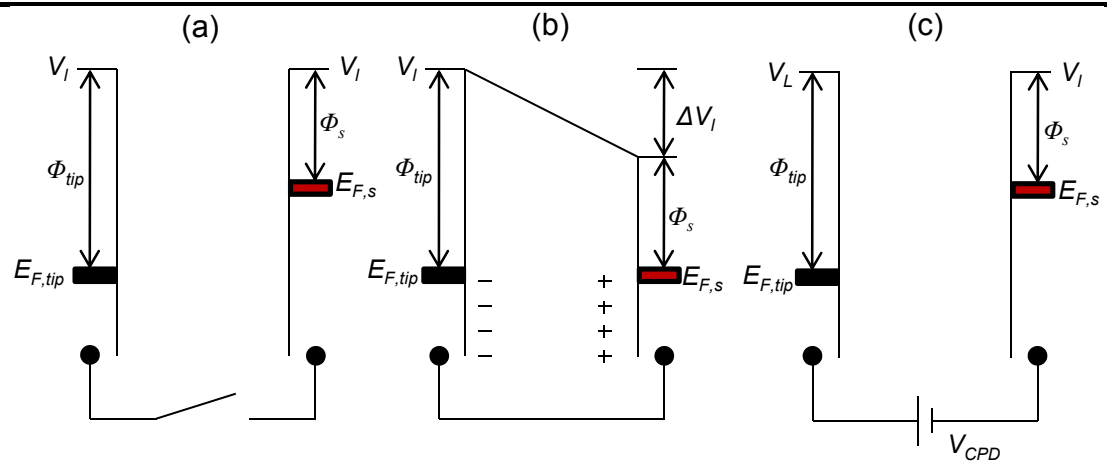
Figure 2.12: Schematic illustration of the Kelvin probe technique. (a) Two materials not connected, (b) when connected electron transfer occurs, (c) when the applied dc bias, V_b, is equal to the V_{CPD} of the materials then no charge transfer occurs.

When the sample and metal probe are not connected they share a common V_l, as shown in Figure 2.12(a). When two materials with different work functions are connected, electrons flow from the material with the lower work function to that with the higher value. This charge transfer leads to the formation of an electric field between the probe and surface, shown in Figure 2.12(b). By mounting the oscillating probe just above the sample, the output voltage will fluctuate periodically with the oscillations of the probe. The peak to peak voltage depends on the difference in capacitor potential (V_c) and the external backing potential (V_b). This can be monitored using an oscilloscope. The V_b is applied to the capacitor until the point where the charging between probe and surface disappears and a null signal is seen. This is shown in Figure 2.12(c).[139] The V_b required to achieve this is equal to the V_{CPD}, and allows the work function of the sample to be calculated against the graphite reference.

All Kelvin probe measurements were performed under a N_2 atmosphere, against freshly cleaved highly ordered pyrolytic graphite (HOPG) reference. The signal was monitored on an oscilloscope.

2.3.2 Ultra-violet photoemission spectroscopy

The electronic characteristics of the materials used in an OPV cell need to be measured in order to gain a greater understanding of energetic factors influencing cell performance. The energetic properties of the interfaces between layers in particular often govern the performance of cells, and therefore require explicit investigation. Whilst a Kelvin probe can be used to provide just a surface work function value, ultra-violet photoemission spectroscopy (UPS) can determine the work function and the ionisation potential of a semiconducting sample. By using a vacuum system with both a deposition chamber and a UPS, the changes to the electronic structure of materials can be probed *in-situ* with the sequential fabrication of layers. This gives a substantial insight into properties of a particular system.[140, 141]

In UPS measurements, a sample is held under vacuum and is irradiated with high energy monochromatic light. If the energy of the photons is large enough to cause the emission of an electron from the sample, then the kinetic energy (E_{KE}) of the emitted electron can be measured using a detector. Since the energy of the incident photons and the kinetic energy of the electron are known, the binding energy (E_B) of the valence state that the electron was emitted from can be calculated.[140] Figure 2.13 gives a simplistic schematic of this process, with the kinetic energy given by Equation 2.6.

$$E_{KE} = h\nu - E_B$$

Equation 2.6
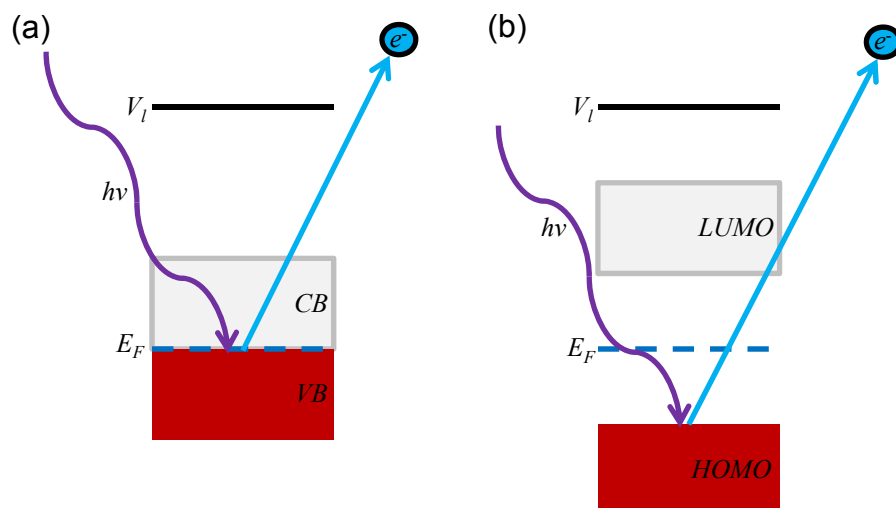
Figure 2.13: Electron photoemitted from (a) a metal and (b) an organic semiconductor.

For a metal, the electron emitted with the highest kinetic energy is excited from the material's Fermi level. This provides the work function from the relationship in Equation 2.7.

$$\phi = h\upsilon - E_{KEmax} \qquad\qquad \text{Equation 2.7}$$

However, the electron emitted with the highest kinetic energy from a semiconductor is excited from the top of the valence band, or in the case of organic semiconductors, the HOMO level. This gives the ionisation potential value using Equation 2.8.

$$IP = h\upsilon - E_{KEmax} \qquad\qquad \text{Equation 2.8}$$

To clearly illustrate how to obtain these values from the features of a UPS spectrum, an example experiment is shown in Figure 2.14. The work function of a material is obtained from the secondary electron cut-off, shown in Figure 2.14(b). In a metal, excitations from the top of the valence band are from the Fermi level of the

material. Therefore, metals will display excitations with 0 eV binding energy in the valence band spectrum. However, for semiconductors the position of the HOMO level or the valence band is displayed in relation to the materials Fermi level in the valence band spectrum, illustrated in Figure 2.14(c). This results in the onset of the HOMO or valence band being measured at an additional binding energy, E_{ABE}, below the materials Fermi level. Consequently, to find the *IP* of the semiconductor experimentally, the work function value has to be added to this additional binding energy, described by Equation 2.9.

$$IP = \phi + E_{ABE} \qquad\qquad \text{Equation 2.9}$$
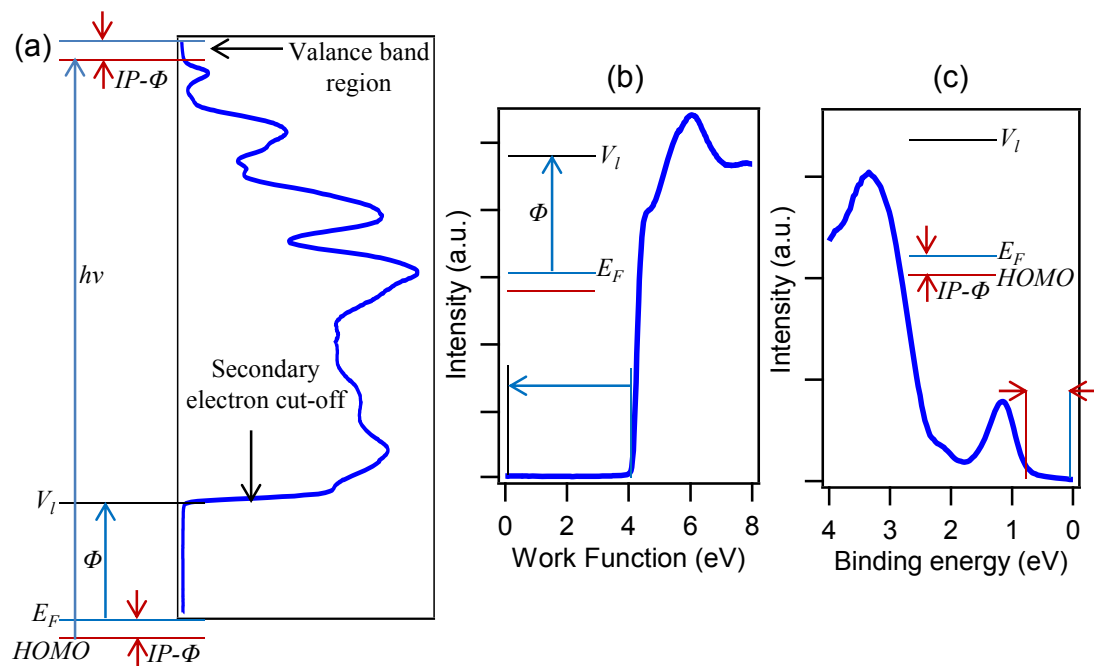
Figure 2.14: Example UPS spectrum of 5 nm CuPc deposited onto an ITO substrate. (a) valence band and secondary electron cut-off areas of the spectrum connected to form a continuous spectrum. Typical presentation of measurements for (b) secondary electron cut-off and (c) valence band regions. Inset are the relevant energy level schematics for each figure.

In this work, UPS measurements were carried out in-situ using a custom multi-chamber UHV system with a base pressure of ~ 1 x 10^{-10} mbar. Spectra were recorded using a SPECS PHOIBOS 100 hemispherical electron energy analyser. Samples were excited with 21.21 eV radiation from a He I plasma source.

2.3.3 X-ray photoelectron spectroscopy

Many of the electrode materials, interfacial layers and even photo-active layers used in the fabrication of OPV cells are either doped or contain a mixture of materials. Since the composition of a surface determines many of its properties, a method for analysing the composition is desirable. The development of high resolution X-ray photoelectron spectroscopy (XPS) won Kai Siegbahn the physics Nobel prize in 1981. XPS is a technique that provides information on the elemental composition and the electronic states of the elements which make up the surface.[140]

XPS relies on many similar principles to UPS. A sample is held under vacuum and irradiated with high energy monochromatic photons, leading to the emission of electrons from the sample. Thus, Equation 2.6 that describes the determination of the binding energy of an emitted electron, can be used for both techniques. However, the energy of the source is far higher in XPS, irradiating the sample with 1486.6 eV X-rays in experiments performed here, compared to the UPS source that produces photons of 21.21 eV. This allows XPS to survey the core levels of atoms, as schematically shown in Figure 2.15. The binding energy of core levels probed by XPS are characteristic of a specific electron orbital for a particular atom. The binding energy of atoms increases with atomic number. Binding energy also increases for orbitals closer to the nucleus, for example the E_B of 1s > 2s. The environment the atom is within will also determine the exact binding energy of an electron and so provide additional information.[142, 143]
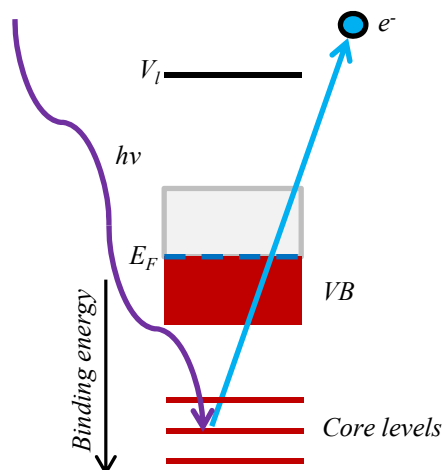
Figure 2.15: Illustrative schematic of an electron photoemitted from a core levels using XPS.

The penetration depth of X-rays is up to several micrometres. However, the main peaks in an XPS spectrum are due to photoelectron emission from the samples surface region, with a depth of up to 10 nm. These emitted electrons exhibit the characteristic binding energy of the atoms core levels. For the top few nanometres of the sample, nearest the surface, electrons are able to escape into vacuum without collision before detection, hence maintaining their initial kinetic energy. Deeper into the sample, emitted electrons are likely to collide and so lose some of the initial kinetic energy. Since these electrons will be detected with this lower kinetic energy and consequently higher binding energy, they will contribute to the XPS spectra as a continuous background of inelastically scattered electrons. Each subsequent photoelectron peak leads to additions to the background of inelastically scattered photoelectrons, producing a step-like background. Hence, background subtractions such as that devised by Shirley are a necessity in the analysis of XPS peaks.[144] An example XPS spectra for illustrative purposes is shown in Figure 2.16.
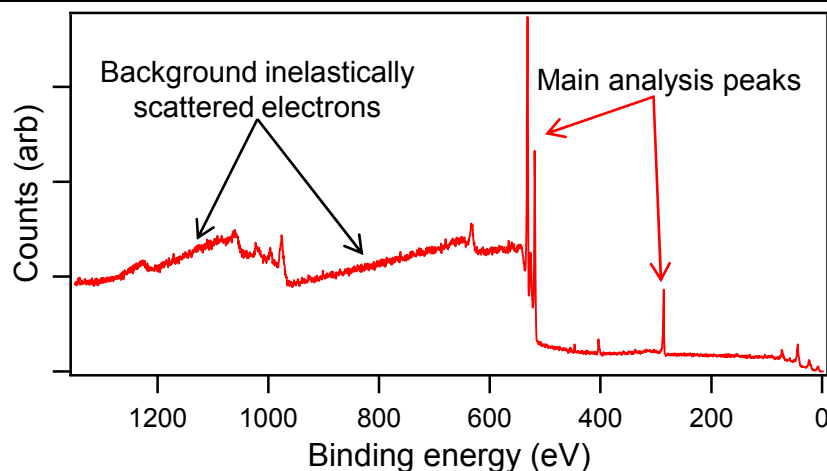
Figure 2.16: Example XPS survey scan for solution processed vanadium oxide on an ITO substrate.

The XPS measurements in this work were carried out *ex-situ* after loading into a UHV system with a base pressure ~ 5 x 10^{-11} mbar. The sample was illuminated with X-rays from a monochromated Al kα source (hv = 1486.6 eV), with the photoelectrons detected at a 45 ° take off angle using an Omicron Sphera electron analyser. Analysis was performed using CasaXPS before exporting files to Igor Pro.

2.3.4 Electronic absorption spectroscopy

Determining the transmittance or absorption of a layer is essential for assessing the potential factors behind the performance of an OPV cell. The spectral coverage of a photo-active materials absorption can be measured using electronic absorption spectroscopy. This measurement gives an indication of the compatibility of the donor and acceptor materials from the absorption profiles, and the layer thicknesses of each required for satisfactory absorption. It is important to determine the transmittance of both electrodes and interlayers in order to highlight any possible

overlap with the absorption of photo-active materials. In addition, the electronic structure and optical band gap of the materials can be deduced.

The absorption of a photon by a thin film is wavelength dependent. In a typical electronic absorption measurement, a wide range of visible and ultra-violet (UV) wavelengths are scanned in order to give an absorption profile. If the energy of a photon matches an allowed transition of the material, an excitation can occur. By measuring quantitatively the incident light intensity (I_0) and the reduced transmitted light intensity (I), absorption (A) can be calculated. The molar absorption coefficient (ε) of a solution with a known molar concentration (c) and path length (l), can be extracted using the Beer-Lambert law in Equation 2.10.

$$A = \log\frac{I_0}{I} = \varepsilon l c \qquad \text{Equation 2.10}$$

In a solid, the product of the molecular mass and the density of a material can be substituted for concentration. The absorption coefficient (α) of the material is produced from the concentration and molar absorption coefficient. Therefore, by measuring the absorption of a solid with film thickness L, the absorption coefficient can be calculated from the modified Beer-Lambert law in Equation 2.11.

$$A = \log\frac{I_0}{I} = \alpha L \qquad \text{Equation 2.11}$$

The transmittance (T) of a solid film is determined by the relationship for transmitted light to incident light in Equation 2.12.

$$T = \frac{I}{I_0} = 10^{-\alpha L} \qquad \text{Equation 2.12}$$

The UV / vis electronic absorption measurements in this work were carried out using a Perkin-Elmer Lambda 25 spectrometer, typically scanning from 350 - 900 nm dependent on sample. Scans were taken against either an ITO or air background, stated where appropriate.

2.3.5 Atomic force microscopy

The AFM was invented by Binnig, Quate and Gerber in 1986 as a method for imaging surface topography on a nano-scale.[145] Basic AFM uses a tip on the end of a cantilever to interact with a surface and create a three dimensional map of the morphological surface features. The technique is highly versatile and can be used on a range of surfaces, from hard conductive materials to biological samples. For the development of OPV cells AFM is typically used to give an understanding of surface topography, the size of features and the roughness of surfaces. This routine characterisation technique is carried out on electrodes, interlayers and photo-active materials. AFM experiments highlight nano-scale morphological changes that can influence the performance of cells. As stated in Section 2.1.3.4, step edge AFM measurements allow for the calibration of film deposition thicknesses. Specialist AFM techniques have been used to study OPV photo-active material properties, such as photo-conductive measurements.[146]

When an AFM cantilever is brought close to a surface, the tip with a nanometre scale radius will be influenced by both attractive and repulsive forces. Attractive forces, such as electrostatic and van der Waals, have a relatively long range dependence and so dominate the tip to sample interaction on approach to the surface. This results in the tip snapping towards the surface, bending the cantilever towards the sample. As the z-piezo moves the cantilever closer to the surface, short range repulsive forces dominate. These include hard sphere repulsion and electron-

electron Coulombic interaction. The repulsive forces cause the cantilever to bend in the opposite direction, with a linear deflection of the cantilever to the force applied. Since the tip and cantilever together act as a spring with a measureable spring constant, the tip-sample forces obey Hooke's law.

A schematic illustration of the Asylum Research MFP-3D AFM used in this report is shown in Figure 2.17. The AFM head is lowered towards the sample to a point where the cantilever is visibly just above the sample surface. A laser is reflected off the cantilevers coating and directed using a positioning mirror onto a photo-detector. This allows for sub-nanometre tracking of the cantilevers motion. The position of the cantilever is relayed to the controller. A set point for the deflection or amplitude of the cantilevers motion is typically kept constant by the controller. A feedback loop adjusts the cantilevers position using the z-piezo to maintain the setpoint. In order to build a three dimensional image of the surfaces topography, the sample is moved in a two dimensional ortho scanning motion by the x and y piezos.

Two main modes of AFM operation can be used in order to obtain a three dimensional surface topography plot. In contact mode, the deflection of the cantilever is kept constant as it moves over surface features, with a repulsive interaction between the tip and sample. The controller uses a feedback loop with the z-piezo to adjust the cantilevers position for any changes in deflection. Whilst contact mode is fast and easy to execute, it possesses several disadvantages. Due to the frictional forces between the tip and sample, the tip can be damaged or easily pick up debris off the sample surface. The lateral forces of to tips movement along the surface can also cause considerable damage to soft surfaces, such as the organic photo-active layers used in OPV cells.
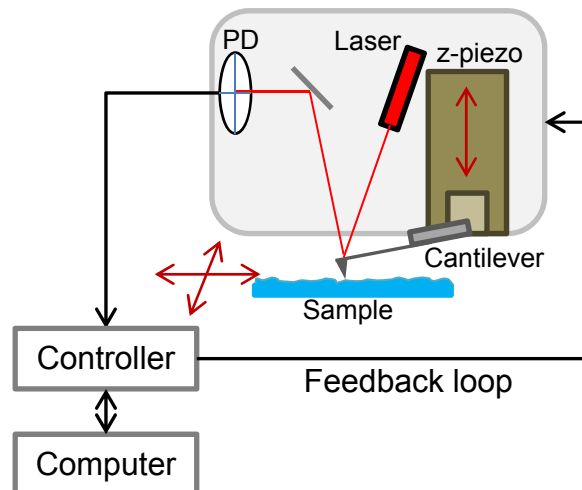
Figure 2.17: Schematic representation of an Asylum Research MFP-3D AFM. Photo-detector abbreviated PD.

The other commonly used mode is known as alternating contact (AC). The cantilever is oscillated near its resonant frequency, producing a free air amplitude of oscillation. The cantilever is brought closer to the surface by the z-piezo, with interactions between the tip and surface leading to a damping of the oscillation. An amplitude set point is selected by the user for imaging. The controller ensures the amplitude is kept constant as the tip moves over surface features, using the z-piezo and feedback loop. This technique is less destructive to soft surfaces and thus ideal for imaging softer samples.

Throughout this report, an Asylum Research MFP-3D AFM was used in AC mode for surface topography measurements. The MFP-3D was used in combination with a Asylum Research ARC2 controller. The measurements were carried out in a AEK2002 acoustic isolation enclosure containing a vibration isolation table. Olympus AC240-TS Si cantilevers were used with a resonant frequency of 70 kHz

and nominal tip radius of 9 nm. Data acquisition and analysis utilised a Asylum Research add-on for Igor Pro.

2.3.6 X-ray diffraction

A crystal is comprised of repeating structural motifs of atoms, molecules or ions. A unit cell is the smallest repeating unit of a crystal and can be described by its lattice parameters. These are the length of the cell edges in three dimensions, a, b and c, and the angles between the unit cell edge vectors, α, β, γ. A unit cell will be one of 14 possible Bravais space lattices. The points where a plane intercepts the unit cell forming crystal planes on its crystallographic axis, can be expressed using the Miller indices, *hkl*. The Miller indices provide the reciprocal of the intersection distances of the crystal plane, $1/h$, $1/k$ and $1/l$, removing the need for fractions in labels. Miller indices are useful for finding the separation of parallel planes, identified as the interplanar spacing, d_{hkl}.[38]

If the lattice planes of a crystal are regarded as a mirror, then reflection of incoming photons will result in both constructive and deconstructive interference. X-ray diffraction (XRD) is a technique that uses this principle, detecting the reflection of incident X-rays on a surface. When reflecting incoming X-rays from two lattice planes the difference in path lengths is given by AB + BC, as illustrated in Figure 2.18(a). In order to obtain constructive interference of the X-rays with a crystal spacing of d_{hkl}, the difference between the path lengths must equal an integer number of wavelengths. Therefore, deconstructive interference will occur when Equation 2.13 is true.

$$AB + BC \neq n\lambda \qquad \qquad \text{Equation 2.13}$$

When constructive interference does occur, d_{hkl} can be calculated from the path length of the constructive waves given by Bragg's law in Equation 2.14.

$$n\lambda = 2d_{hkl}\sin\theta \qquad\qquad \text{Equation 2.14}$$

Where θ is the glancing angle of incidence and n is the order of reflection.
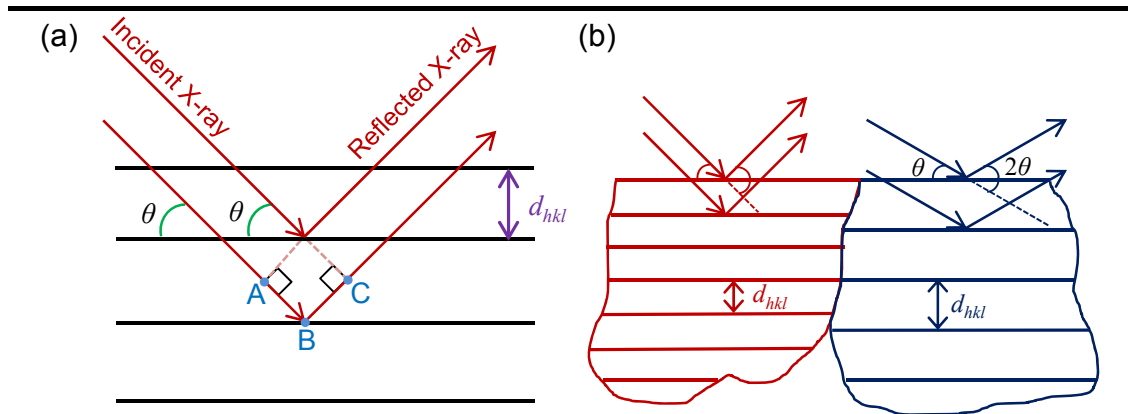
Figure 2.18: Schematic of (a) Bragg diffraction and (b) powder diffraction of two regions with different d_{hkl} spacings.

Unlike many inorganic semiconductors, organic thin films are typically polycrystalline with random orientations of relatively small crystal domains. Thus, the powder XRD technique is usually used to reveal the preferential orientation of diffraction planes parallel to the surface. The powder XRD method is often described as θ - 2θ, as the angle of incidence and reflection are both at θ to the surface leading to the output of a 2θ scan. The X-ray angle of incidence and detection is varied in relation to the surface allowing for detection of a range of d_{hkl} values, as shown in Figure 2.18(b). Where coherent interference of the monochromatic X-rays is detected, a peak at the 2θ angle is displayed. The intensity of the peak is dependent on the number of crystallites with the d_{hkl} spacing.

In this work, XRD analysis was carried out using a PANalytical X'Pert PRO diffractometer with Cu Kα radiation on samples prepared on an ITO substrate. Sample details are described in later chapters.

Chapter 3: The impact of a MoO$_x$ hole extracting layer on OPV cells

This chapter explores the impact of inserting a MoO$_x$ hole extracting layer into small molecule OPV systems. Whilst the polymer community regularly uses solution processed hole extracting layers to enhance cell performance, there have been few reports of thermally evaporated equivalents for small molecule OPV architectures. The effect of inserting a MoO$_x$ layer into several different donor / fullerene systems was examined using cell fabrication and testing. The factors influencing the performance of each cell were determined using a combination of techniques, including AFM, UV-vis absorption spectroscopy and UPS.

3.1 The MoO$_x$ layer in the ClAlPc / C$_{60}$ OPV system

3.1.1 MoO$_x$ layer thickness optimisation for the ClAlPc / C$_{60}$ OPV system

A series of MoO$_x$ layer thicknesses were thermally evaporated onto ITO, varying from 2.5 nm to 50 nm. Photo-active materials were then deposited, with deposition on bare ITO used as a reference (supplied by Psiotech throughout this chapter). 20 nm of ClAlPc was used as the donor layer, with 40 nm C$_{60}$ used as the acceptor layer. This structure has previously been optimised in both literature reports and by the Jones group.[16, 110] An 8 nm BCP film was used as an exciton blocking layer, with Al as the top contact. ClAlPc was chosen as the donor material due to its relatively high ionisation potential of 5.4 eV. This produced an effective interface gap of 1.15 eV with the C$_{60}$ acceptor material, and therefore a large V_{oc} was expected for the system.[110]
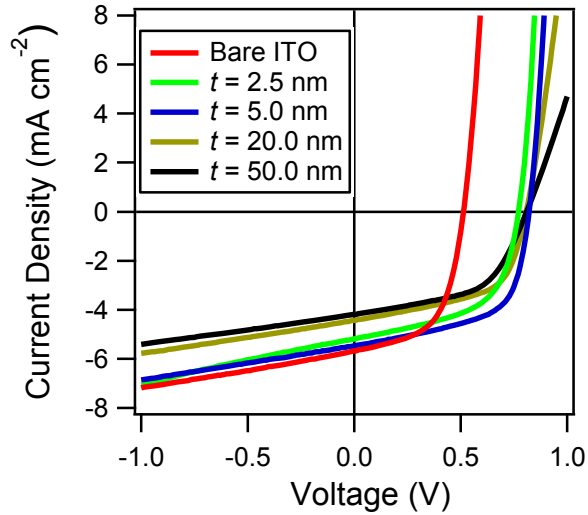
Figure 3.1: *J-V* curves obtained under 1 sun illumination for cells with structure ITO / *t* nm MoO$_x$ / 20 nm ClAlPc / 40 nm C$_{60}$ / 8 nm BCP / Al, with *t* varied between 0 and 50 nm.

J-V curves and key cell performance parameters are displayed in Figure 3.1 and Table 3.1 respectively. When deposited on bare ITO, the ClAlPc / C$_{60}$ cells had a V_{oc} of 0.51 V, a J_{sc} of 5.68 mA cm^{-2} and a *FF* of 0.57. Consequently, the η_p was 1.65 %. When utilising a 2.5 nm MoO$_x$ layer with the same photo-active materials, the cell η_p increased to 2.20 %. This was predominantly due to an enhancement in V_{oc} to 0.77 V, however both J_{sc} and *FF* decreased to 5.19 mA cm^{-2} and 0.55 respectively. With the insertion of a 5 nm MoO$_x$ layer, η_p was further increased to 2.60 %. This was due to a small improvement in V_{oc} to 0.82 V, a J_{sc} of 5.46 mA cm^{-2} and a *FF* of 0.58. Increasing the MoO$_x$ layer thickness beyond 5 nm did not lead to an increase in V_{oc}, but did increase R_s and transmittance losses, consequently compromising the *FF* and reducing J_{sc} and leading to a concomitant loss of η_p. A 50 nm MoO$_x$ layer gave a η_p of 1.79 %, due to a substantially reduced J_{sc} of 4.02 mA cm^{-2}. The optimum layer thickness of thermally evaporated MoO$_x$ for these cells was therefore determined to be ~ 5 nm. Since the cell performance increased from bare ITO to 5 nm of MoO$_x$, it

suggests that the 2.5 nm thick layer of MoO$_x$ does not give a complete coverage of the ITO surface. This was reflected in the V_{oc} for cells containing the 2.5 nm layer of MoO$_x$ (0.77 V). This V_{oc} was between the values for bare ITO (0.51 V) and 5 nm of MoO$_x$ (0.82 V), although closer to the value of the 5 nm layer.

Table 3.1: Summary of cell performance parameters obtained for OPV cells with the architecture ITO / t nm MoO$_x$ / 20 nm ClAlPc / 40 nm C$_{60}$ / 8 nm BCP / Al.

MoO$_x$ thickness t (nm)	J_{sc} (mA cm^{-2})	V_{oc} (V)	FF	η_p (%)
0	5.68 ± 0.20	0.51 ± 0.03	0.57 ± 0.01	1.65 ±
2.5	5.19 ±	0.77 ±	0.55 ±	2.20 ±
5	5.46 ± 0.10	0.82 ± 0.01	0.58 ± 0.01	2.60 ±
10	4.68 ± 0.10	0.81 ± 0.01	0.58 ± 0.03	2.20 ±
20	4.43 ± 0.05	0.81 ± 0.01	0.56 ± 0.01	2.01 ±
50	4.02 ± 0.05	0.81 ± 0.01	0.55 ± 0.03	1.79 ±

Other researchers have reported a similar optimum layer thickness of MoO$_x$ when used in other OPV systems.[107, 112] The optimum was however considerably thinner than the 50 nm reported by Kinoshita *et al.* with tetraphenylporphine (H$_2$TPP) / C$_{60}$ small molecule OPV cells.[147]

3.1.2 Characterisation of the MoO$_x$ layer

To assess the properties of the 5 nm MoO$_x$ hole extracting layer, UV-vis absorption spectroscopy and AFM studies were performed. One factor in determining the suitability of a hole extracting material is the transparency of the layer across the regions in which the relevant photo-active materials absorb. Figure 3.2 shows the transmittance of bare ITO and ITO / 5 nm MoO$_x$ taken against an air background. Since the majority of small molecule and polymer photo-active materials absorb between 400 - 900 nm, any absorption due to the MoO$_x$ layer in this

region could lead to a decrease in cell J_{sc}. Figure 3.2 shows the largest loss in transmittance for the 5 nm MoO$_x$ layer (~5 %) to be a broad feature centred around 492 nm, with a small overall loss between 420 - 600 nm. A more significant loss was seen below 360 nm. A small gain in transmittance compared to bare ITO can be seen centred at 383 nm. This was likely to be due to lower reflectance compared to bare ITO in this region.[148]

MoO$_x$ is commonly reported to be a wide band gap metal oxide,[107, 149] therefore the excellent transmittance demonstrated across visible wavelengths should be expected. The onset of the MoO$_x$ absorption edge resulted in the loss of transmittance below 360 nm. Equation 3.1 indicates the relationship between α, the energy of an incoming photon, E, and the band gap of a layer.[149] In order to estimate the band gap of the MoO$_x$ layer, a plot of $(E \times \alpha)^{1/2}$ against energy for a MoO$_x$ layer against an ITO background is presented in the inset of Figure 3.2. The measurement revealed a 3.4 eV band gap for the MoO$_x$ layer.

$$\alpha \propto \frac{1}{E} \cdot (E - E_g)^2 \qquad\qquad \text{Equation 3.1}$$

The small loss in J_{sc} for the ClAlPc / C$_{60}$ cells using the optimised MoO$_x$ layer can be attributed to the overlap of C$_{60}$ absorption and the broad MoO$_x$ absorption peak at 492 nm, in addition to other minor losses between 400 - 900 nm.
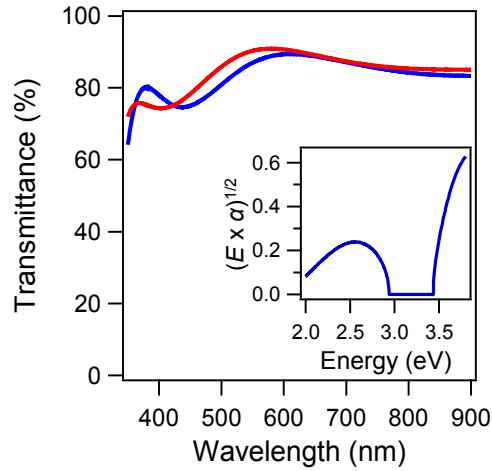
Figure 3.2: Transmittance of bare ITO (red line) and ITO / 5 nm MoO$_x$ (blue line). Inset: plot of $(E \times \alpha)^{1/2}$ against energy for a 5 nm MoO$_x$ layer against an ITO background.

The morphological features of ITO, ITO / 5 nm MoO$_x$ and ITO / 20 nm MoO$_x$ are shown in Figure 3.3. The surface roughness (R_q) of ITO was 4.1 nm, with peak to peak variation of ~ 20 nm. With 5 nm of MoO$_x$ thermally evaporated on to the ITO the R_q remained very similar at 4.0 nm. Of particular note, the morphological features seen on the bare ITO surface topography were still prevalent even with the 5 nm MoO$_x$ layer. This was contrary to the island growth of MoO$_x$ reported by Shrotriya *et al.*, where MoO$_x$ increased the surface roughness of the sample.[107] The report showed an increase in R_q from 1.6 nm measured on bare ITO, to 6.9 and 7.2 nm for film thicknesses of 3 nm and 10 nm of MoO$_x$ respectively. Here, even with 20 nm of MoO$_x$ (Figure 3.3(c)) the R_q was only 4.6 nm, with the sample displaying similar surface features to bare ITO. This demonstrated that the MoO$_x$ layer covered the relatively rough ITO surface homogeneously. The hole extracting layer did not increase the interfacial surface area with the donor material that may otherwise encourage nanostructuring, or create large features which may lead to pin holes.
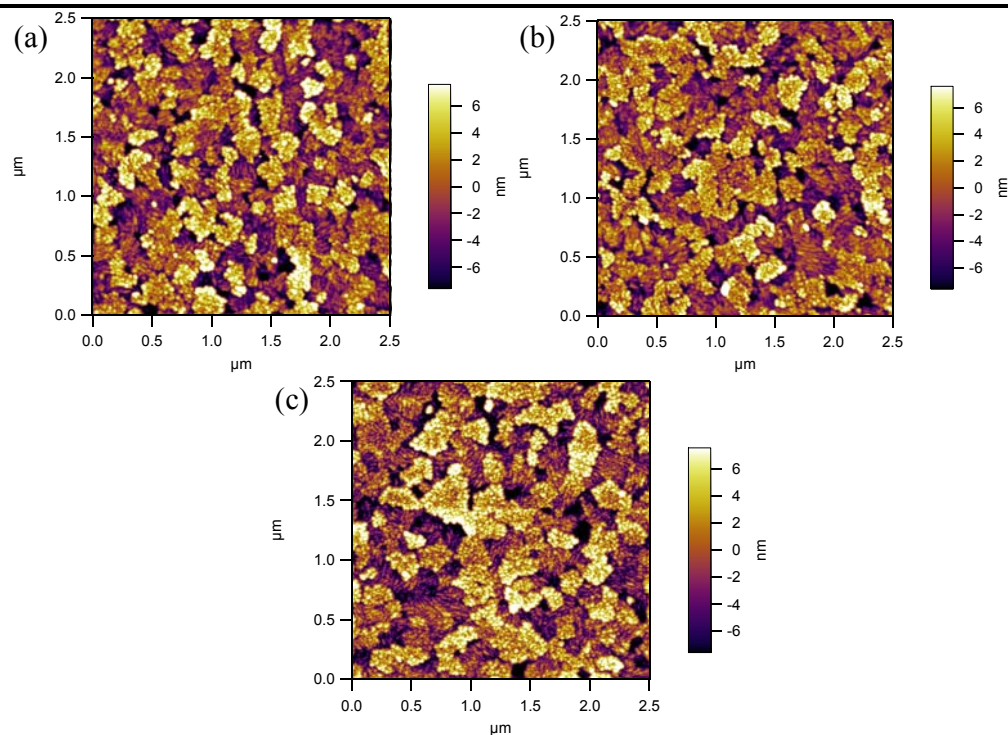
Figure 3.3: 2.5 µm AFM topographical images of bare ITO (a), ITO / 5 nm MoO$_x$ (b) and ITO / 20 nm MoO$_x$ (c). All images have the same height scale (± 7.5 nm).

3.1.3 Impact of the MoO$_x$ layer on ClAlPc growth

The possible factors influencing the changes in ClAlPc / C$_{60}$ cell performance were explored. To establish whether the changes in cell performance could be attributed to any modification of the structure or morphology of the ClAlPc layer by the MoO$_x$ layer, AFM, UV/vis absorption spectroscopy and XRD measurements were obtained.

Thin layers (5 nm) of ClAlPc were deposited on to both bare ITO and ITO / 5 nm MoO$_x$. The AFM images displaying the surface topography of these layers are shown in Figure 3.4.
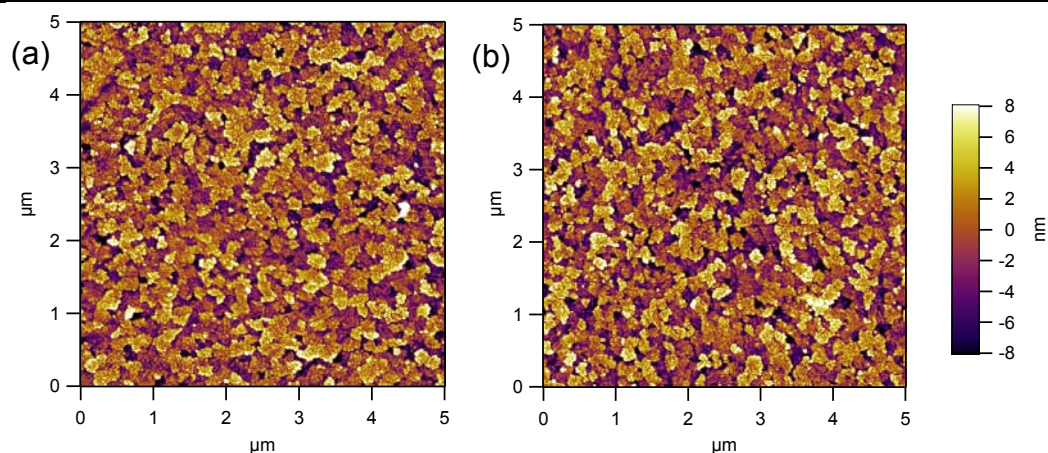
Figure 3.4: 5 µm AFM topographical images of (a) ITO / 5 nm ClAlPc and (b) ITO / 5 nm MoO$_x$ / 5 nm ClAlPc. All images have the same height scale (± 8 nm).

No significant change in the morphology of the ClAlPc layer was seen when deposited on to the MoO$_x$ film, with the AFM images showing comparable topography to the bare ITO, just as with the MoO$_x$ layer on ITO. The images gave R_q values of 3.9 nm and 4.0 nm for ITO / 5 nm ClAlPc and ITO / 5 nm MoO$_x$ / 5 nm ClAlPc respectively. The topographical images therefore show no obvious change in the ClAlPc crystallinity or layer growth due to MoO$_x$.

To complement the AFM studies, UV/vis absorption spectra of ITO / 20 nm ClAlPc and ITO / 5 nm MoO$_x$ / 20 nm ClAlPc were obtained against an ITO reference background. Figure 3.5 indicates the ClAlPc layer had an absorption maximum at 740 nm with a smaller shoulder at 670 nm, and was similar for both samples. The main peak at 740 nm is due to ClAlPc aggregates, with the shoulder at 670 nm due to monomer ClAlPc, as presented for ClAlPc solutions by Chauhan *et al.*[150] The marginal increase in absorption between 800 and 900 nm for the ClAlPc layer on the MoO$_x$ films can be attributed to the additional absorption due to MoO$_x$.

Therefore, MoO$_x$ was perceived to have a negligible effect on the packing of the ClAlPc layer.
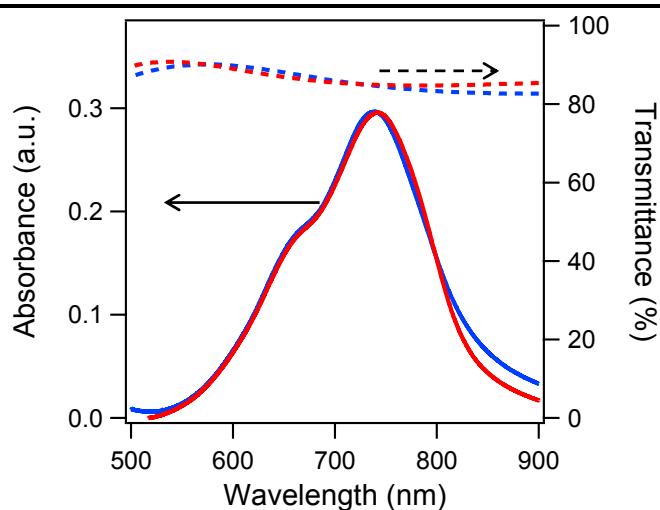
Figure 3.5: UV/vis absorption data for ITO / 20 nm ClAlPc (red line) and ITO / 5 nm MoO$_x$ / 20 nm ClAlPc (blue line) against an ITO background scan. ITO (red dotted) and ITO / 5 nm MoO$_x$ (blue dotted) transmittance are shown for reference.

XRD spectra of ITO / 80 nm ClAlPc and ITO / 5 nm MoO$_x$ / 80 nm ClAlPc were obtained, with the thicker ClAlPc layer used to increase the signal to noise ratio in the measurement. Previous XRD studies of organic photo-active layers have been reported utilising similar layer thicknesses for this reason.[16, 150] Bailey-Salzmann *et al.* showed ClAlPc to be amorphous using XRD experiments, with the spectra displaying no distinct peaks.[16]
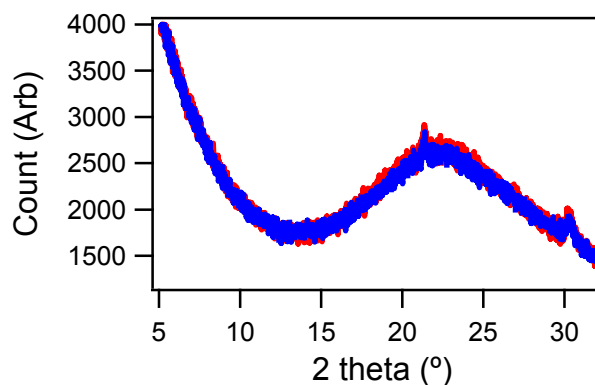
Figure 3.6: Thin film XRD scans for ITO / 80 nm ClAlPc (red line) and ITO / 5 nm MoO$_x$ / 80 nm ClAlPc (blue line).

The XRD spectra presented in Figure 3.6 indicated that the ClAlPc layer was amorphous on both ITO and ITO / 5 nm MoO$_x$. The peaks in the spectra at 30.2 ° and 21.3 ° are due to the underlying ITO in both cases. MoO$_x$ was also shown to be amorphous, with no additional features due to the transition metal oxide layer. This was in agreement with previous reports.[150]

These experiments rule out structural effects such as templating, recently demonstrated using thin organic interlayers including 3,4,9,10-perlenetetracarboxylic dianhydride (PTCDA).[42, 150] These combined experiments are therefore evidence that MoO$_x$ has very little influence on the structural, morphological and absorption properties of the donor layer. Consequently, changes to these properties can be dismissed as the cause of the increased ClAlPc / C$_{60}$ cell performance with the MoO$_x$ layer.

3.1.4 Electronic effects of MoO$_x$ on ClAlPc / C$_{60}$ cells

Shrotriya *et al.* were the first group to use MoO$_x$ as a hole extracting layer in OPV cells,[107] taking inspiration from previous use in OLEDs.[106, 151] In this

pioneering article the performance of a P3HT : PCBM blend was improved when spin-coated onto a MoO$_x$ layer rather than bare ITO. An increase in V_{oc}, J_{sc}, *FF* and η_p was observed with MoO$_x$, giving a marginally greater performance compared to a PEDOT : PSS hole extracting layer (3.33 % compared to 3.18 %). The authors state that they measured the work function of the MoO$_x$ to be 5.3 eV by UPS. It was assumed that the MoO$_x$ layer has a highly p-type character, with the MoO$_x$ valence band residing at 5.3 eV and conduction band at 2.3 eV.[107] Hence, it was deduced that the Fermi level of the MoO$_x$ was pinned to the HOMO of the P3HT, providing a similar cell V_{oc} to those containing a PEDOT : PSS hole extracting layer. The electronic properties of MoO$_x$ are often referenced to this work when reported in the OPV literature,[113, 152, 153] and the values are still regularly quoted in journal articles to date.[17, 154]

With the use of these electronic energy levels, a schematic for understanding how the ClAlPc / C$_{60}$ system operates is shown in Figure 3.7. With improved energy level alignment between the HOMO of ClAlPc (5.4 eV) and the valence band of MoO$_x$ (5.3 eV), efficient hole extraction could be imagined to occur through the MoO$_x$ valence band. The beneficial alignment would allow for a larger V_{bi} compared to the system on bare ITO, which has a work function of ~ 4.6 - 4.8 eV measured here by KP. By maximising the cell V_{bi}, insertion of the MoO$_x$ layer leads to reduced losses in V_{oc}.
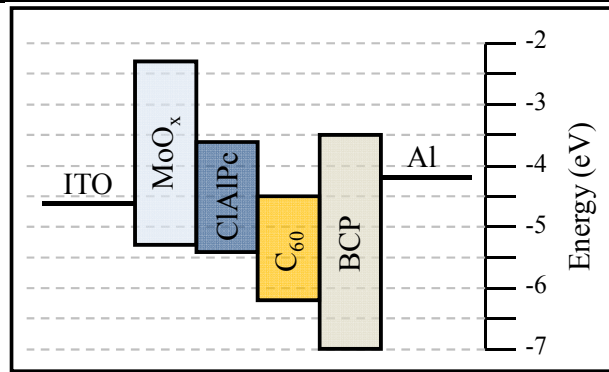
Figure 3.7: Electronic energy level diagram for the ITO / MoO$_x$ / ClAlPc / C$_{60}$ / BCP / Al, with MoO$_x$ values from reference [107].

Irwin *et al.* also reported improvements in P3HT : PCBM cell performance by utilising a p-type NiO hole extracting layer, deposited using PLD.[30] A similar argument to that reported by Shrotriya *et al.* for the MoO$_x$ layer was used to explain the increased cell performance. The wide band gap (3.6 eV) of the NiO layer, combined with an ionisation potential of 5.4 eV, gave reduced losses in V_{bi} and also provided an energetic barrier for electron collection at the anode.[30] Several groups have since also shown the p-type character of the NiO layer through rigorous UPS studies.[155, 156]

Despite this, UPS studies of the MoO$_x$ layer presented here, deposited *in-situ*, conflict with those obtained by Shrotriya *et al.*[107] In order to propose an alternative theory behind the increase of V_{oc} with the insertion of MoO$_x$, the electronic structure for the ClAlPc / C$_{60}$ system on bare ITO must first be understood. Figure 3.8 is reproduced from reference [110], previous work carried out by the Jones group. The UPS studies in the report showed the work function of bare ITO to be 4.4 eV, with a 0.3 eV V_l shift upon deposition of ClAlPc. This gave ClAlPc a work function of 4.7 eV. The onset of the ClAlPc HOMO was measured to be 0.55 eV below the Fermi

level, giving an ionisation potential of 5.25 eV. This was marginally lower than other reported values for ClAlPc (5.3 - 5.4 eV).[16, 112] This work indicates an energy level offset of 0.55 eV between the ITO work function and the HOMO level of ClAlPc.
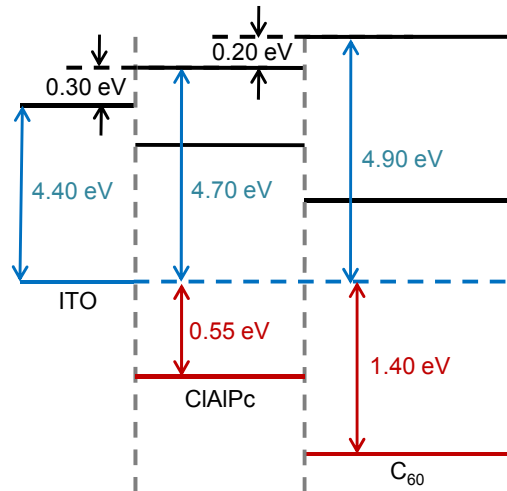
Figure 3.8: Schematic energy level diagram for the ClAlPc / C$_{60}$ system on bare ITO. Reproduced from reference [110].

In order to show the electronic effects the MoO$_x$ layer had on the ClAlPc / C$_{60}$ system, UPS studies were conducted. Figure 3.9 shows the secondary electron cut-off and valence band UPS spectra for the ClAlPc / C$_{60}$ system measured on ITO / 5 nm MoO$_x$. Each layer was deposited *in-situ*, with sequential deposition and UPS measurements. In Figure 3.9(a) ITO was shown to have a work function of 4.5 eV. The spectrum for 5 nm MoO$_x$ showed a clear increase in work function to 6.4 eV. The significant difference in work function between the ITO and MoO$_x$ leads to the formation of a large interface dipole due to electron transfer from ITO to MoO$_x$, resulting in a V_I shift of 1.9 eV. The work function of the MoO$_x$ demonstrated here was 1.1 eV larger than that reported by Shrotriya *et al.*[107]
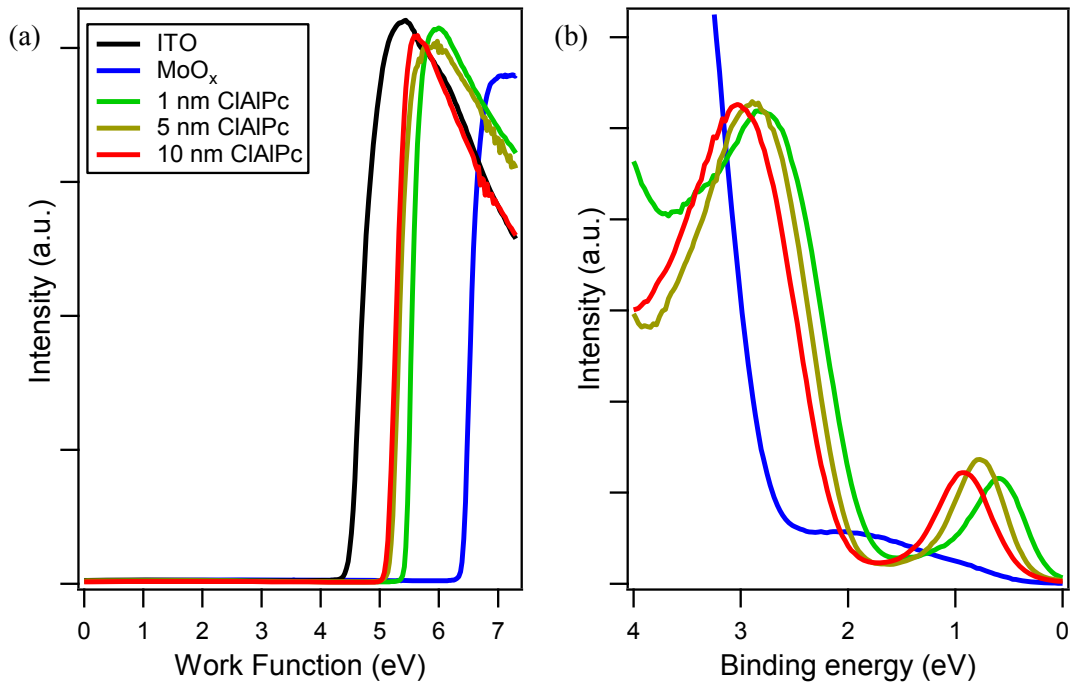
Figure 3.9: (a) Onset of the secondary electron cut-off and (b) valence band UPS spectra for ITO (black line)/ 5 nm MoO$_x$ (blue lines) / 1 nm (green lines), 5 nm (gold lines), 10 nm (red lines) ClAlPc.

Figure 3.9(b) indicates the onset of the MoO$_x$ valence band to be 2.7 eV below the Fermi level, resulting in an ionisation potential energy of 9.1 eV. With the band gap of thermally evaporated MoO$_x$ measured at 3.4 eV here (Figure 3.2 inset), this implies an n-type character for MoO$_x$. Since the band gap has been measured to be 3.4 eV, the position of the conduction band was ~ 0.7 eV above the MoO$_x$ Fermi level. Figure 3.9(b) also indicate the presence of additional states between the Fermi level and valence band of MoO$_x$. These 'gap states' are shown to be between 0.3 to 2.3 eV below the MoO$_x$ Fermi level, within the band gap of the MoO$_x$. Other researchers have also reported these features for a substoichiometric oxygen deficient thermally evaporated layer of MoO$_x$,[157, 158] and for other n-type transition metal oxides.[159]

To demonstrate the impact of the high work function MoO$_x$ layer on the donor material, sequential layer growths of ClAlPc with total thicknesses of 1, 5 and 10 nm were deposited and measured by UPS *in-situ*. Figure 3.9(a) shows the work function of ClAlPc to be reduced from 5.4 to 5.2 and 5.1 eV for 1, 5 and 10 nm layers respectively. A dipole was formed at the interface between MoO$_x$ and ClAlPc, with electron transfer into the MoO$_x$. The V_l shift from MoO$_x$ to the 1 nm ClAlPc layer was 1.0 eV. As the ClAlPc layer thicknesses were increased to 5 and 10 nm, there were further V_l shifts of 0.2 and 0.3 eV respectively compared to the 1 nm layer.

The onset of the ClAlPc HOMO can be seen in Figure 3.9(b). It was established that the HOMO onset of the 1 nm ClAlPc layer resides 0.1 eV below the Fermi level, producing an ionisation potential of 5.5 eV. The HOMO onset of the 5 and 10 nm ClAlPc layers were positioned 0.3 and 0.4 eV below their respective Fermi levels. These thicknesses accordingly exhibited ionisation potentials of 5.5 eV, marginally larger (~0.1 eV) than values commonly reported.[16, 160]

Figure 3.10 presents an overall energy level schematic for this UPS data. This clearly illustrates the n-type character of MoO$_x$, in addition to the considerable V_l shifts due to electron transfer for both materials in contact with MoO$_x$. Band bending (due to the formation of a space charge region) in the ClAlPc layer towards the MoO$_x$ interface was revealed, with the HOMO level of the ClAlPc bending towards the MoO$_x$ Fermi level. This significant Fermi level pinning of the organic was not witnessed with ClAlPc on bare ITO.[110]

Figure 3.10: Schematic energy level diagram from UPS data for ITO / 5 nm MoO$_x$ / 1, 5, 10 nm ClAlPc.

The high work function of MoO$_x$ is the cause of the band bending in ClAlPc, resulting in charge transfer. As discussed in Section 1.5.2, selection rules such as the 'Mark of Zorro' indicate that in order to maximise the V_{oc} of the cell the work function of the hole extracting layer must be equal to or larger than the E_{ICT+} energy of the donor material (or ionisation potential value depending on the reported rule).[54, 57] It is only if this is true that the pinning of the organic occurs with spontaneous charge transfer, maximising V_{bi} and reducing losses in V_{oc}. Accordingly, the high work function of the MoO$_x$ film makes the hole extracting layer an ideal choice for donor materials with a relatively deep E_{ICT+} value, such as ClAlPc. Since the ITO work function is between the positive and negative integer charge transfer states of ClAlPc, this led to losses in the V_{bi} of the cell, resulting in a lower V_{oc} value.

One of the implications of the p-type character of MoO$_x$ reported previously was that hole-extraction occurs through the MoO$_x$ valence band. However, these measurements showing the n-type character of the MoO$_x$ indicate that this is not

possible due to the low lying valence band of the layer. Consequently the hole-extraction must occur via another mechanism. Whilst the benefits of the high work function of the MoO$_x$ layer are widely accepted, the method of hole transport through the layer is less understood. The presence of the additional states shown within the MoO$_x$ band gap in Figure 3.9 is a controversial topic in the current literature. Publications by Meyer *et al.*,[161] Gwinner *et al.* and Sun *et al.* show UPS data without evidence of the gap states, or / and XPS with only a Mo^{6+} contribution.[149, 162] Kroeger *et al.* studied the role of MoO$_3$ within OLEDs using UPS, suggesting hole injection improvements were facilitated by electron extraction from the organic HOMO through the MoO$_3$ conduction band.[163] Further reports by the same group and collaborators have proposed that in OPV cells the extraction of holes occurs through the MoO$_3$ conduction band.[164]

However, there have been a similar number of groups reporting substoichiometric MoO$_x$ using UPS and XPS.[157, 158, 165-167] Wu *et al.* studied the role of MoO$_x$ within OLEDs, with the reduced form of MoO$_x$.[158] They suggested the substoichiometric defects were created by the thermal evaporation process and allowed for reduced barrier heights for charge extraction. Kanai *et al.* also reported gap states within MoO$_x$ films 5 to 20 nm thick.[157] They commented that the gap states allow hole extraction from Au to the organic. Irfan *et al.* observed the additional states using UPS in a study of ITO / MoO$_x$ / ClAlPc.[160] This resulted in the suggestion that one possible mechanism of hole extraction could be through these partially filled states. A similar explanation has been proposed by other researchers.[166]

Some groups have actively increased the density of the gap states by sputtering the surface of the MoO$_x$.[168, 169] Chiam *et al.* thermally evaporated and

solution processed MoO$_x$ layers.[168] They directly compared an as prepared solution processed sample to a sputtered sample that showed considerable additional Mo^{5+} states. OPV performance was greatly improved for the cell containing the defects. The authors state that this was likely to be due to the larger number of pathways for charge extraction after the sputtering process. Wang *et al.* report a similar improvement in performance for OLED devices with the sputter treatment on thermally evaporated MoO$_x$.[169]

Vasilopoulou *et al.* have had a series of reports comparing stoichiometric and substoichiometric WO$_x$ and MoO$_x$.[159, 170, 171] They described significantly improved hole injection for hole only devices when using a 65 % Mo^{6+}, 35 % Mo^{5+} layer in comparison to stoichiometric MoO$_3$. This was believed to be due to charge transport through the additional states.[171]

Therefore, there is no complete consensus within the current literature for the mechanism of hole extraction through a MoO$_x$ layer. However, the defect states reported here (Figure 3.9) due to substoichiometric MoO$_x$, may either facilitate hole transfer directly from the donor to the ITO or alternatively provide additional electrons that can be excited to allow hole transfer to the MoO$_x$ conduction band.

The conduction band of MoO$_x$ was located between the HOMO and LUMO of most donor materials as a consequence of the n-type character of the layer. In the case of bulk heterojunctions, the acceptor materials are also in contact with the metal oxide and there is no barrier to electron extraction from the active layer. This is in contrast to the p-type, electron blocking behaviour reported by Shrotriya *et al.*[107] Indeed, Subbiah *et al.* reported an increase in performance of polymer bulk heterojunction cells containing the MoO$_x$ layer and an additional electron blocking

layer compared to MoO$_x$ alone.[172] This indicates another contrast to the mechanism of hole extraction for a p-type NiO layer, which occurs through the NiO valence band and allows electron blocking characteristics.[30]

3.1.5 Exposure of the MoO$_x$ layer to air

In order to determine the effect of air exposure on MoO$_x$ films, layers were deposited onto ITO and exposed to air for between 0 and 3 days. ClAlPc / C$_{60}$ cells were then fabricated on these layers, with the *J-V* measurements shown in Figure 3.11.
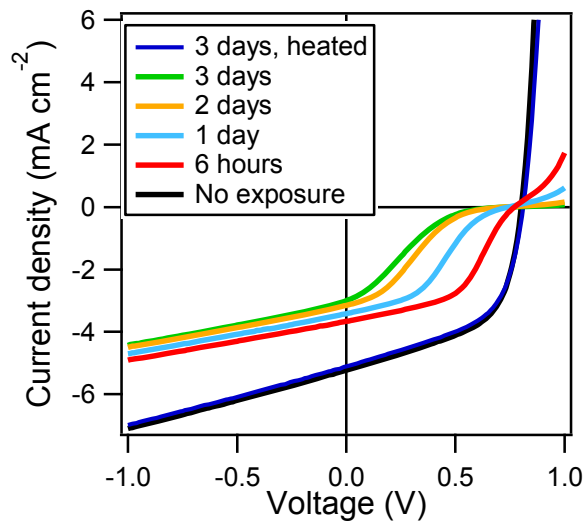
Figure 3.11: *J-V* curves obtained under 1 sun illumination for cells with structure ITO / 5 nm MoO$_x$ / 20 nm ClAlPc / 40 nm C$_{60}$ / 8 nm BCP / Al, with MoO$_x$ exposed to air for between 0 to 3 days.

The exposure of MoO$_x$ to air had a significant detrimental impact on cell performance, increasing R_s while decreasing J_{sc} and *FF* with increased exposure. The reduction of V_{oc} for the cells was less considerable, with reductions from 0.80 V to 0.74 V for non-exposed layers to 3 days of air exposure respectively. The largest loss in performance was in *FF*, decreased from 0.54 to 0.18 due to the increased R_s.

As the layers are exposed to atmospheric conditions for a longer period of time charge transport appears to be hindered, leading to the increased R_s and decreases in J_{sc} and *FF*. Figure 3.12 shows the variation of key parameters with exposure time.

Some of the MoO$_x$ layers that were exposed to air for 3 days were subsequently heat treated, at 150 °C for 20 minutes under a N$_2$ atmosphere. After photo-active layer deposition, the performance of cells containing the heat treated layer were nearly identical to that of a cell containing a non-exposed MoO$_x$ film. This indicated a reversible effect of air exposure for the MoO$_x$ layer.
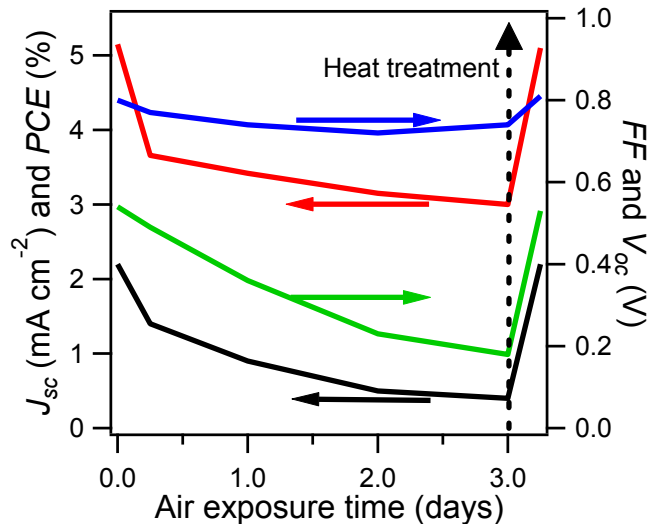
Figure 3.12: Key cell parameters η_p (black line), J_{sc} (red line), V_{oc} (blue line) and *FF* (green line) against air exposure time for ITO / 5 nm MoO$_x$ / 20 nm ClAlPc / 40 nm C$_{60}$ / 8 nm BCP / Al cells.

The work function of the MoO$_x$ layers was measured by KP in a N$_2$ environment. The non-exposed MoO$_x$ layer gave a work function of 6.2 eV, close to the *in-situ* measurement of 6.4 eV obtained by UPS. Layers exposed to air for ~ 10 minutes and 3 days gave work function values of 5.3 eV. After heat treatment at 150 °C for 20 minutes under a N$_2$ atmosphere, the work function of the layer was

measured to be 6.2 eV. Hence, the work function measurement of MoO$_x$ obtained by Shrotriya *et al.* was most likely measured after air exposure of the films.[107] This set of data highlights the importance of *in-situ* measurements of the electronic characteristics of thin films in order to understand the attributes of OPV cells.

Upon air exposure, adsorption of water and other materials leads to a reduced work function for the layers. This was due to charge transfer to the adsorbed species and the surface sensitivity of the KP technique.[173] With heat treatment the majority of these adsorbed species are removed, restoring the work function of the MoO$_x$ to its original value. The likely reason for the stable cell V_{oc} with variation of exposure time after the initial drop to ~0.74 V, was that the work function of the MoO$_x$ layer remained consistently high at a value of 5.3 eV. This was close to or higher than the expected E_{ICT+} of ClAlPc (compared to bare ITO, a V_{oc} 0.51 V and a work function of ~ 4.6 to 4.8 eV).[107] Similar changes to MoO$_x$ work function with air exposure have been reported,[161, 173] with a reversible degradation after air exposure of F8BT / MoO$_3$ diodes demonstrated by Gwinner *et al.*[149]

These experiments indicate the MoO$_x$ hole extracting layer may not be suitable for use with high ionisation potential water soluble donor materials. However, the effects of exposure to air were reversible by a simple heat treatment before active layer deposition, which may be a applicable step in commercial techniques such as roll-to-roll processing.

3.2 Use of the MoO$_x$ hole extracting layer in other OPV systems

3.2.1 The direct influence of MoO$_x$ on the SubPc / C$_{60}$ system

The effect of the MoO$_x$ hole extracting layer on donor / C$_{60}$ systems with different properties was explored. Cells were fabricated on bare ITO as a comparison to the 5 nm MoO$_x$ layer, optimised for the ClAlPc / C$_{60}$ system presented in Section 3.1.1.

SubPc was chosen as a donor material as it has been shown to have a high ionisation potential of 5.6 eV.[109] This produces a large energy level offset with the C$_{60}$ acceptor, allowing high V_{oc} values to be reached. Cells with the optimised architecture ITO / (0, 5) nm MoO$_x$ / 14 nm SubPc / 40 nm C$_{60}$ / 8 nm BCP / Al were fabricated and tested under 1 sun illumination. Figure 3.13 shows *J-V* curves obtained for the cells and Table 3.2 shows the key cell parameters.
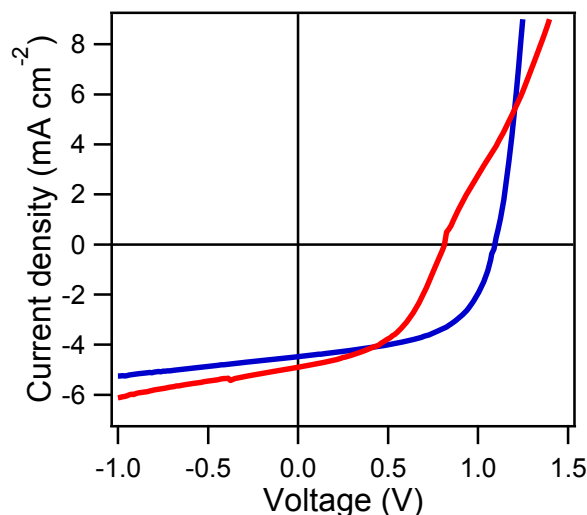
Figure 3.13: *J-V* curves obtained under 1 sun illumination for cells with structure ITO / (0,5) nm MoO$_x$ / 14 nm SubPc / 40 nm C$_{60}$ / 8 nm BCP / Al (0 nm is red line, 5 nm blue line)

When deposited onto bare ITO, the SubPc / C$_{60}$ cells obtained a V_{oc} of 0.79 V, a J_{sc} of 4.97 mA cm^{-2}, a *FF* of 0.47 and therefore η_p was 1.85 %. This was similar to values reported elsewhere.[109, 174] With the insertion of a 5 nm MoO$_x$ layer η_p increased to 2.53 %. This was due to a large gain in V_{oc} to 1.08 V and an increase in *FF* to 0.52, although J_{sc} was reduced to 4.51 mA cm^{-2}. This V_{oc} was far greater than the values previously reported for SubPc / C$_{60}$ on bare ITO, which ranged between 0.57 and 0.97 V.[109, 110, 174] The *J-V* curves also showed a significant reduction in R_s with the insertion of MoO$_x$. A kink in the bare ITO *J-V* curve can be seen in Figure 3.13, and is not present with the MoO$_x$ layer inserted. The elimination of the kink was indicative of the reduced hole extraction losses approaching V_{oc} with the transition metal oxide utilised.

Table 3.2: Summary of cell performance parameters obtained for OPV cells with the architecture ITO / (0,5) nm MoO$_x$ / donor / 40 nm C$_{60}$ / 8 nm BCP / Al.

Donor material, (t nm MoO$_x$)	J_{sc} (mA cm^{-2})	V_{oc} (V)	*FF*	η_p (%)
SubPc, (0)	4.97 ± 0.27	0.79 ± 0.06	0.47 ± 0.05	1.85 ± 0.22
SubPc, (5)	4.51 ± 0.43	1.08 ± 0.01	0.52 ± 0.03	2.53 ± 0.25
CuPc, (0)	4.47 ± 0.40	0.47 ± 0.02	0.53 ± 0.02	1.11 ±
CuPc, (5)	4.37 ± 0.26	0.46 ± 0.01	0.51 ± 0.05	1.03 ±
Pentacene, (0)	6.43 ± 0.66	0.42 ± 0.02	0.51 ± 0.02	1.38 ±
Pentacene, (5)	6.06 ± 0.60	0.43 ± 0.03	0.48 ± 0.03	1.24 ±

The reduction of J_{sc} by 0.46 mA cm^{-2} for the SubPc / C$_{60}$ cells incorporating a MoO$_x$ layer can be understood from the SubPc UV-vis absorption spectra presented in Figure 3.14. The ClAlPc / C$_{60}$ cells had a decrease in J_{sc} of 0.22 mA cm$^-$

^{2}, due to the loss of transmittance in the C$_{60}$ region of the spectra caused by the MoO$_x$ layer. However, the main ClAlPc absorption peak was between 600 - 850 nm, with a maximum at 740 nm and therefore was largely unaffected by MoO$_x$ transmittance losses. SubPc has a main absorption region between 475 - 625 nm. The SubPc absorption maximum is positioned at 590 nm, with a shoulder at 540 nm, due to aggregates and monomer SubPc species respectively. With MoO$_x$ absorption losses centred at 492 nm, and covering a broad range between 400 - 600 nm, the SubPc cells will have a more significant reduction in photogenerated current in the donor region. This was in addition to the J_{sc} loss for the C$_{60}$ region in both systems. Figure 3.14 does indicate that although there was increased absorption due to the MoO$_x$, the SubPc absorption peaks are not red or blue shifted, so no significant change in packing of the donor is exhibited.
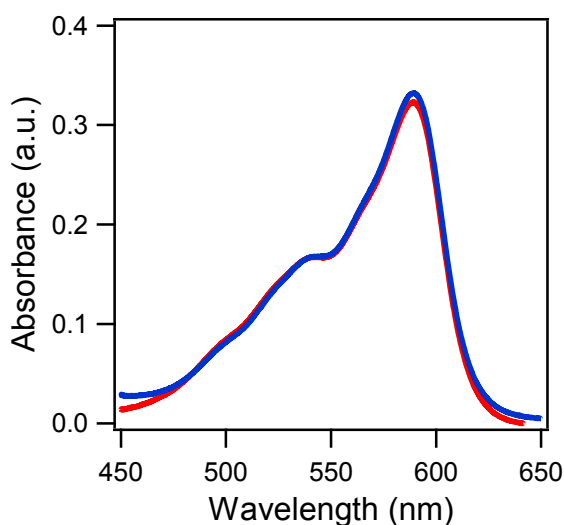
Figure 3.14: UV/vis absorption data for ITO / 14 nm SubPc (red line) and ITO / 5 nm MoO$_x$ / 14 nm SubPc (blue line) against an ITO background scan.

The topographical AFM images of a 14 nm SubPc layer deposited onto bare ITO and ITO / 5 nm MoO$_x$ are displayed in Figure 3.15. These produced similar R_q

values of 2.3 and 2.4 nm respectively. The SubPc films on both surfaces were smoother than the ITO and MoO$_x$ surfaces measured in Section 3.1.2. The similarities between the SubPc topographies, which roughly follow that of the underlying ITO, also suggests the MoO$_x$ does not have an influence on layer morphology or crystallinity, just as with the AFM images previously demonstrated for ClAlPc.
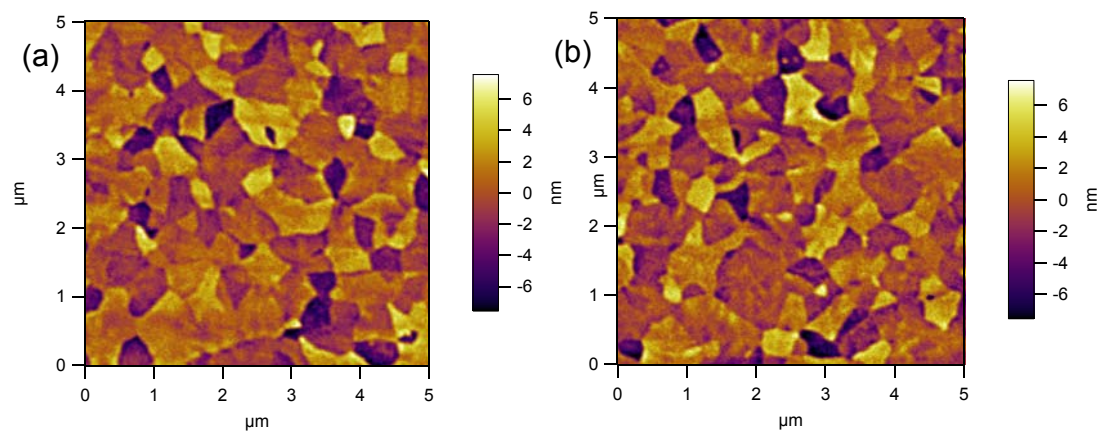
Figure 3.15: 5 μm AFM topographical images of ITO / 14 nm SubPc (a) and ITO / 5 nm MoO$_x$ / 14 nm SubPc (b). All images have the same height scale (± 6 nm).

3.2.2 The impact of the MoO$_x$ layer on CuPc / C$_{60}$ cells

Having presented the impact of MoO$_x$ on two high ionisation potential systems, ClAlPc and SubPc, the effect of the layer on lower ionisation potential donor materials was tested. CuPc is a widely used donor material, with a relatively low ionisation potential, reported between 4.95 - 5.20 eV.[109, 110] Literature values for CuPc / C$_{60}$ cell performance on ITO varies between < 1 % and 4 %, however the majority of reports are between 0.7 - 2.0 %.[25, 109, 118]

Cells with the architecture ITO / (0, 5) nm MoO$_x$ / 30 nm CuPc / 40 nm C$_{60}$ / 8 nm BCP / Al were fabricated and tested under 1 sun illumination. Figure 3.16

shows *J-V* curves obtained for the cells and Table 3.2 shows the key cell parameters. On bare ITO the CuPc / C_{60} system produced a J_{sc} of 4.47 mA cm^{-2}, a V_{oc} of 0.47 V, a *FF* of 0.53 and accordingly an η_p of 1.11 %. When CuPc is employed as the donor material a lower V_{oc} is observed compared to ClAlPc and SubPc with a C_{60} acceptor, due to the lower ionisation potential of the material, producing a smaller interface gap with C_{60}. When utilising a MoO_x hole extracting layer with the CuPc / C_{60} system, the V_{oc}, *FF* and J_{sc} were marginally reduced producing a η_p of 1.03 %. Therefore, unlike the higher ionisation potential materials, there was no gain in V_{oc} when using MoO_x.
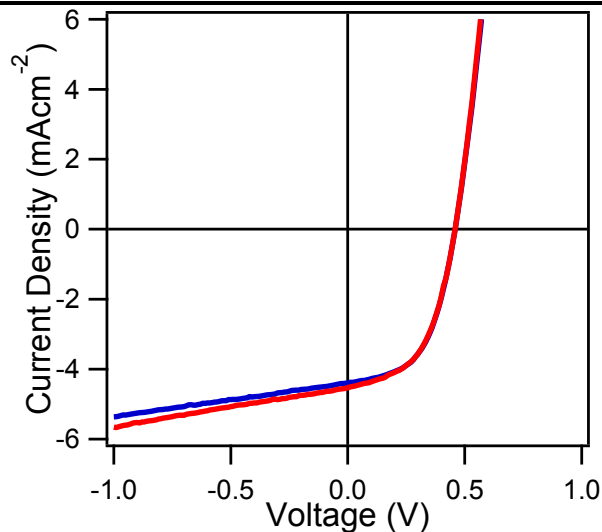
Figure 3.16: *J-V* curves obtained under 1 sun illumination for cells with structure ITO / (0,5) nm MoO_x / 30 nm CuPc / 40 nm C_{60} / 8 nm BCP / Al (0 nm is red line, 5 nm blue line).

3.2.3 The impact of the MoO_x layer on pentacene / C_{60} cells

Another commonly used donor material is pentacene, with a low ionisation potential with reported values of between 4.8 - 5.2 eV.[120, 121] Pentacene is used extensively in organic electronics due to a relatively long exciton diffusion length of > 50 nm, allowing comparatively thicker layers to be used and favourably increasing

light absorption.[81, 175] Cells with the previously optimised architecture ITO / (0, 5) nm MoO$_x$ / 43 nm pentacene / 40 nm C$_{60}$ / 8 nm BCP / Al were fabricated and tested under 1 sun illumination.[81] Figure 3.17 shows the cells *J-V* curves and Table 3.2 shows the key cell parameters.

On bare ITO the pentacene / C$_{60}$ system produced a *J$_{sc}$* of 6.43 mA cm^{-2}, a *V$_{oc}$* of 0.42 V, a *FF* of 0.51 and thus a η_p of 1.38 %. The *J$_{sc}$* achieved by the pentacene / C$_{60}$ cells was significantly higher than that of the other donor / C$_{60}$ systems, due to the enhanced absorption profile of the thick pentacene layers and the likelihood of triplet fission.[176] Yet, the low cell *V$_{oc}$* obtained led to an unfavourable overall performance compared to the high ionisation potential materials. This highlights one of the material choice compromises encountered with planar heterojunction cells, with a degree of trade off between improved current generation and energy level offsets for high *V$_{oc}$* values.
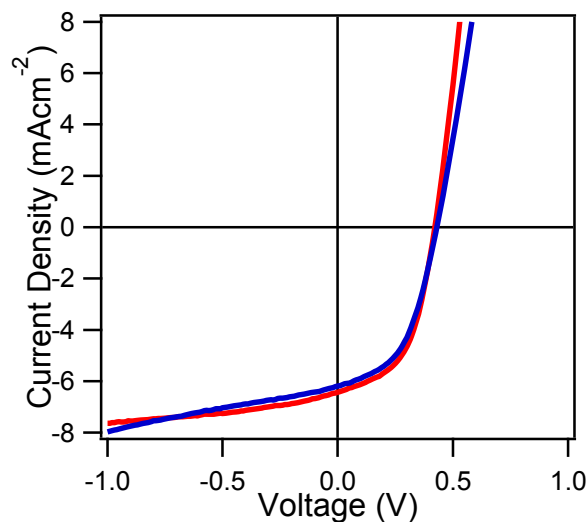
Figure 3.17: *J-V* curves obtained under 1 sun illumination for cells with structure ITO / (0,5) nm MoO$_x$ / 43 nm pentacene / 40 nm C$_{60}$ / 8 nm BCP / Al (0 nm is red line, 5 nm blue line).

When a 5 nm MoO$_x$ layer was inserted into the pentacene / C$_{60}$ system a similar V_{oc} of 0.42 V was attained. Slight losses in *FF* to 0.48, and J_{sc} resulted in a reduction of η_p to 1.24 %, compared to 1.38 % on bare ITO. The result was similar to the CuPc / C$_{60}$ system, with losses in J_{sc} and no gain in V_{oc}, resulting in a marginal loss of η_p.

3.2.4 The factors determining OPV cell performance with MoO$_x$ layer insertion

The UV-vis absorption spectra for CuPc and Pentacene, presented in Figures 3.18(a) and 3.18(b) respectively, account for the losses in J_{sc} for each donor systems cells. The marginal reduction (0.10 mA cm^{-2}) for CuPc / C$_{60}$ cells containing MoO$_x$ is mainly due to the reduced transmittance in the C$_{60}$ absorption region for the layer. The broad absorption of CuPc between 550 - 800 nm does not significantly overlap with the MoO$_x$ absorption between 400 - 600 nm, which leads to smaller J_{sc} losses for CuPc cells compared to SubPc. The 0.37 mA cm^{-2} reduction in J_{sc} for pentacene / C$_{60}$ can also be attributed to an overlap with the MoO$_x$ absorption between 400 - 600 nm. The main region for the pentacene current generation was between 500 - 750 nm. Pentacene produced two main maxima, with the largest centred at 670 nm, with a corresponding shoulder at 630 nm, and another maxima at 583 nm. Accordingly, increased overlap with the absorption region of the MoO$_x$ layer resulted in more noticeable reductions in current generation for pentacene cells compared to those with CuPc.
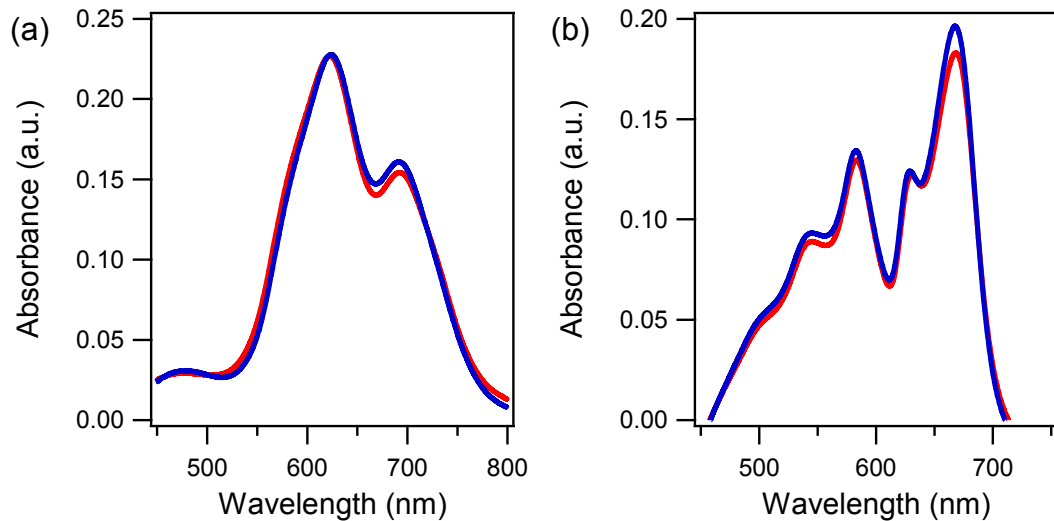
Figure 3.18: UV/vis absorption data for (a) ITO / 30 nm CuPc (red line) and ITO / 5 nm MoO$_x$ / 30 nm CuPc (blue line), and (b) ITO / 43 nm pentacene (red line) and ITO / 5 nm MoO$_x$ / 43 nm pentacene (blue line), each against an ITO background scan.

Just as demonstrated for the higher ionisation potential materials, the morphology and packing of CuPc and pentacene are largely unaffected by deposition onto a 5 nm layer of MoO$_x$. The AFM topographical images of 30 nm layers of CuPc in Figure 3.19(a) and (b) show near identical crystalline structures and gave R_q values of 4.9 nm for growth on both bare ITO and ITO / 5 nm MoO$_x$. The XRD data in Figure 3.19(c) for 80 nm thick CuPc layers on bare ITO and ITO / 5 nm MoO$_x$ indicated no shift in the main CuPc peak at $2\theta = 6.8°$, corresponding to an interplanar spacing distance of 1.30 nm. In combination with the negligible shifts in the absorption spectra above, it can be concluded that no significant change in growth of the CuPc occurs when grown on a MoO$_x$ layer.[177]
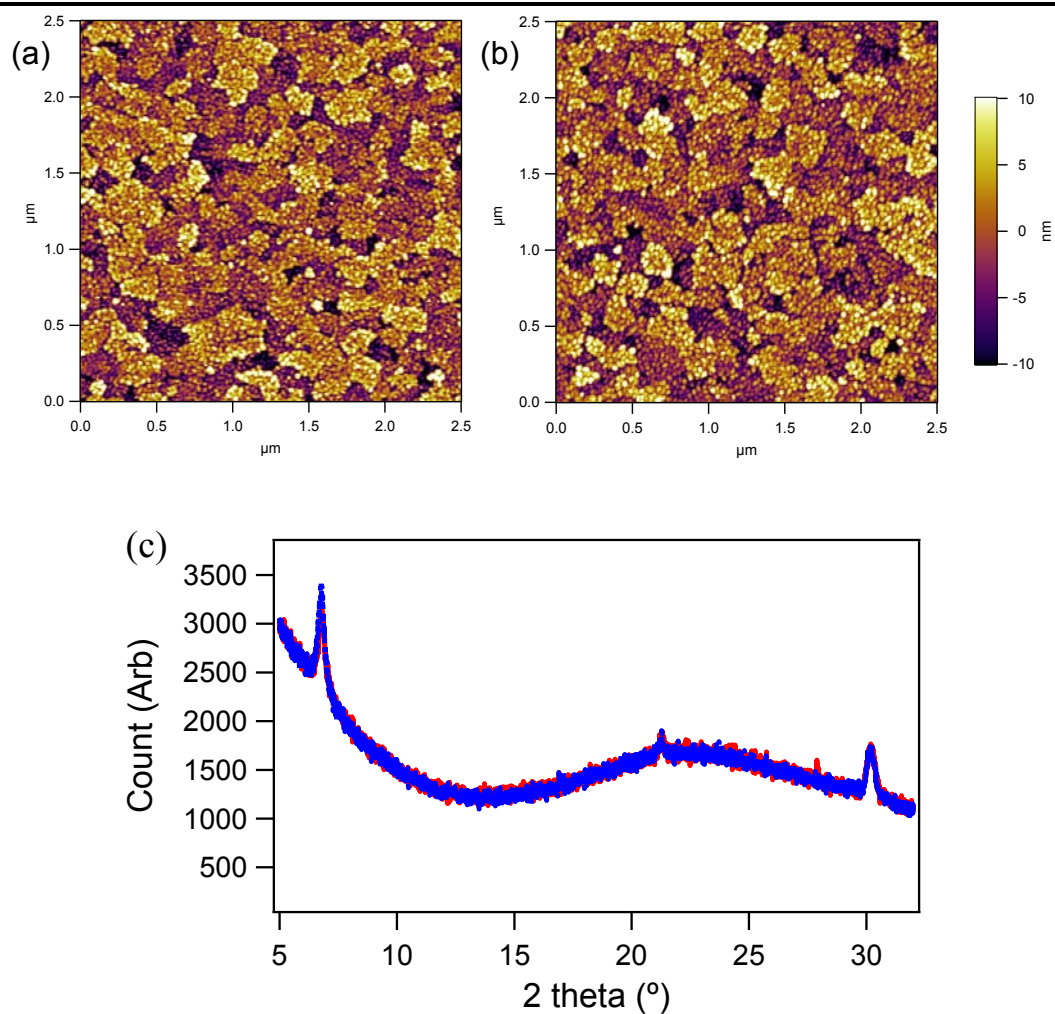
Figure 3.19: 2.5 μm AFM topographical images of ITO / 30 nm CuPc (a) and ITO / 5 nm MoO$_x$ / 30 nm CuPc (b). All images have the same height scale (± 10 nm). (c) Thin film XRD scans for ITO / 80 nm CuPc (red line) and ITO / 5 nm MoO$_x$ / 80 nm CuPc (blue line).

The differing effects of inserting a MoO$_x$ layer between ITO and the photo-active materials can be understood from the electronic properties of each donor material and using the ICT model. With a high work function value, the MoO$_x$ layer was able to exceed the E_{ICT+} of each donor material used. Hence, spontaneous electron transfer from the donor to the metal oxide occurs, pinning the organic HOMO to the MoO$_x$ work function in each system. The SubPc and ClAlPc donors have high ionisation potentials, 5.6 and 5.4 eV respectively, which indicated that the

E_{ICT+} of each donor would exceed the work function of the bare ITO surface. This led to a non ideal contact formed with the ITO, compromising the cell V_{bi}. Thus, a lower V_{oc} was obtained for SubPc / C$_{60}$ and ClAlPc / C$_{60}$ cells on bare ITO compared to deposition on MoO$_x$. The compromised V_{bi} is particularly noticeable with the absence of the kink in the *J-V* curves in Figure 3.13 for MoO$_x$ cells, which was present with bare ITO. The kink indicates a reduced driving force to remove holes produced from photogenerated charges in the near V_{oc} region of forward bias on ITO. With MoO$_x$ the kink was eliminated due to the increased V_{bi}.

The work function value of the MoO$_x$ layer obviously exceeded the E_{ICT+} value of CuPc and pentacene. However, the obtained V_{oc} for these donors with a C$_{60}$ acceptor was similar on both ITO and MoO$_x$. The work function of ITO was measured by KP to be between 4.6 and 4.8 eV. CuPc and pentacene have reported ionisation potential values of 4.95 - 5.20 eV and 4.80 - 5.20 eV respectively.[109, 110, 120, 121] The E_{ICT+} value would be lower than the ionisation potential for each donor. Therefore, it was possible that the ITO work function exceeded the E_{ICT+} of the CuPc and pentacene donors. The similar V_{oc} of CuPc / C$_{60}$ and pentacene / C$_{60}$ cells on both ITO and MoO$_x$ can be rationalised by the idea that for these systems, the cell V_{bi} is maximised on both surfaces. This resulted in similar V_{oc} values. These results suggest that there was no advantage to incorporating a MoO$_x$ hole extracting layer for low ionisation potential materials.

3.2.5 The influence of the MoO$_x$ layer on cell stability

In order to be a commercially viable energy source, OPVs need to be both efficient and retain performance over time. Bare ITO is known to be an unstable electrode due to oxygen diffusion from its surface into the active layer.[78-80] PEDOT : PSS has been commonly used by many researchers as a hole extracting layer in order

to enhance initial cell performance. However, this still has the undesirable characteristics of delaminating from the electrode surface and a damaging acidity leading to cell degradation.[30, 178, 179] Hence to assess the practicality of MoO$_x$ as a hole extraction layer, stability measurements were performed.

Literature reports have described an initial 'burn in' period for an OPV cell, where the largest losses of cell performance are likely to occur.[180, 181] Whilst only partially accounting for this burn in period, the most significant proportional loss of cell stability often occurs in the first hour of cell illumination. Therefore, each donor / C$_{60}$ system used in the previous sections was tested over 1 hour of constant illumination at 100 mW cm^{-2} AM1.5G under a N$_2$ atmosphere, in order to monitor the relative stability of each interface. *J-V* scans were acquired at 1 minute intervals for devices fabricated on both ITO and MoO$_x$. Normalised key cell parameters are displayed in Figure 3.20. A cell with an architecture that displays a significant proportional loss of original performance during the initial illumination study is clearly of little use for commercial products.

Figure 3.20 reveals that the stability of the cells under one hour of constant illumination was significantly increased with the MoO$_x$ layer. There were reduced losses in J_{sc} with MoO$_x$, except for the ITO / pentacene cell. There was an average 9 % J_{sc} reduction across the 4 systems with MoO$_x$ compared to a 14 % loss on bare ITO. A much greater stability was achieved for cell V_{oc} and *FF*, with only a 3 and 1 % average loss for these parameters over the 4 systems on MoO$_x$. On bare ITO, losses of 30 % and 19 % were encountered for V_{oc} and *FF* respectively. This led to an overall average degradation of 52 % on bare ITO and only 13 % with insertion of MoO$_x$. Due to the severity of the degradation for the pentacene and CuPc systems on bare ITO, and the relative stability of the same systems on MoO$_x$, it appeared that it

would be advantageous to fabricate these cells on the metal oxide hole extracting layer for the improved stability despite an initial lower performance.
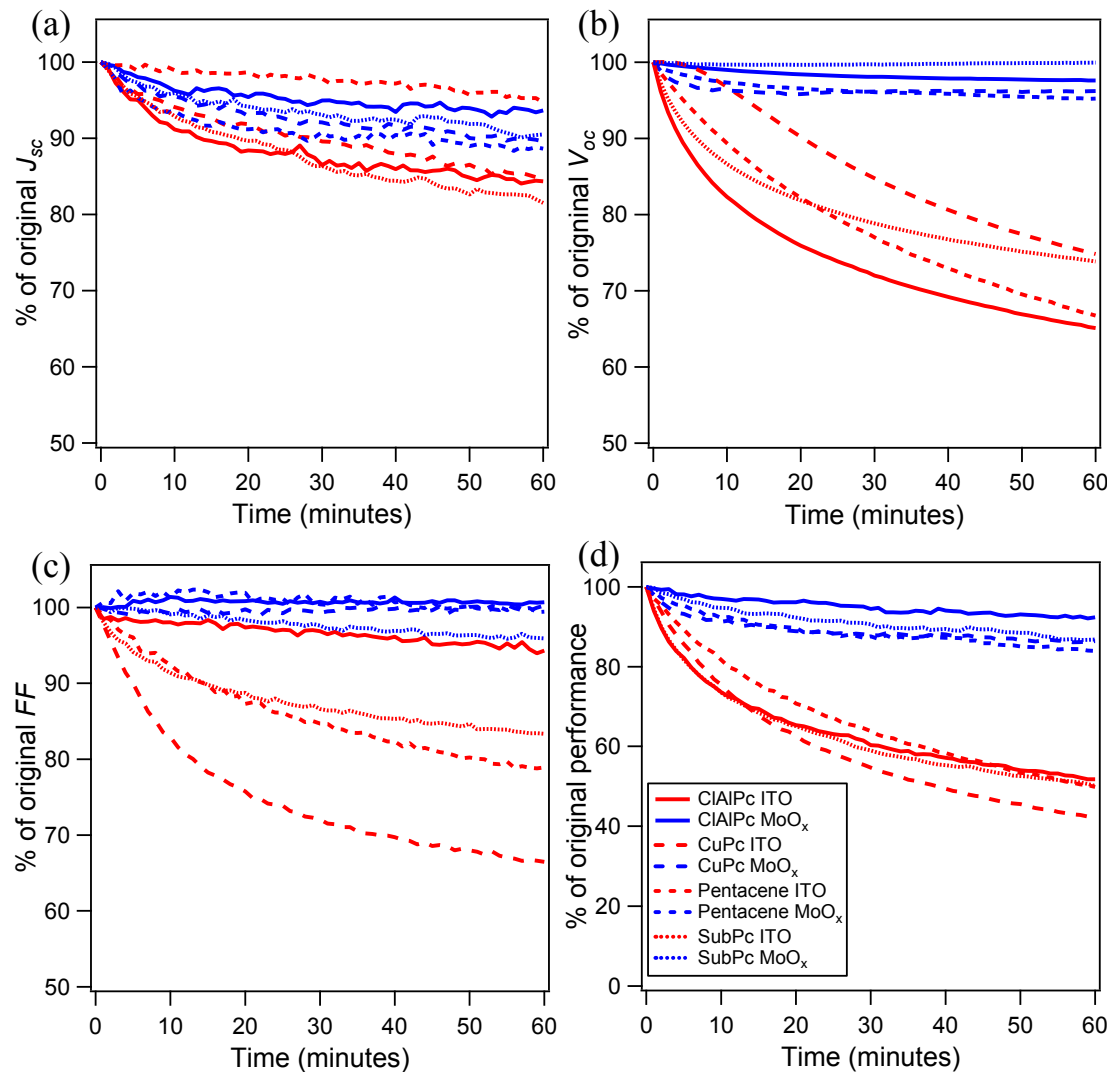
Figure 3.20: (a) J_{sc}, (b) V_{oc}, (c) FF and (d) η_p measured under constant 1 sun illumination for 60 minutes under an N$_2$ atmosphere, with key in (d), expressed as a percentage of the original performance value.

The J_{sc} of the SubPc cell was reduced by ~19 % on bare ITO and ~10 % on the metal oxide hole extracting layer after 60 minutes illumination. *EQE*

measurements were performed before and after device degradation under constant illumination and are shown in Figure 3.21.
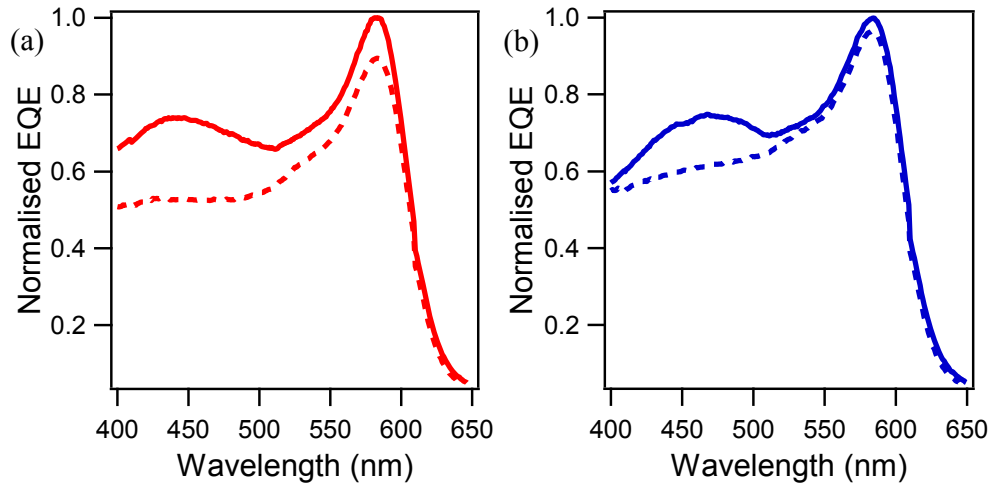
Figure 3.21: *EQE* data taken before (solid lines) and after (dashed lines) degradation for 1 hour under constant illumination under an N$_2$ atmosphere for (a) ITO / 14 nm SubPc / 40 nm C$_{60}$ / 8 nm BCP / Al and (b) ITO / 5 nm MoO$_x$ / 14 nm SubPc / 40 nm C$_{60}$ / 8 nm BCP / Al.

On MoO$_x$ the overall degradation was lower across the whole spectrum when compared to bare ITO. The region of current generation between 400 - 525 nm can be attributed to the C$_{60}$ acceptor.[175] This region shows a substantial loss in the *EQE* spectra after degradation on both ITO and MoO$_x$. Since C$_{60}$ is known to photo-oxidise the degradation should be expected in both cell architectures. However, the *EQE* spectra also reveal an additional overall loss of current generation for the cell deposited on ITO compared to the MoO$_x$ hole extracting layer. This indicates the increased stability of the MoO$_x$ interface compared to that of ITO. It is likely that the MoO$_x$ layer prevents unwanted chemical reactions between the ITO surface and the photo-active layers, such as the diffusion of oxygen from ITO into the active

regions.[78-80] The increased degradation due to the ITO surface causes disruption to the charge transport paths, leading to a reduction of J_{sc} V_{oc} and FF compared to cell fabrication on MoO$_x$. As the photo-active layer degrades on ITO, charge accumulation compromises the built-in electric field of the cell. The MoO$_x$ was therefore able to act as a physical barrier to the reactions and also had the advantage of being oxygen deficient. The metal oxide was consequently an ideal hole extracting layer to minimise these oxidation reactions.

Interestingly, Zhou *et al.* reported a decrease in ITO work function from 4.7 eV to 4.2 eV using a solar simulator or UV lamp.[182] This led to a large loss of cell performance when measured over 45 minutes of illumination for a CuPc / C$_{60}$ system, from 1.36 % to 0.47 %. Similar losses in FF, J_{sc} and V_{oc} as those reported here were demonstrated. The decrease in work function was found to favour using ITO as a electron extracting contact when the inverted cells were tested over 11 minutes illumination, removing a large kink in the first J-V curve. Surface modifiers were therefore used to reduce the variability of work function for the hole and electron extracting interfaces in standard and inverted structures.[182]

Further stability tests were carried out for SubPc / C$_{60}$ cells with 24 hours constant illumination at 1 sun. This test used the degradation system described in Section 2.2.1, and the measurement is shown in Figure 3.22. After 1 hour the cells on bare ITO and MoO$_x$ show similar stability characteristics to those presented in Figure 3.20, retaining 46 and 94 % of the original cell η_p respectively. After 24 hours constant illumination, the bare ITO cell had suffered extensive degradation and maintained only 6 % of the original cell η_p. In contrast, the cell grown on MoO$_x$

retained 62 % of the original cell η_p. It can be seen that after the first 250 minutes

illumination, the SubPc / C$_{60}$ cells on MoO$_x$ degrade fairly linearly.
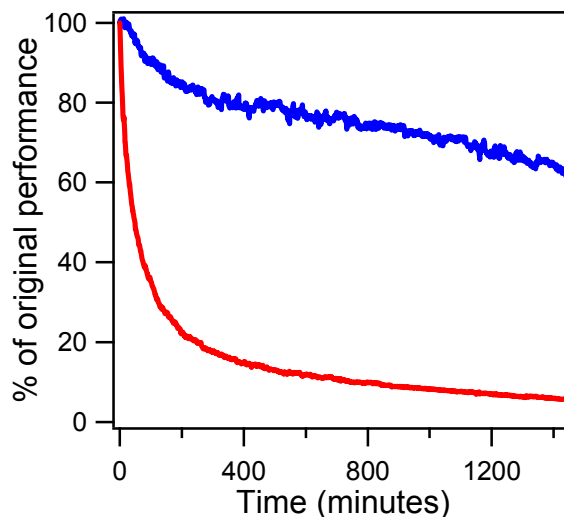
Figure 3.22: Stability measured under constant 1 sun illumination under an N$_2$ atmosphere

for 1440 minutes (24 hours) for ITO / 14 nm SubPc / 40 nm C$_{60}$/ 8 nm BCP / Al (red line)

and ITO / 5 nm MoO$_x$/ 14 nm SubPc / 40 nm C$_{60}$/ 8 nm BCP / Al (blue line).

In addition to the cell stability tests with constant illumination, the shelf life

stability of SubPc / C$_{60}$ cells on bare ITO and MoO$_x$ were tested over a longer period

of time. In this study, the cell performances were tested under one sun illumination

once a day and then stored in dark conditions in a nitrogen filled glovebox. Figure

3.23 shows the outcome of the testing period.

Figure 3.23 indicates that on both bare ITO and MoO$_x$, the greatest reduction

in η_p occurred in the initial period of testing. Both systems incur a less dramatic loss

after this initial period. The initial 'burn in' period is often discounted in literature

reports, with the cell shelf life measured after this effect has occurred.[180] For

example, the initial 400 hours of measurements were discounted as the burn in time

in reference [180] before the relatively linear degradation of the cells. Shelf life and long term measurements are quoted in terms of the T80 and T50 value of a cell. These values represent the time taken for the cell to degrade to 80 and 50 % of the η_p recorded at the end of the burn in period.[180, 181] In this test, the burn in period was also taken to be the closest measurement recoded to 400 hours (16.7 days). The performance retained for SubPc / C$_{60}$ cells on ITO from the end of burn in to the last recorded test (after 52.9 days) was 79 %. This gave a T80 of ~ 33.8 days for the cell. In the time period of 37.1 days after burn in, SubPc / C$_{60}$ cells on MoO$_x$ retained 93 % of the cell η_p. A linear fit of the cell degradation from the end of the burn in period gave a T80 value of ~ 106.0 days with MoO$_x$. This was significantly longer than that achieved by the ITO reference cells.
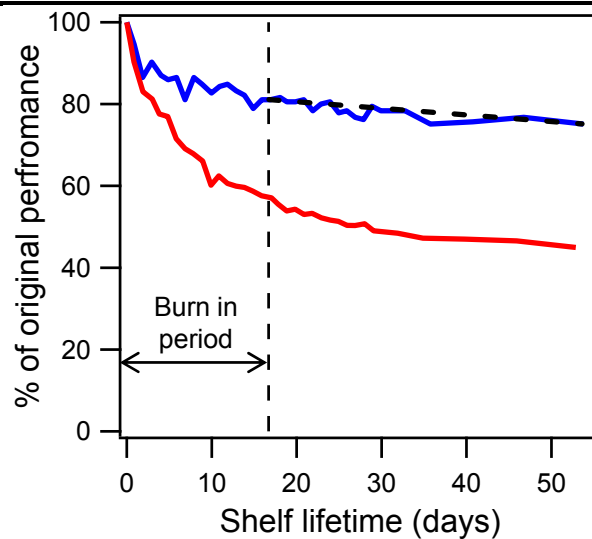
Figure 3.23: Shelf life measurement tests over ~ 54 days under an N$_2$ atmosphere for ITO / 14 nm SubPc / 40 nm C$_{60}$ / 8 nm BCP / Al (red line) and ITO / 5 nm MoO$_x$ / 14 nm SubPc / 40 nm C$_{60}$ / 8 nm BCP / Al (blue line), with a linear fit to determine the T80 of the MoO$_x$ cell (dotted black line).

These tests indicate that MoO$_x$ considerably increases the stability of the donor / C$_{60}$ cells under both storage and illumination conditions. Whilst the cells still do not currently provide the stability that would be required for commercialisation, further possible improvements have already been implemented. Sullivan *et al.* replaced C$_{60}$ with Cl$_6$-SubPc as the acceptor for a 24 hour constant illumination measurement.[21] The cell containing C$_{60}$ was reduced to 64 % of the original η_p, whereas with the cell using the Cl$_6$-SubPc acceptor retained 85 % η_p. Other researchers have replaced the exciton blocking layer, BCP, with metal oxides such as ZnO and TiO$_2$.[68, 183, 184] Indeed, Schumann *et al.* reported increased stability for an inverted polymer blend of P3HT : PCBM on electrodeposited ZnO compared to ITO. The cell containing ZnO retained 80.7 % of the original η_p, against 37.3 % for the ITO cell, after 40 hours constant illumination.[67]

The encapsulation of cells, to act as a barrier to unwanted oxygen and moisture diffusion,[79, 185] and the replacement of ITO with a more stable electrode material will produce future improvements for cell stability.[83] Specialist equipment and experimental methods are required for the design and evaluation of cell stability.[186, 187] This has resulted in a new field of research, with groups focused on stability effects and causes.

3.2.6 Inverted cell architecture

Inverted cell architectures allow for the use of different exciton blocking layers. This can open up the possibility of improved η_p, increased stability and novel nanostructuring.[188] However, the hole extracting layer between the donor and metal back electrode also needs to be carefully selected. PEDOT : PSS is not a viable option since this requires the small molecule photo-active layers to undergo air and water exposure during the spin-coating process and subsequent annealing steps.

Hence, a layer that can be fabricated quickly and without breaking vacuum would be favourable, with MoO$_x$ proposed as an ideal candidate. Therefore, inverted cells with the structure ITO / 5 nm BCP / 40 nm C$_{60}$ / 14 nm SubPc / 5 nm MoO$_x$ / Al were fabricated, with *J-V* curves presented in Figure 3.24.
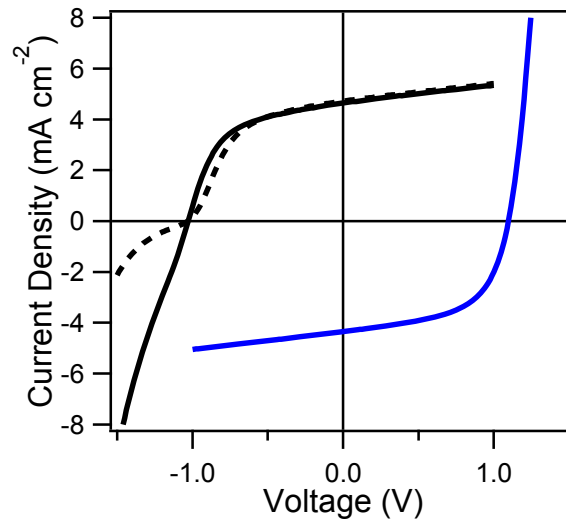
Figure 3.24: *J-V* curves measured under 1 sun illumination for cells with structure ITO / 5 nm MoO$_x$ / 14 nm SubPc / 40 nm C$_{60}$ / 8 nm BCP / Al (standard architecture, blue line) and ITO / 5 nm BCP / 40 nm C$_{60}$ / 14 nm SubPc / 8 nm MoO$_x$ / Al (inverted architecture, black line) after 0 (dotted) and 6 minutes illumination(solid).

The performance of the standard architecture cell is highest at the initial measurement, with degradation thereafter. In contrast, for the inverted cells it took 6 minutes of constant illumination to achieve the highest η_p before subsequent performance degradation. Consequently, both the initial (black dotted line) and optimal (black solid line) *J-V* curves are presented in Figure 3.24. The inverted cell achieved a V_{oc} of 1.03 V at both 0 and 6 minutes illumination, a J_{sc} that marginally decreased from 4.71 to 4.64 mA cm^{-2} after illumination and a *FF* that increased from 0.49 to 0.54, due to a considerably improved R_s. Thus, the cell had an initial η_p of

2.38 %, which increased to 2.58 % after illumination. The need for illumination to increase cell performance can be understood by looking at the order of material deposition. In the inverted cells the exciton blocking layer, BCP, is deposited directly onto the ITO, with a C$_{60}$ layer sequentially deposited on the BCP. In a standard architecture the BCP was used as both an exciton blocking layer and a sacrificial material to prevent reactions between C$_{60}$ and the hot Al deposition.[73] The metal deposition causes additional defect states within the band gap of the BCP, which are required to maximise performance.[73] With the BCP layer shielded from the hot metal, Rand *et al.* found performance was compromised. In addition, a reduced *FF* in standard architecture devices was demonstrated for layers thicker than the 10 nm metal penetration depth that caused the extra defects.[73] Further studies would be required to fully understand the cause of the improvement of inverted cell performance.

These initial studies of the inverted cell obtain a similar overall performance to the standard architecture SubPc / C$_{60}$ cells. These results indicate that the exciton blocking and hole extracting layers effectively 'decouple' the photo-active materials from the properties of the electrode. If the electrode work functions (ITO ~ 4.6 - 4.8 and Al 4.2 eV) were the outright determining factor for deciding the direction of the photo-generated charge extraction then the inverted cell would suffer a considerable loss of performance. Therefore, as a similar η_p was possible for both architectures, the electronic effects of the charge transport materials and the order of the photo-active layer deposition dominated the cell performance. This provides fewer cell design restrictions via the undemanding modification of electrode materials with hole extracting layers. The electrode transparency and conductivity, not energy level alignment, become significantly more important factors to consider in electrode

design. For example, the widely used relatively low work function metal Al can still be utilised as a back contact for inverted cells alongside the incorporation of the MoO$_x$ layer. This avoids the requirement of more expensive higher work function metals such as gold as back contacts.[67]

3.3 Conclusion

The optimum thickness of the MoO$_x$ hole transport layer in OPV cells was found to be 5 nm for the ClAlPc / C$_{60}$ system. The metal oxide acted as a relatively transparent hole extracting material which followed the surface topography of the underlying ITO. When used in OPV cells, the MoO$_x$ layer allows for considerable increases in V_{oc} (~ 0.3 V) for the high ionisation potential donor materials ClAlPc and SubPc, with only small losses in J_{sc}. This gave a concomitant enhancement of η_p from 1.65 and 1.85 % on bare ITO to 2.60 and 2.53 % on MoO$_x$ for cells employing ClAlPc and SubPc respectively. However, for cells using the lower ionisation potential materials, pentacene and CuPc, a similar V_{oc} on MoO$_x$ and bare ITO was found. With a reduced J_{sc} due to the detrimental MoO$_x$ absorption between 400 - 600 nm, this accordingly lowered the η_p from 1.11 and 1.38 % on bare ITO to 1.03 and 1.24 % on 5 nm MoO$_x$ for the CuPc and pentacene based cells respectively.

XRD, UV-vis absorption spectroscopy and AFM experiments showed no noticeable structural or morphological changes to the donor materials with MoO$_x$ inclusion. Significant electronic effects were demonstrated, with MoO$_x$ shown to be an n-type material, with a high work function value of 6.4 eV. Sequential deposition and UPS measurements of ClAlPc on MoO$_x$ showed favourable band bending of the ClAlPc HOMO towards the MoO$_x$ Fermi level, maximising the built-in field of the cells. This facilitates enhanced V_{oc} values for the high ionisation potential materials.

Additionally, the UPS revealed states within the band gap of the MoO$_x$ due to the substoichiometric character of the thermally evaporated layer. Since the valence band of the MoO$_x$ is situated 2.7 eV below the Fermi level, a large barrier for hole extraction via the valence band is formed. The position of the additional states near to the MoO$_x$ Fermi level indicates they may play a role in hole extraction. It is tentatively proposed that hole extraction in OPV cells could occur through these partially filled states, although it is acknowledged that current literature is divided over both the presence and role of the states.

It has been demonstrated that MoO$_x$ considerably increased the stability of OPV cells in both shelf life and constant illumination tests. A T80 shelf life of ~ 106.0 days was extrapolated for the SubPc / C$_{60}$ cell on MoO$_x$, compared to the observed ~ 33.8 days on ITO. Under constant illumination for 24 hours, OPV cells containing MoO$_x$ retained 62 % of the original performance, compared to only 6 % on ITO. The MoO$_x$ acts as a physical barrier to oxidation of the active layer caused by ITO.

The MoO$_x$ and BCP layers were shown to effectively decouple the photo-active materials of the OPV cell from the ITO and Al electrodes. This was demonstrated by the inversion of SubPc / C$_{60}$ cell architecture, with a η_p of 2.58 % achieved. This opens up the potential for new materials, fabrication techniques and low cost electrodes to be used in the future.

Chapter 4: A thermally evaporated V_2O_x hole extracting layer in OPV cells

With MoO_x revealed to be a high work function n-type hole extracting layer, this chapter examines if a thermally evaporated V_2O_x has similar properties and could be used as an alternative hole extracting layer. Using *in-situ* layer growth and UPS characterisation the electronic properties of the metal oxide and subsequently deposited organic layers were determined. The performance of SubPc / C_{60} and CuPc / C_{60} systems on the V_2O_x layer were compared to deposition onto ITO (Thin Film Devices), allowing an insight into the role of the metal oxide layer in OPV cells.

4.1 V_2O_x used in the SubPc / C_{60} system

4.1.1 Cell performance of the SubPc / C_{60} system

Cells with the architecture ITO / d nm V_2O_x / 14 nm SubPc / 40 nm C_{60} / 8 nm BCP / Al were fabricated where d = 0, 2.5, 5 and 7.5 nm of V_2O_x with the *J-V* curves shown and performance data in Figure 4.1. When deposited on bare ITO the cells showed a similar performance to those reported in Section 3.2.1. A considerable increase in cell performance is seen with the insertion of the V_2O_x layer, with the 5 nm thick film permitting a slightly favourable performance compared to the 2.5 and 7.5 nm thick layers. Therefore, all further studies in this chapter were carried out on the 5 nm layer. The *J-V* curves in Figure 4.1 show a large increase in V_{oc} from 0.81 V to 1.10 V for fabrication on the 5 nm V_2O_x layer compared to bare ITO. Although there was a loss in J_{sc} from 4.80 mA cm^{-2} to 4.11 mA cm^{-2}, there was also an increase in *FF* from 0.50 to 0.54 when utilising 5 nm of

V$_2$O$_x$. This led to a substantial improvement in η_p from 1.98 % on bare ITO to 2.50 % for cells incorporating the V$_2$O$_x$ layer. The *J-V* curves with V$_2$O$_x$ showed a significant decrease in R_s, without the kink displayed in the reference cells. As stated previously with the MoO$_x$ layer, the kink indicates a barrier to charge extraction, which suggests a reduced barrier to hole extraction at the V$_2$O$_x$ / SubPc interface.
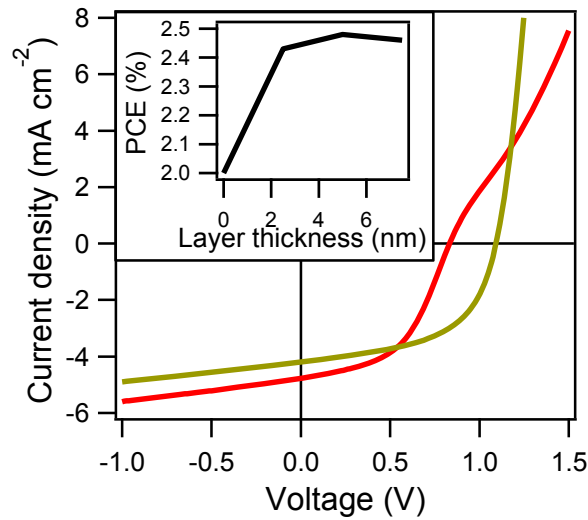
Figure 4.1: *J-V* curves obtained under AM 1.5G illumination for OPV cells with the structure ITO / *d* nm V$_2$O$_X$ / 14 nm SubPc / 40 nm C$_{60}$ / 8 nm BCP / Al, where *d* = 0 (red line) and 5 nm (gold line). Inset: η_p against *d*, where *d* = 0 - 7.5 nm.

With similar cell performance for the SubPc / C$_{60}$ system on both the V$_2$O$_x$ and the MoO$_x$ hole extracting layer, similarities were expected for the surface morphology and transmittance of the metal oxide. Figure 4.2 shows the topography of ITO and ITO / 5 nm V$_2$O$_x$, with R_q values of 0.56 and 0.63 nm respectively. Lower R_q values were obtained compared to those in Section 3.1.2 due to a change of ITO supplier. With similar surface morphologies and R_q, the V$_2$O$_x$ appeared to cover the ITO surface homogeneously, as demonstrated previously with MoO$_x$. This

was again in contradiction to the large island features observed by Shrotriya *et al.*, where R_q increased three fold with deposition of V_2O_x.[107]
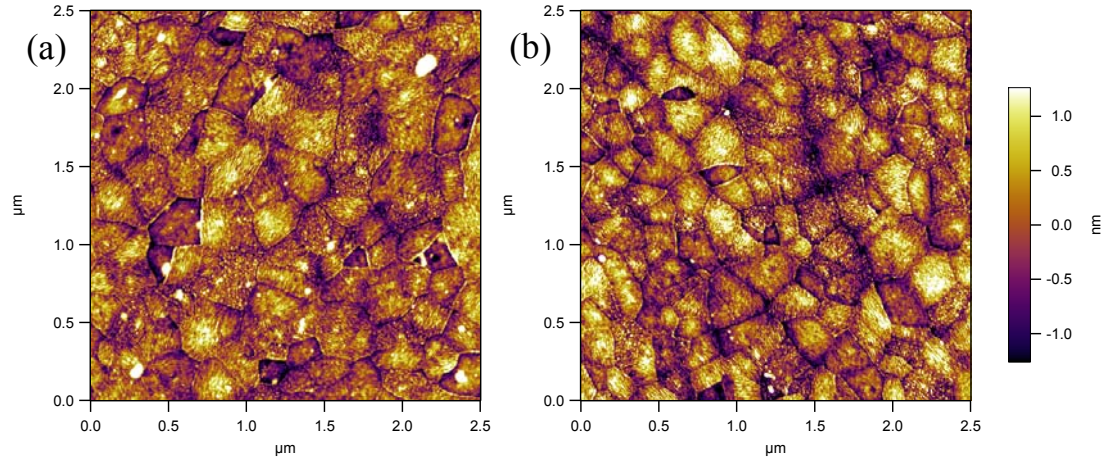
Figure 4.2: 2.5 µm AFM topographical images of (a) bare ITO and (b) ITO / 5 nm V_2O_x. Both images have a height scale ± 1.5 nm.

Figure 4.3(a) shows the transmittance of V_2O_x (black line) in comparison to the transmittance of MoO_x (dotted blue line) with the absorption profiles of SubPc and C_{60} layers also displayed. The V_2O_x had a reduction of transmittance to around 90 % at 415 nm, with broad losses between 380 and 500 nm. Therefore a greater loss of transmittance was found compared to the MoO_x layer in this region with an expected reduction of current generated in the C_{60} region. These transmittance losses were the probable cause of the reduction in J_{sc} from 4.80 mA cm^{-2} on ITO to 4.11 mA cm^{-2} on the V_2O_x layer for the SubPc / C_{60} cells. Above 500 nm the layer exhibited marginally improved transparency compared to the MoO_x layer, the region where SubPc absorption occurs.

A plot of $(E \times \alpha)^{1/2}$ against energy for the V_2O_x layer is displayed in Figure 4.3(b). The intercept of a linear fit of the absorption edge onset with the x-axis can

be used to estimate the band gap of transition metal oxides, as previously shown in Section 3.1.2.[149] The inset of Figure 3.2(a) demonstrated that the analogous plot for the MoO_x layer contained additional absorption features at a lower energy than the main absorption edge onset, however these features did not interfere with the estimate of the intercept. Figure 4.3(b) shows complications for the determination of the V_2O_x band gap, as the additional absorption features of V_2O_x overlap with the main onset of the absorption edge. Consequently, a linear fit (black dotted line) has been added to allow for the estimation of the band gap. The fit estimated a band gap value of 2.9 eV for the V_2O_x layer, close to the 2.8 eV measured by Mayer *et al.* by combined UPS and inverse photoemission spectroscopy (IPES) techniques.[189]
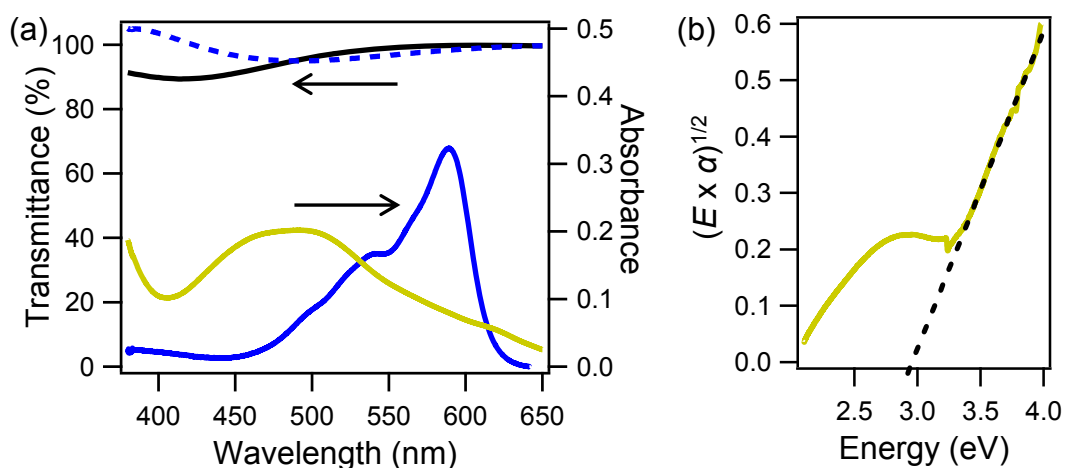
Figure 4.3: (a) Transmittance of V_2O_x (solid black line) and MoO_x (dotted blue line) against an ITO background, with absorbance for SubPc (solid blue line) and C_{60} (yellow line). (b) plot of $(E \times \alpha)^{1/2}$ against energy for a V_2O_x layer (yellow line) with a linear fit (black dotted line).

4.1.2 Electronic effects of V_2O_x on the SubPc / C_{60} system

Comparable electronic properties were expected for V_2O_x and MoO_x due to the analogous improvement of cell performance. Literature reports often reference

the work of Shrotriya *et al.* when discussing the electronic properties of V_2O_x,[107] in a similar manner to the MoO_x layer discussed in Section 3.1.4.[190, 191] Therefore, V_2O_x has been assumed to be p-type, with a relatively low work function value of only 4.7 eV. Hole extraction was assumed to occur through the V_2O_x valence band. This low reported work function would indicate that a poor performance should be expected when using the V_2O_x layer with high ionisation potential donor materials such as SubPc, in contrast to what has been demonstrated here.

A UPS study of the electronic characteristics of the metal oxide and the impact on subsequent SubPc layers is displayed in Figure 4.4, allowing comparisons to the study of fabrication on bare ITO in Figure 4.5. Figure 4.4(a) shows the secondary electron cut-off region for ITO, 5 nm V_2O_x and 1, 5 and 14 nm of SubPc. Figure 4.4(b) shows the valence band UPS spectra for 5 nm V_2O_x and the HOMO onset of the 1, 5 and 14 nm SubPc layers. The bare ITO has a work function of 4.3 eV. The spectrum for the 5 nm V_2O_x layer reveals a clear shift in work function to 6.8 eV. The large work function difference between the surfaces leads to a significant interface dipole due to electron transfer from ITO to V_2O_x, resulting in a large vacuum level (V_l) shift of 2.5 eV. The V_2O_x work function value is far greater than that previously reported,[107] and close to the value that MoO_x exhibited in Section 3.1.4. The UPS spectrum indicates the valence band to be positioned 2.5 eV below the Fermi level of the 5 nm V_2O_x layer, resulting in an ionisation potential energy of 9.3 eV. With a band gap of 2.9 eV determined from Figure 4.3(b) the V_2O_x conduction band resides 0.4 eV above the Fermi level. This indicates that V_2O_x has a strongly n-type character, similar to our findings for MoO_x rather than the previously reported p-type character.[107] In Figure 4.4(b) additional features were positioned from 0.6 eV to 2.1 eV below the Fermi level of the V_2O_x layer. These were

comparable to those seen for the MoO_x layer. Thus, thermally evaporated V_2O_x also gave a substoichiometric layer, due to the oxygen deficient metal oxide.
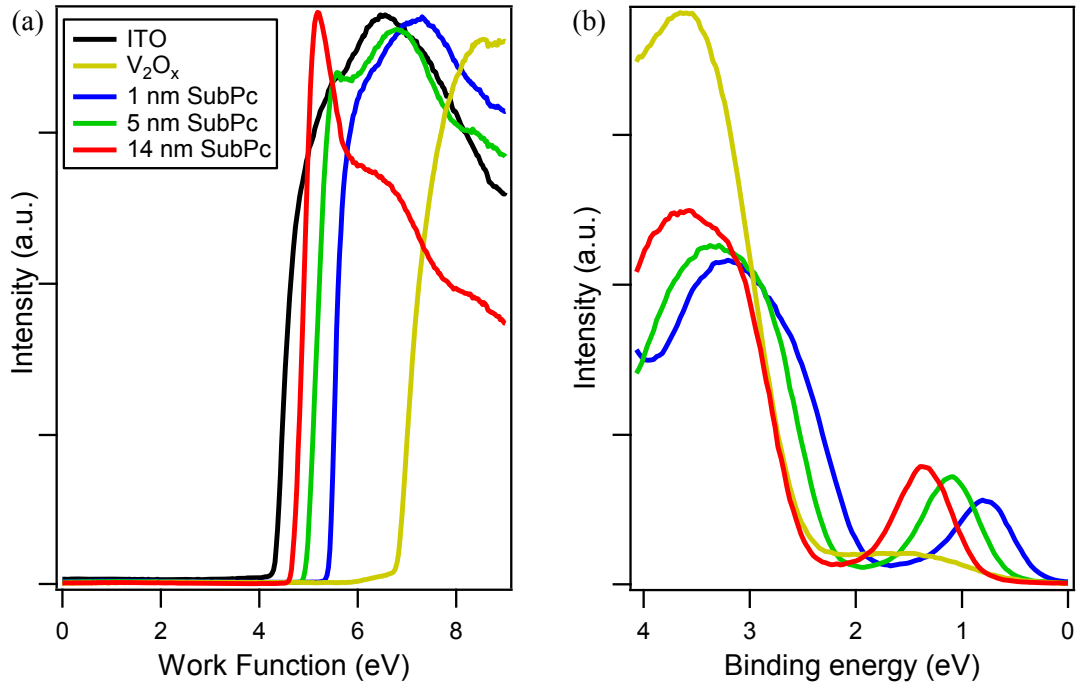
Figure 4.4: (a) Onset of the secondary electron cut-off and (b) valence band UPS spectra for ITO (black line) / 5 nm V_2O_x (gold lines) / 1nm (blue lines), 5 nm (green lines), 14 nm (red lines) SubPc.

The UPS spectra of the 1 nm SubPc layer indicates a large work function difference between the metal oxide and the donor material and accordingly an interface dipole forms between the SubPc and V_2O_x with a V_l shift of 1.4 eV. Work function values of 5.4, 5.0 and 4.7 eV were found for the 1, 5 and 14 nm thick SubPc layers respectively. This band bending was due to a Fermi level pinning effect at the V_2O_x / SubPc interface, with electron transfer from the organic to the metal oxide. This was previously shown in Section 3.1.4 for the ClAlPc layer deposited onto the high work function MoO_x surface. The 1 nm SubPc layer demonstrated a HOMO

onset 0.3 eV below the Fermi level, whereas the 5 and 14 nm SubPc HOMO onsets were 0.6 and 0.9 eV below the respective Fermi levels. Therefore, the 1, 5 and 14 nm thick SubPc layers have ionisation potentials of 5.7, 5.6 and 5.6 eV respectively. These are close to the literature value of 5.6 eV.[109]

For comparison the SubPc was grown directly onto ITO, with UPS spectra presented in Figure 4.5. Figure 4.5(a) shows the secondary electron cut-off region for ITO and 1, 5 and 14 nm of SubPc, with Figure 4.5(b) displaying the HOMO onset of the 1, 5 and 14 nm SubPc layers. The ITO work function was measured to be 4.1 eV. When deposited on bare ITO there was a small V_l shift of 0.1 eV between the ITO and a 1 nm SubPc layer. With the 5 nm SubPc layer displaying the same work function value of 4.2 eV. At 14 nm of SubPc the work function returned to 4.1 eV. These values are 1.2, 0.8 and 0.6 eV smaller than those of the respective 1, 5 and 14 nm SubPc layers deposited on to the V_2O_x surface. Offsets of 1.3, 1.4 and 1.5 eV between the respective Fermi level and the HOMO level of the 1, 5 and 14 nm layers of SubPc on ITO, consequently the ionisation potentials are 5.5, 5.6 and 5.6 eV. These were equivalent to the SubPc ionisation potentials reported elsewhere.[109]
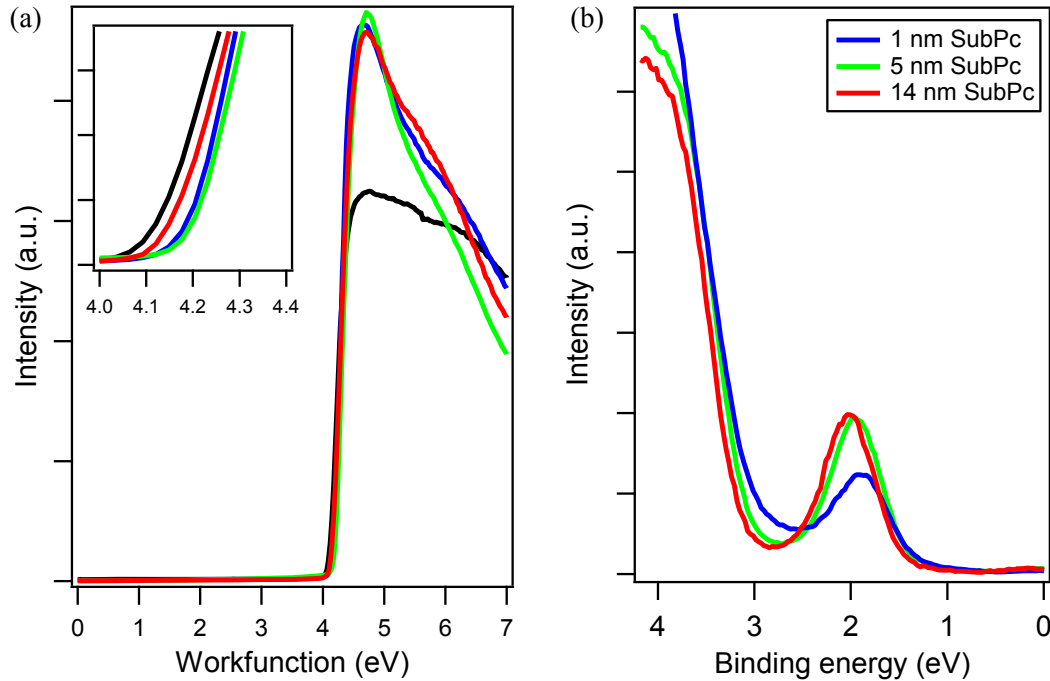
Figure 4.5: (a) Onset of the secondary electron cut-off and (b) valence band UPS spectra for ITO (black line) / 1 nm (blue lines), 5 nm (green lines), 14 nm (red lines) SubPc. Inset (a): enlargement of cut-off region.

Figure 4.6 presents the energy level schematic of the ITO / V_2O_x / SubPc and ITO / SubPc interfaces derived from the UPS data. Figure 4.6(a) shows the n-type character of V_2O_x, with Fermi level pinning and band bending of the SubPc layer due to the large interface dipole that was formed. The high work function value of V_2O_x and subsequent pinning of the organic indicates it obeyed the 'mark of Zorro' rule that was described for the MoO_x / ClAlPc interface in Section 3.1.4. Thus, the V_{bi} is maximised and consequently a high V_{oc} was obtained for the cells. Figure 4.6(a) additionally shows that the position of the HOMO level of the 1 nm SubPc layer would create a large barrier for hole extraction through the V_2O_x valence band. As with MoO_x, the position of the additional gap states that occur due to the partial reduction of V_2O_x would allow a favourable energy level alignment for efficient hole

extraction. The overlap of these gap states with the SubPc HOMO can be seen in Figure 4.4(b). Therefore, this is one possible mechanism for hole extraction. However, Meyer *et al.* have since also published work that shows n-type character for the V$_2$O$_x$ layer, and just as with the MoO$_x$ layer they did not observe the presence of the gap states.[189]
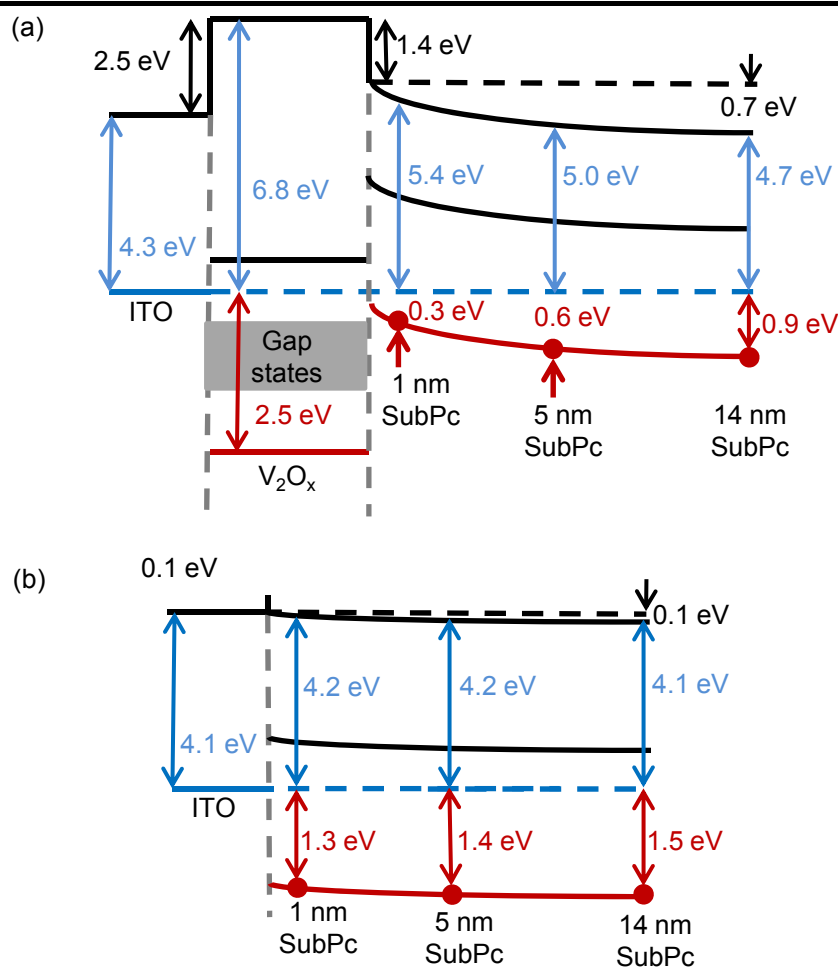
Figure 4.6: Schematic energy level diagram for the (a) ITO / V$_2$O$_x$ / 1, 5 and 14 nm SubPc and (b) ITO / 1, 5 and 14 nm SubPc interfaces.

Figure 4.6(b) indicated a large mismatch of 1.3 eV between ITO and the HOMO of the 1 nm SubPc layer. Negligible pinning of the organic was observed due to the relatively low ITO work function. As a result, there was a reduction in the V_{bi}

of the cell, causing the kink produced in the ITO cell *J-V* curve, in addition to providing a lower V_{oc} compared with cells fabricated on the V_2O_x layer.

4.2 V_2O_x used in the CuPc / C_{60} system

4.2.1 Cell performance of the CuPc / C_{60} system

Cells with the architecture ITO / *d* nm V_2O_x / 30 nm CuPc / 40 nm C_{60} / 8 nm BCP / Al were fabricated where *d* = 0 and 5 nm, with *J-V* curves for the cells shown in Figure 4.7. When deposited directly onto ITO the cells had a J_{sc} of 3.99 mA cm^{-2}, a V_{oc} of 0.47 V, a *FF* of 0.57, and consequently a η_p of 1.07 %. With the V_2O_x hole extracting layer similar V_{oc} and *FF* values of 0.47 V and 0.56 were obtained but J_{sc} was reduced to 3.52 mAcm^{-2}, leading to a reduction of η_p to 0.93 %.
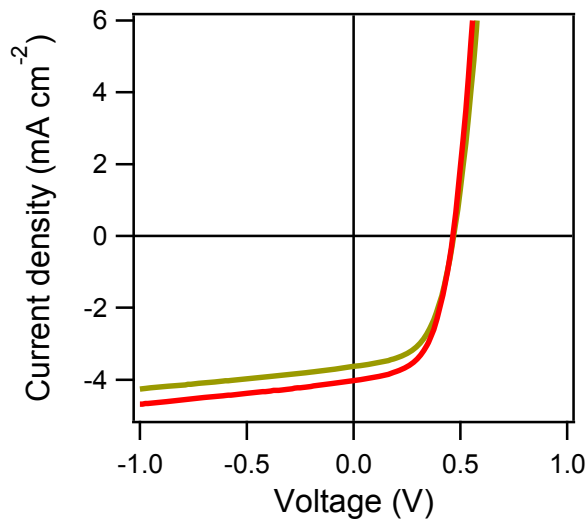
Figure 4.7: *J-V* curves obtained under AM 1.5G illumination for OPV cells with the structure ITO / *d* nm V_2O_X / 30 nm CuPc / 40 nm C_{60} / 8 nm BCP / Al, where *d* = 0 (red line) and 5 nm (gold line).

This set of cells showed similar characteristics to those seen in Section 3.2.2, with the comparison of CuPc / C_{60} cells deposited on to MoO_x and bare ITO. However, a larger reduction in J_{sc} was obtained on V_2O_x as was also seen in the SubPc / C_{60} cells. These findings are expected since there was a greater loss in transmittance between 350 and 500 nm with the V_2O_x layer, and hence a comparable decrease in J_{sc}.

4.2.2 Electronic effects of V_2O_x on the CuPc / C_{60} system

In order to explore the electronic factors behind the V_{oc} values obtained for CuPc / C_{60} cells on both bare ITO and V_2O_x a UPS study for each was conducted and are shown in Figures 4.8 and 4.9 respectively. Figure 4.8(a) shows bare ITO has a work function of 4.4 eV. The 1 nm layer of CuPc experienced a 0.1 eV work function shift to 4.3 eV. The 5 and 14 nm CuPc layer thicknesses both had work function values of 4.1 eV, a reduction of 0.2 eV compared to the 1 nm layer. The HOMO onsets in Figure 4.8(b) for the 1, 5 and 14 nm CuPc layers are 0.7, 0.8 and 0.7 eV below the respective Fermi level. Hence, the measured ionisation potentials are 5.0, 4.9 and 4.8 eV, for 1, 5 and 14 nm CuPc layers respectively. This was marginally lower than the 4.95 - 5.20 eV reported in literature, and ~ 0.7 eV smaller than that of the SubPc layers.[109, 110]
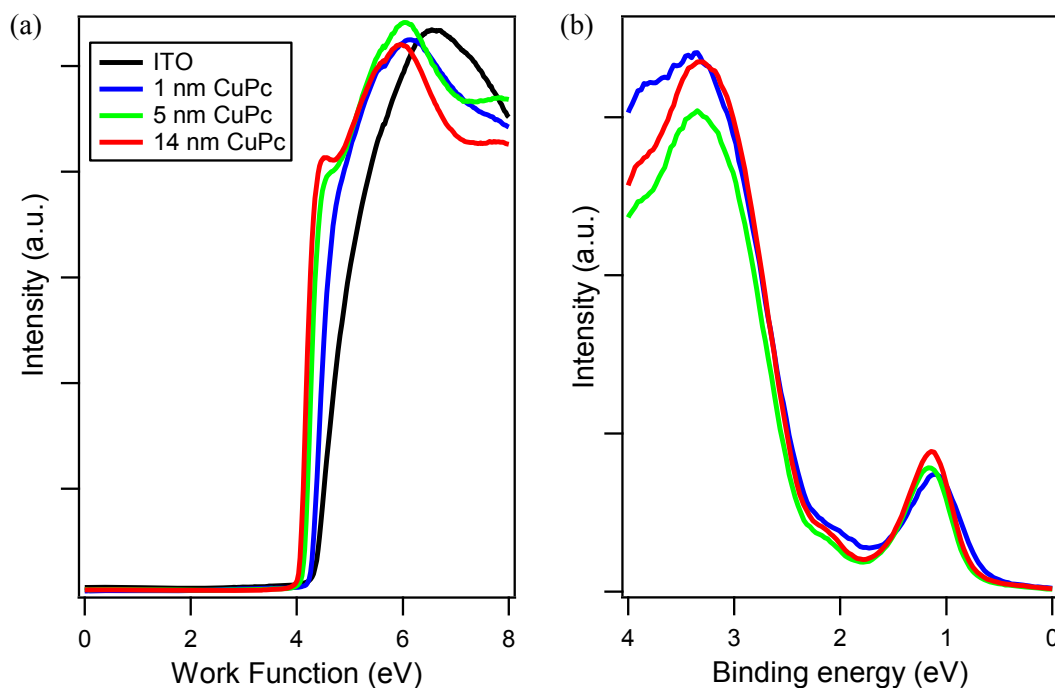
Figure 4.8: (a) Onset of the secondary electron cut-off and (b) valence band UPS spectra for ITO (black line) / 1nm (blue lines), 5 nm (green lines), 14 nm (red lines) CuPc.

Figure 4.9(a) presents the secondary electron cut-off region for ITO, 5 nm V_2O_x and 1, 5 and 14 nm of SubPc. Figure 4.9(b) shows the valence band UPS spectra for the 5 nm V_2O_x layer and the HOMO onset of 1, 5 and 14 nm of SubPc. Here, ITO is shown to have a work function of only 3.9 eV. Whilst this value was relatively low compared to the previous measurements, it can be explained by the ITO surface treatment used. The UV ozone treatment and transfer of the ITO into the UHV system was the only part of the measurement process that cannot be done *in-situ*. The UV ozone treatment of the ITO is an important cleaning step, removing residual organic contaminants and consequently leading to the increased work function of the ITO surface.[57, 192] When fabricating cells the time taken between UV ozone treatment of ITO and transfer into the N_2 filled glovebox was ~ 1 minute. When measured by KP (under N_2) the work function of freshly treated ITO varies

between 4.6 - 4.8 eV. Cook *et al.* presented data that showed that the work function of UV ozone treated ITO was unstable over time even under a N_2 atmosphere.[57] It should therefore be unsurprising that the surface contamination and work function should change with post treatment exposure to ambient conditions. In order to obtain UPS spectra after UV ozone treatment, the ITO has to be mounted, transferred carefully into a carousel and then the chamber pumped down. This takes several additional minutes of ambient exposure to complete compared to direct transfer into a glovebox. As a result, the work function of the ITO measured by UPS in this report varies between 3.9 - 4.5 eV, in comparison to 4.6 - 4.8 eV when measured by KP.
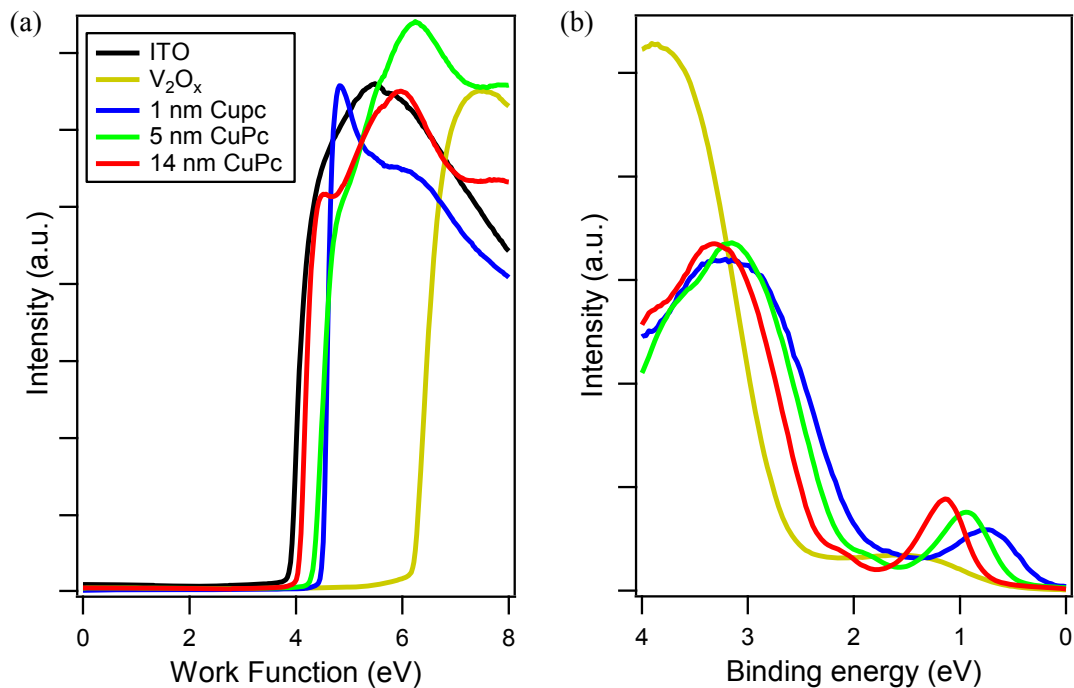
Figure 4.9: (a) Onset of the secondary electron cut-off and (b) valence band UPS spectra for ITO (black line) / 5 nm V_2O_x (gold lines) / 1nm (blue lines), 5 nm (green lines), 14 nm (red lines) CuPc.

Despite this, a high work function value of 6.2 eV was obtained for the 5 nm V_2O_x layer, forming a large interface dipole with ITO. The onset of the valence band was 2.6 eV below the Fermi level of V_2O_x, resulting in an ionisation potential of 8.8 eV. The layer also displayed the presence of additional states and n-type behaviour described in Section 4.1.2.

The work function values of 1, 5 and 14 nm layers of CuPc are 4.5, 4.3 and 4.0 eV respectively, hence a large interface dipole was formed between the V_2O_x and the 1 nm CuPc layer, and accordingly a 1.7 eV V_l shift was observed. The UPS data reveals Fermi level pinning and band bending effects of the CuPc layer when fabricated on V_2O_x, as was also seen with the higher ionisation potential donors. Figure 4.9(b) indicates the HOMO onset for the CuPc layers were 0.2, 0.5 and 0.8 eV below the Fermi level for 1, 5 and 14 nm CuPc films respectively, resulting in ionisation potentials of 4.7, 4.8 and 4.8 for the 1, 5 and 14 nm CuPc layers, comparable to the ionisation potentials measured on bare ITO.

Figure 4.10 presents an energy level schematic for the CuPc / C_{60} system on each interface. Despite obtaining a comparable V_{oc} to the cell fabricated on ITO, there was considerable Fermi level pinning of the CuPc on V_2O_x, as was exhibited for the higher ionisation potential materials. Just as with SubPc on V_2O_x, there is a large barrier for hole extraction through the valence band of V_2O_x and the need for another mechanism for extraction as described in Section 3.1.4. Obvious parallels can be made between the role of the V_2O_x and MoO_x within OPV cells, consequently allowing the materials to be used interchangeably to an extent.
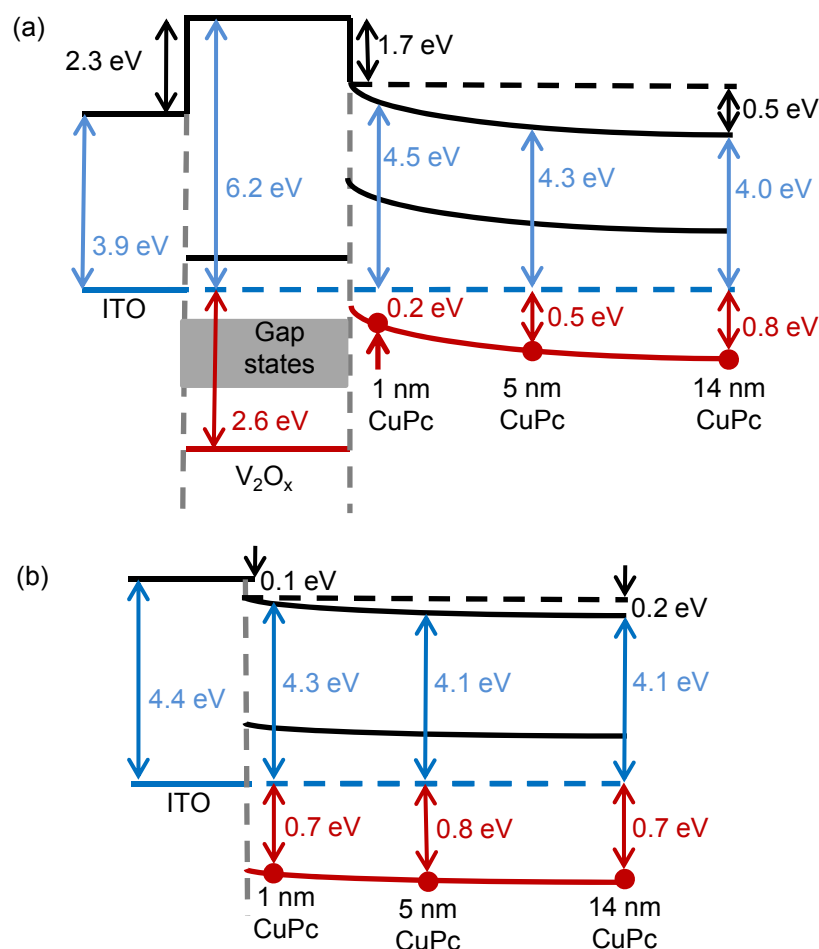
Figure 4.10: Schematic energy level diagram for the (a) ITO / V_2O_x / 1, 5 and 14 nm CuPc and (b) ITO / 1, 5 and 14 nm CuPc interfaces.

In comparison, considerably less Fermi level pinning was demonstrated with the deposition of CuPc onto bare ITO, highlighted by a 0.2 eV V_l shift only from the 1 nm to the 5 nm CuPc layer. This was however in contrast to identical work function values obtained for 1 and 5 nm SubPc layers on bare ITO. Whilst the effect was only marginal with the CuPc layers measured on V_2O_x, it may indicate that the ITO work function of 4.4 eV was close or equal to the E_{ICT+} value of CuPc. Indeed, CuPc exhibited an ionisation potential of ~ 5.0 eV which is close to the work function value of a freshly ozone treated ITO substrate, measured to be 4.6 - 4.8 eV

by KP. Consequently, during cell fabrication the CuPc E_{ICT+} value may actually be equal or lower than the work function value of ITO. Thus, no detrimental effect was found for cell η_p with growth on ITO. It could be assumed that the V_{bi} of the cell on ITO was large enough to maximise the V_{oc} of the cell, with no need for an hole extracting layer at the anode.

4.3 Conclusion

In summary, it was shown that thermally evaporated thin films of V$_2$O$_x$ increased the performance of SubPc / C$_{60}$ OPV cells compared to deposition on bare ITO. This was largely due to a considerable increase in V_{oc} from 0.81 to 1.10 V. The V$_2$O$_x$ hole extracting layer has been determined to be highly n-type, in contrast to the literature reports of p-type behaviour. This was due to a large work function and a very low lying valence band. The large work function led to band bending of the donor material towards the V$_2$O$_x$ Fermi level. Hence, a smaller reduction in V_{bi} for the cell was encountered compared to fabrication on ITO, and consequently higher V_{oc} values were achieved. The V$_2$O$_x$ layer contained gap states due to oxygen deficiencies close to the Fermi level of the material, as was observed with MoO$_x$. We propose one possible mechanism of hole-extraction from the SubPc HOMO was through these gap states since there was a large barrier to extraction through the metal oxide valence band. The V$_2$O$_x$ layer was too thick to allow the direct tunnelling of charges.

With the lower ionisation potential donor CuPc, a comparable V_{oc} was obtained with photo-active layer deposition onto ITO and V$_2$O$_x$. Due to a reduced transmittance, the cells deposited on V$_2$O$_x$ suffer a reduced η_p from 1.07 to 0.93 %. UPS studies revealed significant band bending still occurred for CuPc on V$_2$O$_x$ and

this was less noticeable on ITO. However, a relatively low work function was required with the CuPc donor in order to maximise the V_{oc} of the system. Consequently, performance was marginally compromised when using the hole extracting layer due to the losses in transmittance.

Therefore, V_2O_x has a possible application for use as a thermally evaporated hole-extracting layer within OPV cells, particularly for use with high ionisation potential donors in order to maximise cell V_{oc}. It can be used as a direct alternative to other metal oxide layers such as MoO_x.

Chapter 5: A solution processed V$_2$O$_x$ hole extracting layer in OPV cells

This chapter focuses on the optimisation and characterisation of a solution processed V$_2$O$_x$ (V$_2$O$_{x(sol)}$) hole extracting layer. Spin-coated PEDOT : PSS films are commonly used in polymer : fullerene cell architectures but suffer from several drawbacks, such as delamination from the electrode surface.[193] Therefore, a high work function V$_2$O$_{x(sol)}$ hole extracting layer was developed as a direct replacement material. The V$_2$O$_{x(sol)}$ layer was processed under a range of conditions and characterised using UV-vis absorption spectroscopy, XPS, KP and UPS. A series of SubPc / C$_{60}$ cells were used to determine the optimal fabrication parameters of the layer, before a direct comparison to ITO (Thin Film Devices), MoO$_x$ and PEDOT : PSS hole extracting layers incorporated into both SubPc / C$_{60}$ and P3HT : PCBM cell architectures.

5.1 Optimisation of solution processing conditions

5.1.1 Variation of spin-coating speed

In comparison to the thermally evaporated V$_2$O$_x$ hole extracting film, solution processing of layers requires the optimisation of a greater variety of parameters. These include solution concentration, processing speed and film annealing conditions, and determining the optimal parameters is often a process of trial and error.

The starting material of vanadium (V) oxytriisopropoxide (Sigma-Aldrich) was used in a 1:40 volume ratio with anhydrous IPA (Sigma-Aldrich, 99.5 %) throughout. The solution was spin-coated onto freshly solvent and UV ozone treated ITO at between 1500 - 6000 rpm under a N$_2$ atmosphere to give a range of layer thicknesses. The films were annealed at 140 °C for 2 minutes before transfer into a OMBD system for photo-active layer and metal electrode deposition.
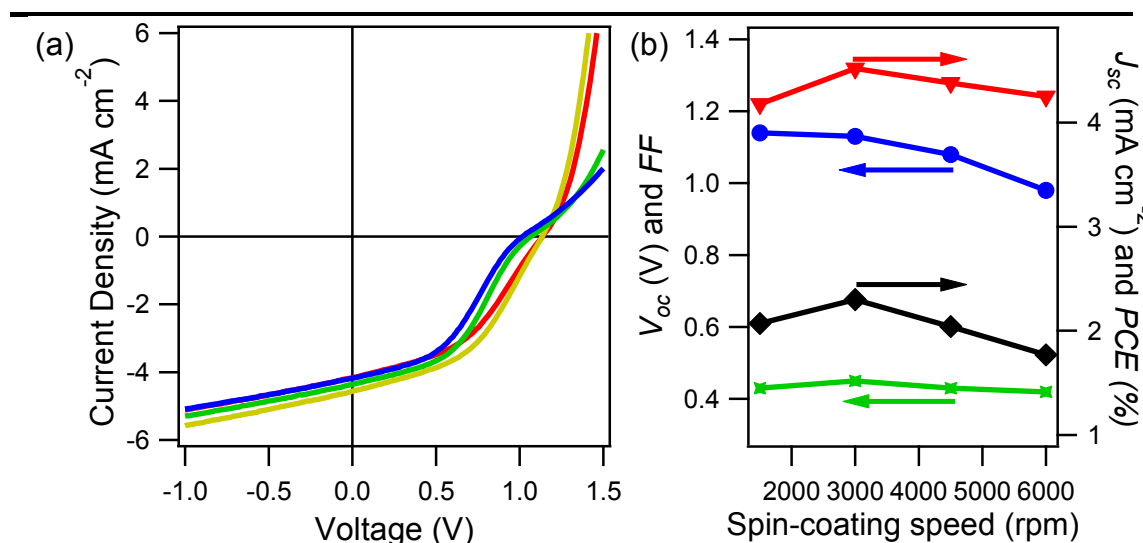
Figure 5.1: (a) *J-V* curves obtained under 1 sun illumination for cells with the structure ITO / V$_2$O$_{x(sol)}$ / 14 nm SubPc / 40 nm C$_{60}$ / 8 nm BCP / Al, with spin-coating speeds of 1500 (red line), 3000 (gold line), 4500 (green line) and 6000 rpm (blue line). (b) Variation of key cell parameters with spin-coating speed, *J*$_{sc}$ (red line), *V*$_{oc}$ (blue line), *FF* (green line) and η_p (black line).

For interfacial layer optimisation, cell architectures of 14 nm SubPc / 40 nm C$_{60}$ / 8 nm BCP / Al were fabricated on the ITO / V$_2$O$_{x(sol)}$ films and *J-V* curves are shown in Figure 5.1(a) with variation of key cell parameters illustrated in Figure 5.1(b). V$_2$O$_{x(sol)}$ layers spin-coated at 1500 rpm gave a *J*$_{sc}$ of 4.18 mA cm^{-2}, with a *V*$_{oc}$ of 1.14 V and a *FF* of 0.43. These cells produced a η_p of 2.07 %. Cell

performance was enhanced to 2.30 % by spin-coating V$_2$O$_{x(sol)}$ layers at 3000 rpm, increasing J_{sc} to 4.52 mA cm^{-2} whilst obtaining a V_{oc} of 1.13 V and a FF of 0.45. For spin speeds beyond 3000 rpm the cell performance decreased. This was due to noticeable losses in V_{oc} and to a lesser extent J_{sc} and FF. Consequently η_p was reduced to 2.04 and 1.77 % for spin-coating layers at 4500 and 6000 rpm respectively.

By increasing the spin-coating speed from 1500 to 3000 rpm the V$_2$O$_{x(sol)}$ layers become thinner, reducing transmittance losses and so allowing an increase of J_{sc}. The high V_{oc} values and similar FF for both spin speeds suggests a complete coverage of the ITO surface was achieved. By increasing the spin-coating speed to 4500 and 6000 rpm, V_{oc} was compromised and an additional kink appears near V_{oc}. A similar kink had previously been shown (Sections 3.2.1 and 4.1.1) for SubPc / C$_{60}$ on bare ITO, with cells obtaining lower V_{oc} values. There the kink was indicative of the poor hole extraction of ITO. Here, the kink is most likely due to partial ITO surface coverage by the V$_2$O$_{x(sol)}$ layer, with the feature becoming more noticeable at 6000 rpm compared to 4500 rpm, and a lower V_{oc} was acquired with the reduced coverage. The J-V curves can therefore be thought of as a combination of areas of both bare ITO and of ITO / V$_2$O$_{x(sol)}$. The 3000 rpm spin speed gave the optimum layer in terms of cell performance, and consequently spin-coating of the solution was conducted at 3000 rpm for the remainder of this chapter.

5.1.2 Variation of the annealing temperature for the V$_2$O$_{x(sol)}$ layer

It was revealed that the annealing temperature of the V$_2$O$_{x(sol)}$ layer was critical to achieve optimal performance. Figure 5.2(a) shows J-V curves and Figure 5.2(b) displays the key cell parameters for annealing of the layer between 50 and 140 °C for two minutes and also without annealing.

It was determined that annealing to 140 °C gave a considerably increased cell performance, enhanced from 0.10 % without annealing, to 2.31 %. Both *J$_{sc}$* and *FF* were greater and *R$_s$* was significantly improved. This gave an obvious indication of an inability to efficiently extract charges without or with annealing at low temperatures. This was unsurprising since the heat treatment allows for the removal of the isopropanol groups and residual solvent to form V$_2$O$_{x(sol)}$ layers. A small performance increase was facilitated by raising the annealing temperature from 110 to 140 °C, however additional studies indicated that heating to 250 °C gave no further benefit. Thus, an annealing step of 140 °C for 2 minutes was incorporated in to all further processing studies.
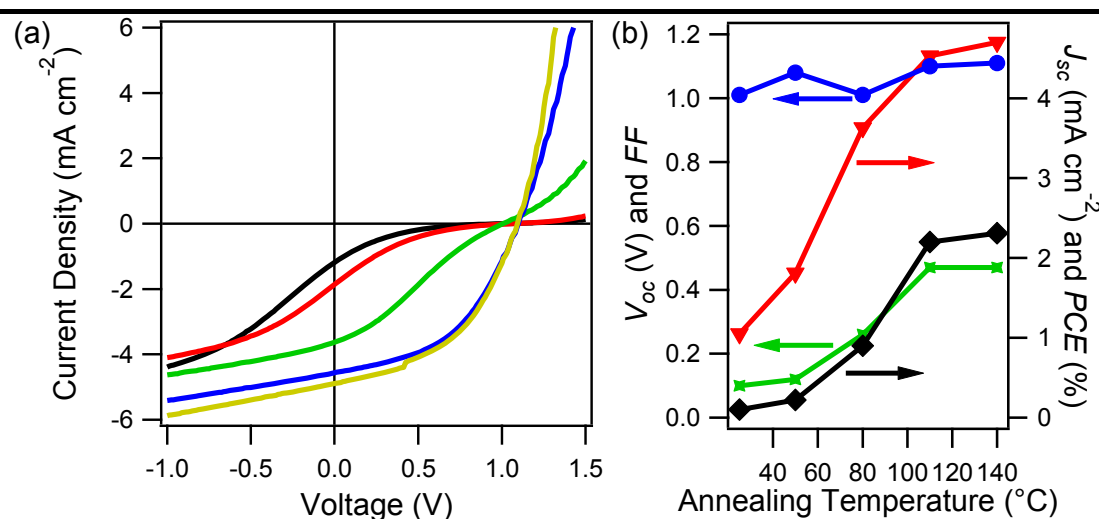
Figure 5.2: (a) *J-V* curves obtained under 1 sun illumination for cells with structure ITO / V$_2$O$_{x(sol)}$ / 14 nm SubPc / 40 nm C$_{60}$ / 8 nm BCP / Al, with no annealing (black line), 50 (red line), 80 (green line), 110 (blue line) and 140 °C (gold line) under N$_2$. (b) Variation of key cell parameters with annealing temperature (25 °C indicates no anneal), *J$_{sc}$* (red line), *V$_{oc}$* (blue line), *FF* (green line) and *η$_p$* (black line).

5.1.3 Atmospheric processing conditions of the $V_2O_{x(sol)}$ layers

The impact of the atmospheric conditions of layer preparation for both spin-coating and annealing steps were explored. Consequently, four variations of $V_2O_{x(sol)}$ were fabricated, with all combinations of spin-coating and annealing under ambient and N_2 atmospheres produced. The limited reports of $V_2O_{x(sol)}$ preparation in current literature focus on preparation of the layer in air,[194-196] despite the majority of organic photo-active layers requiring fabrication in inert atmospheres.

For consistency, all $V_2O_{x(sol)}$ layers were spin-coated at 3000 rpm and annealed at 140 °C, regardless of atmospheric conditions. 1 : 40 solutions of vanadium (V) oxytriisopropoxide : anhydrous IPA were mixed under a N_2 atmosphere, where the materials were stored between uses. Thin films spin-coated under a N_2 atmosphere were processed first, with the same solution transferred to ambient conditions for further layer fabrication.

To be concise, the four different layers distinguished by atmospheric conditions of processing are abbreviated here in the following way: layers spin-coated and annealed under N_2, $V_2O_{x(sol,N2,N2)}$; layers spin-coated under N_2 and annealed in air, $V_2O_{x(sol,N2,air)}$; layers spin-coated in air but annealed under N_2, $V_2O_{x(sol,air,N2)}$; and layers spin-coated and annealed in air, $V_2O_{x(sol,air,air)}$.

Figure 5.3(a) illustrates the contrast between $V_2O_{x(sol,air,air)}$ (left top and bottom) and $V_2O_{x(sol,N2,air)}$ (right top and bottom) layers. Two of each sample are shown to indicate the reproducible nature of this effect. When spin-coated in a N_2 atmosphere, the $V_2O_{x(sol,N2,N2)}$ and $V_2O_{x(sol,N2,air)}$ layers appeared highly transparent, with a slight yellow colour when viewed at certain angles. However, films processed in ambient conditions ($V_2O_{x(sol,air,air)}$ and $V_2O_{x(sol,air,N2)}$) have a drastically more

noticeable yellow colouration. Changes to the atmospheric conditions during annealing did not provide such significant differences.
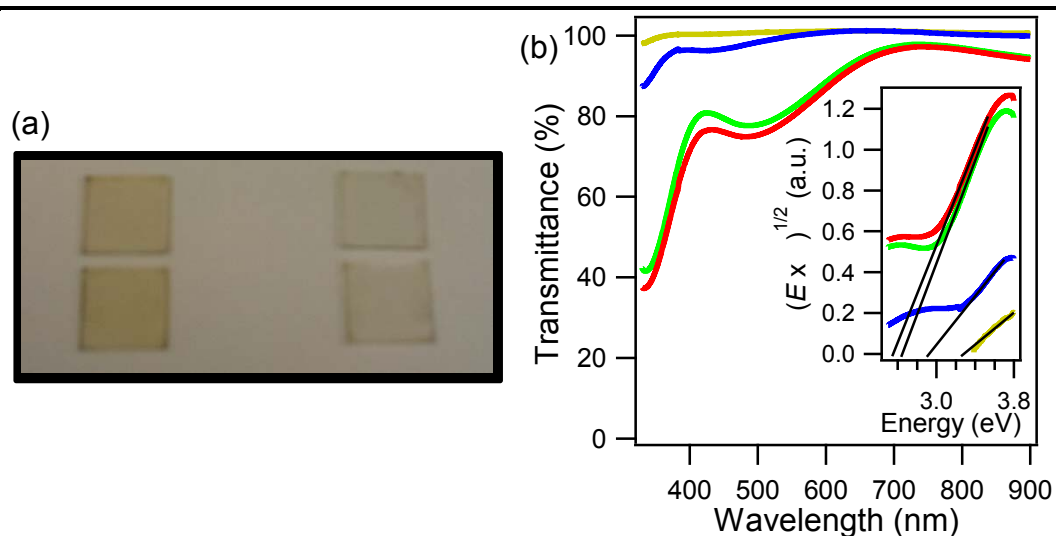
Figure 5.3: (a) Photograph of V$_2$O$_{x(sol,air,air)}$ layers (left) and V$_2$O$_{x(sol,N2,air)}$ layers (right), all on glass / ITO. (b) Transmittance of V$_2$O$_{x(sol,N2,N2)}$ (gold line), V$_2$O$_{x(sol,N2,air)}$ (blue line), V$_2$O$_{x(sol,air,N2)}$ (green line) and V$_2$O$_{x(sol,air,air)}$ (red line). Inset: plot of $(E \times \alpha)^{1/2}$ against energy for each V$_2$O$_{x(sol)}$ layer.

The transmittance data in Figure 5.3(b) highlights the stark contrast between processing conditions more rigorously. The layers spin-coated under N$_2$ have similar transmittance profiles, but with a slight decrease from V$_2$O$_{x(sol,N2,N2)}$ to V$_2$O$_{x(sol,N2,air)}$. Transmittance was above 97 % across the visible range, but below 400 nm the onset of the V$_2$O$_{x(sol)}$ absorption edge causes considerable reductions. The V$_2$O$_{x(sol,air,N2)}$ and V$_2$O$_{x(sol,air,air)}$ layers suffered an extensively reduced transmittance over the entire range. The overall profiles were similar for layers spun in air, but an additional small loss is encountered when annealing in ambient conditions. Both V$_2$O$_{x(sol,air,N2)}$ and V$_2$O$_{x(sol,air,air)}$ layers had reduced transmittance below 700 nm. A broad loss was

centred at 480 nm, with reductions of 22 and 25 % for $V_2O_{x(sol,air,N2)}$ and $V_2O_{x(sol,air,air)}$ films respectively.

Interestingly, the onset of the absorption edge was shifted to longer wavelengths with spin-coating in air. In order to estimate the band gap of the $V_2O_{x(sol)}$, a plot of $(E \times \alpha)^{1/2}$ against photon energy is presented in the inset of Figure 5.3(b), where α is absorbance, and E is energy in eV, as used for a MoO_x layer in Section 3.1.2. The estimation of the band gap of $V_2O_{x(sol)}$ varied with processing conditions. Layers spin-coated under N_2 have band gaps of 3.2 and 2.9 eV for the $V_2O_{x(sol,N2,N2)}$ and $V_2O_{x(sol,N2,air)}$ layers respectively. Spin-coating in ambient conditions produced smaller band gaps of 2.6 and 2.5 eV for $V_2O_{x(sol,air,N2)}$ and $V_2O_{x(sol,air,air)}$ films. The reduction of the $V_2O_{x(sol)}$ band gap with processing conditions suggested a possible change of layer stoichiometry.

XPS spectra for each layer are presented in Figure 5.4. The V2p peaks obtained exhibit clear asymmetry, with each V2p region composed of two distinct vanadium oxidation state species. Accordingly, the regions were fitted with a Lorentzian-Gaussian combination to find two separate peaks, consistent with previous literature reports.[195] Whilst each vanadium $2p_{3/2}$ and $2p_{1/2}$ peak invariably demonstrated asymmetry, the contribution of the lower binding energy shoulder varied with preparation conditions. Table 5.1 lists the binding energy for each peak in the $V2p_{3/2}$ region and the relative ratio of the major and minor vanadium oxidation states.
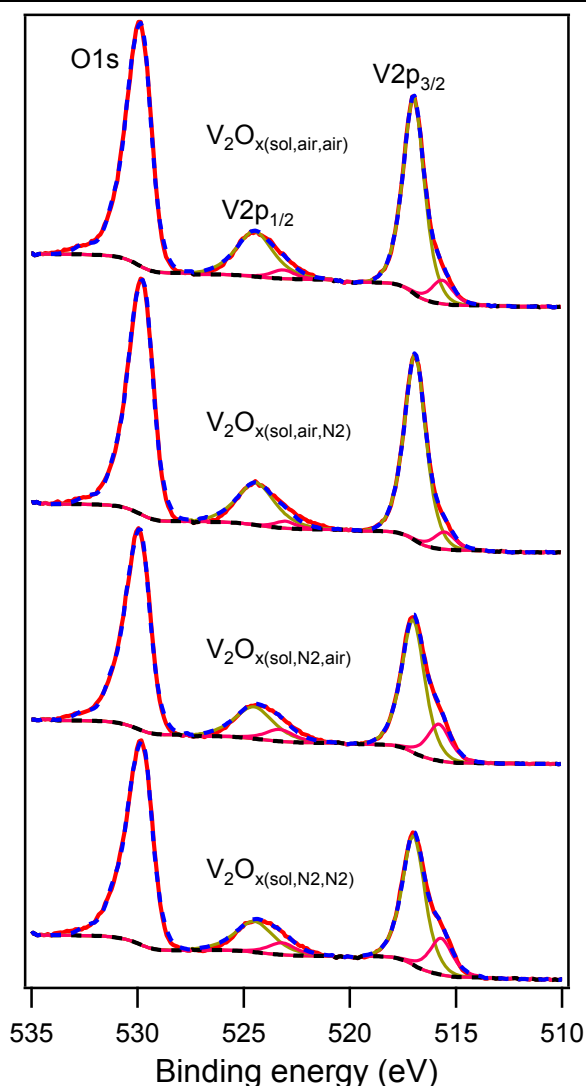
Figure 5.4: XPS spectra of the V2p and O1s region for the V$_2$O$_{x(sol)}$ layers processed under various conditions. Red lines indicate experimental data, dashed black lines the Shirley backgrounds, dashed blue lines the fitting envelope, with gold and pink lines representing the major and minor V^{5+} and V^{4+} contributions.

In each case, the binding energy was found to be 517.0 - 516.9 eV for the dominant vanadium oxidation state peaks. These values were consistent with numerous literature reports for V^{5+}, corresponding to V$_2$O$_5$.[189, 195, 197-199] The features between 1.2 - 1.4 eV lower in binding energy produce peaks centred at 515.8 - 515.5 eV. Binding energies of V^{4+}, due to VO$_2$, are commonly reported in this region.[189,]

[197-199] The films spin-coated in ambient conditions produced relative ratios of V^{5+} : V^{4+} of 8.3 : 1 and 10.8 : 1 for $V_2O_{x(sol,air,air)}$ and $V_2O_{x(sol,air,N2)}$ layers respectively. When spin-coated under N_2, there was a clearly reduced overall vanadium stoichiometry, verified by the noticeably more pronounced shoulders in the V2p region, from the V^{4+} oxidation state. Thus, the ratio of V^{5+} : V^{4+} was significantly lower with fabrication in N_2, with 3.5 : 1 and 3.6 : 1 for $V_2O_{x(sol,N2,N2)}$ to $V_2O_{x(sol,N2,air)}$ layers respectively.

Table 5.1: Summary of binding energy values for the V^{5+} and V^{4+} species in the $V2p_{3/2}$ region, with determined relative ratios of each under different $V_2O_{x(sol)}$ processing conditions.

Layer	V^{5+} peak binding energy (eV)	V^{4+} peak binding energy (eV)	Difference of binding energy (eV)	Ratio of V^{5+} : V^{4+}
$V_2O_{x(sol,N2,N2)}$	517.0	515.7	1.3	3.5:1
$V_2O_{x(sol,N2,air)}$	517.0	515.8	1.2	3.6:1
$V_2O_{x(sol,air,N2)}$	516.9	515.5	1.4	10.8:1
$V_2O_{x(sol,air,air)}$	517.0	515.6	1.4	8.3:1

The relative ratios of V^{5+} to V^{4+} with the variation of processing conditions of $V_2O_{x(sol)}$ convincingly correlate with the band gaps obtained from Figure 5.3. Previous literature reports have studied vanadium oxide layers with lithium and sodium intercalated into the oxide layers, modifying the structure and therefore optical properties of the oxides.[200, 201] The intercalation of Na and Li led to partial reductions of the originally stoichiometric V_2O_5 films, analogous to the substoichiometric $V_2O_{x(sol)}$ layers. In stoichiometric V_2O_5, the band gap arises due to the separation of the O2p valence band and the split V3d conduction band, thus

producing a band gap of ~ 2.3 eV. Talledo *et al.* indicated that the intercalation of Li resulted in a partial reduction of the vanadium oxide and consequently in the partial filling of the lower V3d band.[200] The increased occupation of this band and further reduction of disordered V$_2$O$_5$ occurred with additional Li content. Consequently, the reduction of the stoichiometric V$_2$O$_5$ resulted in a widening of the band gap from 2.25 to 3.10 eV for the substoichiometric layer. This change of band gap was convincingly rationalised by concluding that in stoichiometric V$_2$O$_5$ the optical gap is between the O2p valence band and the lower V3d split of the conduction band. However, with intercalation the lower V3d band is increasingly filled and therefore the band gap widens to be the difference from the O2p to the upper V3d band, with a significant difference of energy.[200] Wu *et al.* suggested an alternative reason for the change, with reduction of V^{5+} leading to a reduced orbital overlap of the O2p and V3d bands, increasing the optical band gap.[201]

Similar arguments for the change of V$_2$O$_5$ band gap can be applied here. The V$_2$O$_{x(sol)}$ layers spin-coated in air produced similar band gaps of 2.5 and 2.6 eV with annealing under ambient and N$_2$ conditions. These values present band gaps slightly wider than stoichiometric V$_2$O$_5$, due to the small quantity of V^{4+} present. With significantly increased V^{4+} content due to spin-coating under N$_2$, the V$_2$O$_{x(sol)}$ films fabricated according to this process have significantly increased band gaps of 2.9 and 3.2 eV, with annealing in air and N$_2$. Thus, analogous to the increased intercalation producing wider band gaps, the increased V^{4+} content also results in wider band gaps acting as a reduced species. Since hole-extracting layers benefit from enhanced transmittance across visible wavelengths, similar layer thicknesses but with increased oxygen deficiency in the V$_2$O$_{x(sol)}$ would be expected to facilitate the optimum transmittance for an OPV cell.

Although the change in band gap of V$_2$O$_{x(sol)}$ thin films can be attributed to stoichiometric changes, the reduced transmittance was also expected to correlate with layer thicknesses. The AFM step edge measurement in Figure 5.5 shows the V$_2$O$_{x(sol,N2,N2)}$ layer to be ~ 5.5 nm thick, whilst the V$_2$O$_{x(sol,air,air)}$ layer is ~ 18.2 nm thick (not shown). The additional features within the step edge are due to the partial removal of the V$_2$O$_{x(sol,N2,N2)}$ layer. When the layers are spin-coated in air, the solution is likely to undergo a hydrolysis reaction similar to other metal oxides.[35] This reaction increases the viscosity of the solution and consequently results in thicker layers than those fabricated under N$_2$ with the same spin-coating parameters.

Despite determining that the layers processed in air are ~ 3 times thicker than those produced under N$_2$, this alone cannot account for such a large loss in transmittance at shorter wavelengths. Thus, the combination of favourable stoichiometry, electronic properties, and fabrication of thinner layers under N$_2$ would suggest an increased suitability of the hole-extracting layers fabricated in this manner for inclusion in OPV cells.
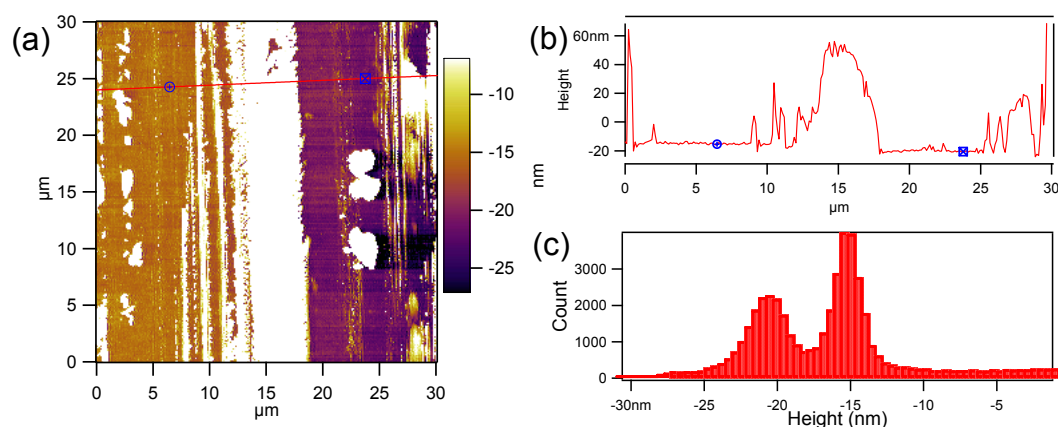
Figure 5.5: (a) 30 µm topographical AFM image of step edge area for V$_2$O$_{x(sol,N2,N2)}$ on ITO. (b) Cross section of image, represented by red line in (a). (c) Histogram of whole image.

The V$_2$O$_{x(sol)}$ films were incorporated into SubPc / C$_{60}$ discrete bilayer OPV cells, with *J-V* curves presented in Figure 5.6. Key cell parameters are stated in Table 5.2. As would be expected, J_{sc} decreased by 0.66 mA cm^{-2} when comparing fabrication on V$_2$O$_{x(sol,N2,N2)}$ to V$_2$O$_{x(sol,air,air)}$ layers due to the change in transmittance. This is further illustrated by the loss in current generation shown when comparing the *EQE* measurements for the cells deposited on V$_2$O$_{x(sol,N2,N2)}$ to V$_2$O$_{x(sol,air,air)}$ layers. It is also evident that fabrication on the V$_2$O$_{x(sol,N2,N2)}$ layer produced a favourable *FF* of 0.45 for the cell. The *FF* values are reduced to 0.41, 0.39 and 0.38 when cells are deposited onto V$_2$O$_{x(sol,air,N2)}$, V$_2$O$_{x(sol,N2,air)}$, and V$_2$O$_{x(sol,air,air)}$ layers respectively. The *J-V* curves in Figure 5.6 indicate an increased R_s to be the cause of the losses in *FF*. Due to the exposure of films to atmospheric conditions, it is likely that organic material and water is adsorbed onto the surface of the hole-extracting layer, causing this detrimental increase in R_s. This was seen to a greater extent with prolonged air exposure for MoO$_x$ layers in Section 3.1.5.

Table 5.2: Summary of cell performance parameters obtained with the architecture ITO / V$_2$O$_{x(sol)}$ / 14 nm SubPc / 40 nm C$_{60}$ / 8 nm BCP / Al, with V$_2$O$_{x(sol)}$ processed under stated conditions.

Layer	J_{sc} (mA cm^{-2})	V_{oc} (V)	*FF*	η_p (%)
V$_2$O$_{x(sol,N2,N2)}$	3.91 ± 0.10	1.12 ± 0.01	0.45 ± 0.03	2.11 ± 0.12
V$_2$O$_{x(sol,N2,air)}$	3.65 ± 0.06	1.12 ± 0.01	0.39 ± 0.04	1.67 ± 0.17
V$_2$O$_{x(sol,air,N2)}$	3.38 ± 0.01	1.10 ± 0.01	0.41 ± 0.01	1.61 ± 0.03
V$_2$O$_{x(sol,air,air)}$	3.25 ± 0.04	1.11 ± 0.01	0.38 ± 0.01	1.44 ± 0.04

The V_{oc} values seemed to be comparatively unaffected by the processing variations, with values from 1.10 to 1.12 V produced for the cells. The factors behind this were explored using KP measurements (under N$_2$). The V$_2$O$_{x(sol)}$ thin films produce remarkably similar work function values, with each in the range 5.6 ± 0.1 eV. Indeed, these work function values were expected to be large enough to cause Fermi level pinning of the SubPc layer, thus maximising the V_{bi} of each cell. This was similar to reports for thermally evaporated metal oxides, culminating in the large V_{oc} values obtained.
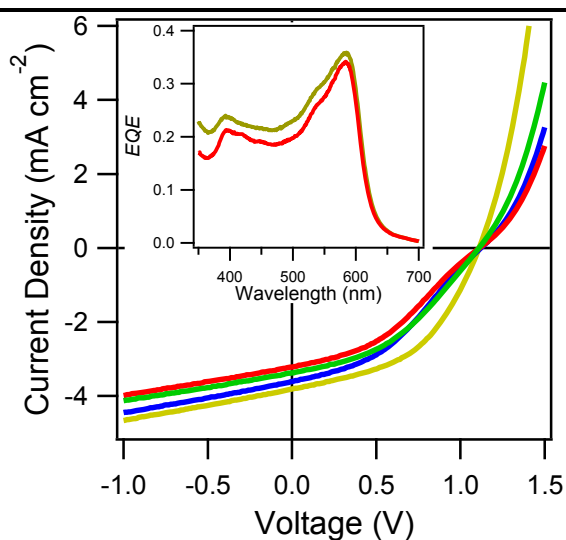
Figure 5.6: *J-V* curves obtained under 1 sun illumination for cells with structure ITO / V$_2$O$_{x(sol)}$ / 14 nm SubPc / 40 nm C$_{60}$ / 8 nm BCP / Al, with layers of V$_2$O$_{x(sol,N2,N2)}$ (gold line), V$_2$O$_{x(sol,N2,air)}$ (blue line), V$_2$O$_{x(sol,air,N2)}$ (green line) and V$_2$O$_{x(sol,air,air)}$ (red line) respectively. Inset: *EQE* measurement of the cells on top of V$_2$O$_{x(sol,N2,N2)}$ (gold line) and V$_2$O$_{x(sol,air,air)}$ (red line) hole extracting layers.

Despite the similar V_{oc} values achieved, the variation of J_{sc} and *FF* with V$_2$O$_{x(sol)}$ processing leads to distinct changes in η_p. The incorporation of V$_2$O$_{x(sol,N2,N2)}$ layers provided the highest η_p of 2.11 % due to improved transmittance

and *FF*. In direct comparison, cells fabricated on V$_2$O$_{x(sol,air,air)}$ layers only produced a η_p of 1.44 %. The > 30 % performance loss highlights the significant impact the processing conditions have on V$_2$O$_{x(sol)}$ layer properties. Thus, the optimal conditions presented here suggest V$_2$O$_{x(sol)}$ fabrication should be implemented under a N$_2$ atmosphere.

To ensure this trend was not only due to the thinner films prepared by film fabrication under N$_2$, comparably thick films of V$_2$O$_{x(sol)}$ were processed fully in air using a 1 : 80 volume ratio of Vanadium (V) oxytriisopropoxide : anhydrous IPA, spin coated at 6000 rpm before annealing at 140 °C for 2 minutes under ambient conditions. These layers were incorporated into SubPc / C$_{60}$ cells with the organic photo-active layers deposited onto V$_2$O$_{x(sol,N2,N2)}$ and the thin V$_2$O$_{x(sol,air,air)}$ simultaneously. *J-V* curves and *EQE* measurements for the cells are shown in Figure 5.7.
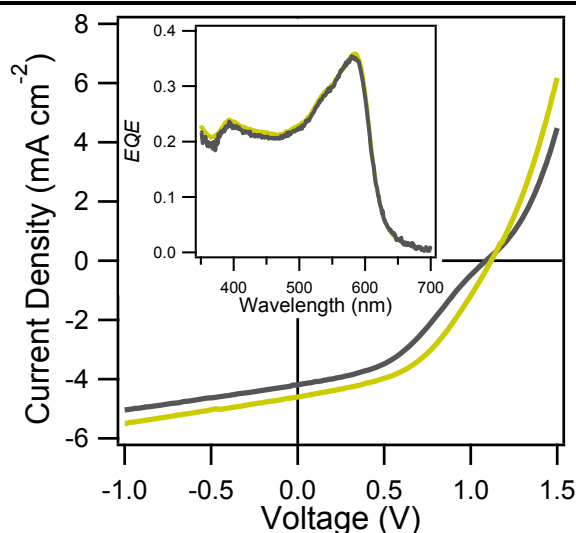
**Figure 5.7:** *J-V* curves obtained under 1 sun illumination for cells with structure ITO / V$_2$O$_{x(sol)}$ / 14 nm SubPc / 40 nm C$_{60}$ / 8 nm BCP / Al, with layers of V$_2$O$_{x(sol,N2,N2)}$ (gold line) and thin V$_2$O$_{x(sol,air,air)}$ layers (grey line). Inset: *EQE* measurement of the cells on top of V$_2$O$_{x(sol,N2,N2)}$ (gold line) and thin V$_2$O$_{x(sol,air,air)}$ (grey line) hole extracting layers.

The cells fabricated on the thin V$_2$O$_{x(sol,air,air)}$ layer gave an improved relative performance compared to those deposited on the standard V$_2$O$_{x(sol,air,air)}$ layers. The J_{sc} values for the cells on thin V$_2$O$_{x(sol,air,air)}$ layer were slightly lower (4.40 mA cm^{-2}) than on V$_2$O$_{x(sol,N2,N2)}$ (4.62 mA cm^{-2}). The *EQE* measurement shown in the inset of Figure 5.7 indicates a similar current generation for the cells at wavelengths above 500 nm, with loss of current generation below 500 nm on V$_2$O$_{x(sol,air,air)}$. This should be expected due to the smaller band gap for films prepared under ambient conditions. The cells fabricated on the V$_2$O$_{x(sol,air,air)}$ layer also suffer from an increased R_s, leading to a loss in *FF* from 0.45 on V$_2$O$_{x(sol,N2,N2)}$ to 0.42 on V$_2$O$_{x(sol,air,air)}$. Therefore cell η_p was lowered from 2.33 % on V$_2$O$_{x(sol,N2,N2)}$ to 2.04 % on thin V$_2$O$_{x(sol,air,air)}$ layers.

5.1.4 Position of the V$_2$O$_{x(sol)}$ valence band

The high work function of V$_2$O$_{x(sol,N2,N2)}$ measured by KP indicates the position of the Fermi level. Nevertheless, in order to determine whether V$_2$O$_{x(sol,N2,N2)}$ is n-type, UPS measurements were acquired. The valence band spectra and an energy level schematic of the optimised V$_2$O$_{x(sol,N2,N2)}$ are shown in Figure 5.8. The onset of the V$_2$O$_{x(sol,N2,N2)}$ valence band is seen to be 2.5 eV below the Fermi level of the layer. With a band gap estimated to be 3.2 eV in Section 5.1.3, this proved V$_2$O$_{x(sol,N2,N2)}$ to be highly n-type, as with thermally evaporated MoO$_x$ and V$_2$O$_x$.
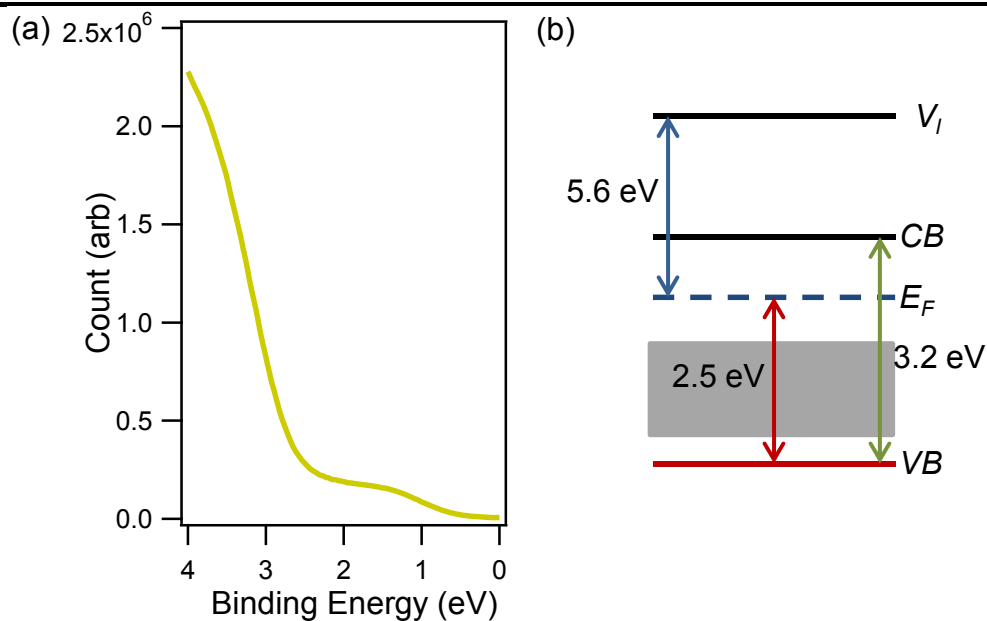
Figure 5.8: (a) Valence band UPS spectra for V$_2$O$_{x(sol,N2,N2)}$. (b) Energy level schematic of the optimised V$_2$O$_{x(sol,N2,N2)}$ constructed from UPS, KP and UV-vis absorption spectroscopy (gap states represented by grey box).

Additionally, gap states are displayed within the V$_2$O$_{x(sol,N2,N2)}$ band gap, between 0.5 - 2.5 eV below the V$_2$O$_{x(sol,N2,N2)}$ Fermi level. The presence of these additional states should be expected due to the substoichiometric nature of V$_2$O$_{x(sol,N2,N2)}$ exhibited in XPS measurements. Critically, this experimental evidence verified that V$_2$O$_{x(sol)}$ was able to behave in an analogous manner to the thermally evaporated metal oxides when used as a hole extracting layer.

5.2 Direct comparisons of optimised hole extracting materials

5.2.1 SubPc / C_{60} cells on 4 hole extracting surfaces

The obvious culmination of this work was to directly compare the previously optimised interfaces in OPV devices. This was implemented using both small molecule and polymer : fullerene photo-active layers. Here, SubPc / C_{60} photo-active layers were deposited on ITO, PEDOT : PSS, MoO_x and $V_2O_{x(sol,N2,N2)}$ to ensure that fair direct comparisons were made.
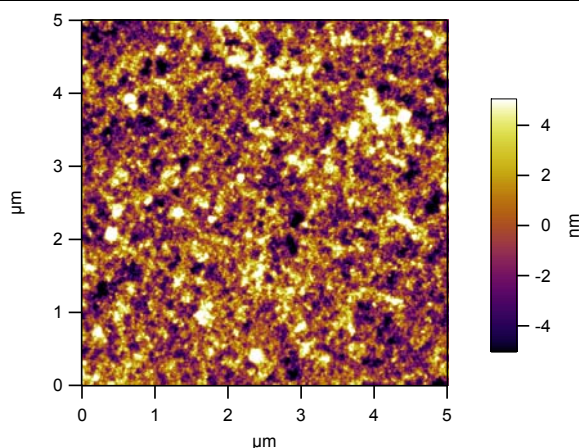
Figure 5.9: 5.0 μm AFM topographical image of ITO / PEDOT : PSS, height scale ± 5 nm.

PEDOT : PSS (Sigma-Aldrich, 1.3 wt % dispersion in H_2O, conductive grade) layers had previously been optimised by other members of the Jones group, and these parameters were used. The solution was filtered (0.45μm pore size) and spin-coated directly onto freshly UV ozone treated ITO at 6000 rpm. The layer was then annealed under ambient conditions at 120 °C for 20 minutes. This gave a layer thickness of ~ 25 nm, with the surface topography shown in Figure 5.9, producing an

R_q of 2.8 nm. MoO$_x$ and V$_2$O$_{x(sol)}$ were fabricated with the optimal parameters described in Sections 3.1.1 and 5.1.3.

Cells with the architecture ITO / (hole extracting layer) / 14 nm SubPc / 40 nm C$_{60}$ / 8 nm BCP / Al were fabricated, with *J-V* curves are displayed in Figure 5.10(a) and key cell parameters presented in Table 5.3.
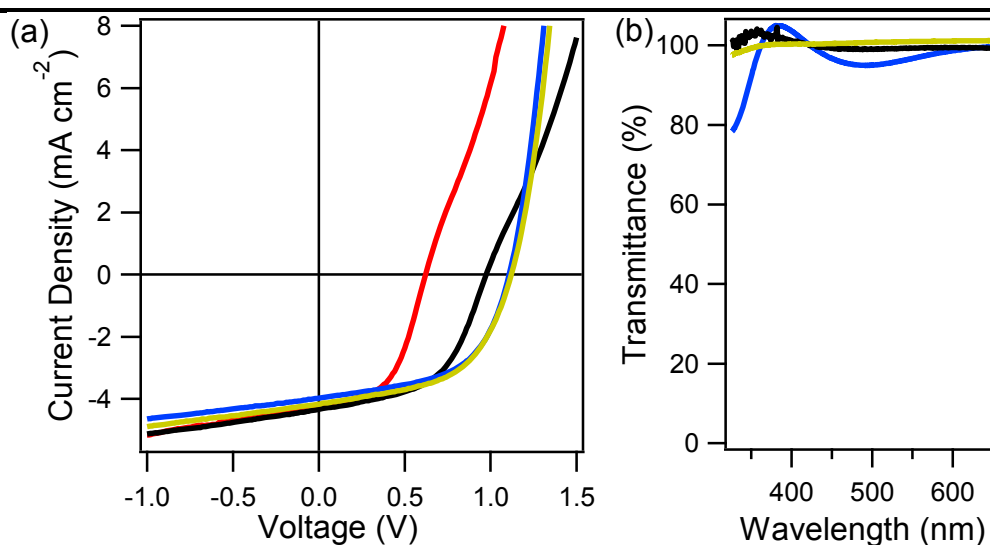
Figure 5.10: (a) *J-V* curves obtained under 1 sun illumination for cells with structure ITO / (hole extracting layer) / 14 nm SubPc / 40 nm C$_{60}$ / 8 nm BCP / Al, where the hole extracting layer was ITO (red line), PEDOT : PSS (black line), MoO$_x$ (blue line) and V$_2$O$_{x(sol,N2,N2)}$ (gold line). (b) Transmittance against ITO background for each hole extracting layer using the same colour coding.

The J_{sc} exhibited by the ITO, PEDOT : PSS and V$_2$O$_{x(sol,N2,N2)}$ based cells were similar with values of 4.24, 4.29 and 4.15 mA cm^{-2} respectively. This correlates well with the transmittance profiles of each layer taken against an ITO background in Figure 5.10(b). Whilst the V$_2$O$_{x(sol,N2,N2)}$ had a marginally preferential transmittance above 425 nm, PEDOT : PSS was more transparent below 425 nm. Accordingly, comparable J_{sc} values should be expected. MoO$_x$ had an equivalent

reduction in J_{sc} compared to ITO as that revealed in Section 3.2.1. This was consistent with the reduced transmittance demonstrated for MoO_x in Figure 5.10(b), when compared to the other interfaces. MoO_x based cells produce the highest *FF* value at 0.55, in comparison to 0.53, 0.53 and 0.52 for $V_2O_{x(sol,N2,N2)}$, PEDOT : PSS and ITO cells respectively. This was similar to the variation of cell parameters presented in Section 3.2.1.

Table 5.3: Summary of cell performance parameters obtained with the architecture ITO / (hole extracting layer) / 14 nm SubPc / 40 nm C_{60} / 8 nm BCP / Al.

Hole extracting layer	J_{sc} (mA cm^{-2})	V_{oc} (V)	*FF*	η_p (%)
ITO	4.24 ± 0.04	0.63 ± 0.01	0.52 ± 0.01	1.34 ± 0.05
PEDOT : PSS	4.29 ± 0.13	0.97 ± 0.01	0.53 ± 0.01	2.12 ± 0.06
MoO_x	3.98 ± 0.04	1.11 ± 0.01	0.55 ± 0.02	2.33 ± 0.04
$V_2O_{x(sol,N2,N2)}$	4.15 ± 0.05	1.12 ± 0.01	0.53 ± 0.01	2.38 ± 0.06

The most striking distinction between the interfaces was the variation of V_{oc}. Both metal oxide layers reveal remarkably high V_{oc} values, of 1.11 and 1.12 V for MoO_x and $V_2O_{x(sol,N2,N2)}$ respectively. PEDOT : PSS cells attained a V_{oc} of 0.97 V, with ITO cells only producing 0.63 V. It should be noted that the ITO substrates used in these experiments were obtained from a different manufacturer to those used in Section 3.2.1, hence the discrepancy from 0.79 to 0.63 V. KP measurements of the PEDOT : PSS surface revealed a work function of 5.3 eV, whilst the ITO work function was measured to be 4.7 eV. With cells containing the PEDOT : PSS layer producing V_{oc} values between that of the metal oxides and ITO, the hole extracting layer gave further evidence of the need for high work function hole extracting layers. The noticeable trend of V_{oc} with interface work function suggests the SubPc integer

charge transfer state resides between 5.3 and 5.5 eV. This can be assumed since a previous cell produced a V_{oc} of 1.10 V for a non optimised V$_2$O$_{x(sol)}$ layer possessing a work function of 5.5 eV as the cell V_{oc} was not maximised with the use of PEDOT : PSS due to a non optimal cell V_{bi}.

Accordingly, cell performance increased from ITO < PEDOT : PSS < MoO$_x$ < V$_2$O$_{x(sol,N2,N2)}$, with η_p values of 1.34, 2.12, 2.33 and 2.38 % respectively. Despite the relatively high J_{sc} values, the ITO and PEDOT : PSS cells showed a reduced η_p due to the losses in V_{oc}. With comparable V_{oc} values, MoO$_x$ and V$_2$O$_{x(sol,N2,N2)}$ were suitable hole extracting layers for SubPc / C$_{60}$ cells. A marginally higher η_p for the solution processed metal oxide is obtained due to the favourable transmittance.

5.2.2 P3HT : PCBM bulk heterojunction cells on 4 hole extracting surfaces

The purpose of developing V$_2$O$_{x(sol,N2,N2)}$ thin films was to provide an alternative to the commonly utilised PEDOT : PSS hole extracting layer. The latter is most commonly employed in polymer : fullerene bulk heterojunction blends, such as P3HT : PCBM. Consequently, in order to test the feasibility of replacing PEDOT : PSS with V$_2$O$_{x(sol)}$ P3HT : PCBM cells were fabricated. Thermally evaporated MoO$_x$ and bare ITO interfaces were also used for comparison.

The P3HT : PCBM system has been described as the workhorse of the polymer OPV community, due to relatively high efficiencies and availability from chemical manufacturers. Numerous reports have developed the systems processing conditions, explored fundamental properties of the blend and measured the impact of cell architecture on the system.[32-35] To minimise variations in cell performance the processing conditions in this report were kept constant throughout.

The hole extracting layers were processed as described in Section 5.2.1. Bulk heterojunction blends consisted of a 1 : 1 weight mixture of P3HT (Rieke, >98 % regioregular) : PCBM (Nano C, > 99 %), with 20 mg ml^{-1} of each dissolved in anhydrous 1,2-dichlorobenzene (Sigma-Aldrich, 99%). The solution was stirred for 48 hours at 40 °C in a N_2 atmosphere. This solution was filtered (0.2 µm pore size) and spin-coated on substrates at 800 rpm. After a drying period, the photo-active layers were thermally annealed at 140 °C for 20 minutes under N_2 and transferred into a vacuum evaporation chamber for deposition of 8 nm BCP and Al. The surface topography these layers form on ITO is shown in Figure 5.11, producing a surface R_q of 8.4 nm.
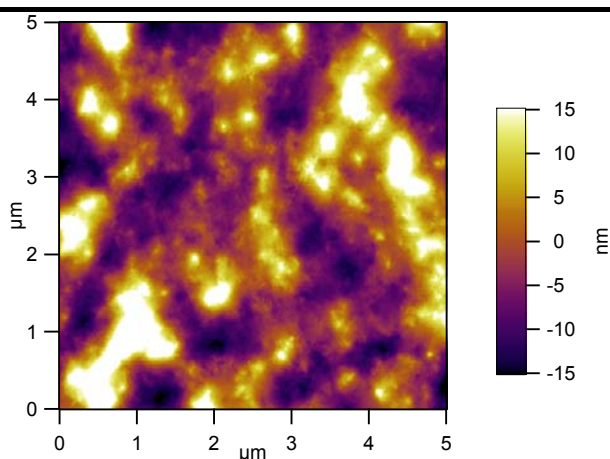
Figure 5.11: 5.0 µm AFM topographical image of ITO / P3HT : PCBM blend, height scale ± 15 nm.

Cells with the architecture ITO / (hole extracting layer) / P3HT : PCBM / 8 nm BCP / Al were fabricated (Figure 5.12(a)), with *J-V* curves in Figure 5.12(b) and key cell parameters presented in Table 5.4. The P3HT : PCBM photo-active layers deposited on bare ITO gave a poor η_p of 1.27 %. The most striking feature of Figure 5.12(b) is the drastically reduced V_{oc} of the ITO cells compared to the hole extracting

layers. With the work function of ITO measured to be 4.6 - 4.8 eV, the cells produce a V_{oc} of 0.33 V. In comparison PEDOT : PSS, $V_2O_{x(sol,N2,N2)}$ and MoO_x achieve comparable values of 0.61, 0.59 and 0.60 V, respectively. With the measured work function values of PEDOT : PSS (5.3 eV), $V_2O_{x(sol,N2,N2)}$ (5.6 eV) and MoO_x (6.4 eV) exceeding the P3HT ionisation potential (5.2 eV),[35, 64] these layers thus exceed the E_{ICT+} of P3HT and consequently maximise V_{oc}.[35] As with the SubPc / C_{60} cells, the smaller work function of ITO means that it does not exceed the P3HT E_{ICT+}, and accordingly produces a lower V_{oc}.
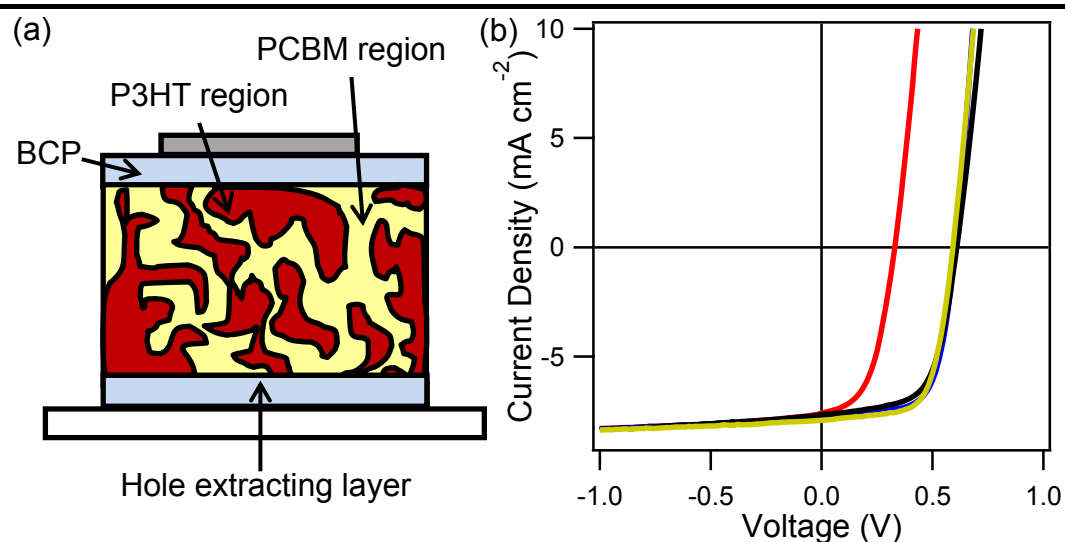
Figure 5.12: (a) Schematic representation of cell architecture. (b) *J-V* curves obtained under 1 sun illumination for cells with structure ITO / (hole extracting layer) / P3HT : PCBM / 8 nm BCP / Al, where the hole extracting layer is ITO (red line), PEDOT : PSS (black line), MoO_x (blue line) and $V_2O_{x(sol,N2,N2)}$ (gold line).

Cells fabricated on $V_2O_{x(sol,N2,N2)}$ and MoO_x layers obtained remarkable *FF* values of 0.65 and 0.67. The PEDOT : PSS cells had a marginally lower *FF* of 0.62 due to a slight increase in R_s. ITO cells suffered from a significantly reduced *FF* of 0.48 in comparison. In the bulk heterojunction cells, the compromised V_{bi} due to the

low work function of the ITO had a larger impact on *FF* and *V$_{oc}$*. Initial literature studies found that the *V$_{oc}$* produced by bulk heterojunction polymer : fullerene cells was directly dependent on the difference of work function between the respective electrode materials.[59, 62] It has been shown since that the *V$_{oc}$* is in fact limited to the effective band gap at the D / A interface, but losses in *V$_{bi}$* are the cause of potential losses in *V$_{oc}$* in such systems.[49, 136, 137]

Table 5.4: Summary of cell performance parameters obtained with the architecture ITO / (hole extracting layer) / P3HT : PCBM / 8 nm BCP / Al.

Hole extracting layer	J_{sc} (mA cm^{-2})	V_{oc} (V)	*FF*	η_p (%)
ITO	7.60 ± 0.05	0.33 ± 0.01	0.48 ± 0.03	1.27 ± 0.09
PEDOT : PSS	7.84 ± 0.68	0.61 ± 0.00	0.62 ± 0.01	3.17 ± 0.27
MoO$_x$	7.73 ± 0.36	0.60 ± 0.00	0.67 ± 0.01	3.31 ± 0.13
V$_2$O$_{x(sol,N2,N2)}$	8.13 ± 0.34	0.59 ± 0.01	0.65 ± 0.01	3.34 ± 0.12

The PEDOT : PSS and V$_2$O$_{x(sol,N2,N2)}$ cells achieve *J$_{sc}$* values of 7.84 and 8.13 mA cm^{-2} respectively. The blend deposited on MoO$_x$ produced a slightly reduced *J$_{sc}$* of 7.73 mA cm^{-2}. Whilst this was lower than the solution processed metal oxide, the difference was shown to be due to transmittance, as with SubPc / C$_{60}$. This was evident in the *EQE* and transmittance profiles presented for each in Figure 5.13, clearly indicating the increased current generation for V$_2$O$_{x(sol)}$ cells, in particular between 425 - 575 nm. The integration of the *EQE* data between 350 - 750 nm indicates a *J$_{sc}$* of 7.13 and 7.31 mA cm^{-2} was produced with the MoO$_x$ and V$_2$O$_{x(sol,N2,N2)}$ layers respectively. Further small *J$_{sc}$* gains should also be expected with the V$_2$O$_{x(sol,N2,N2)}$ layer below 350 nm.
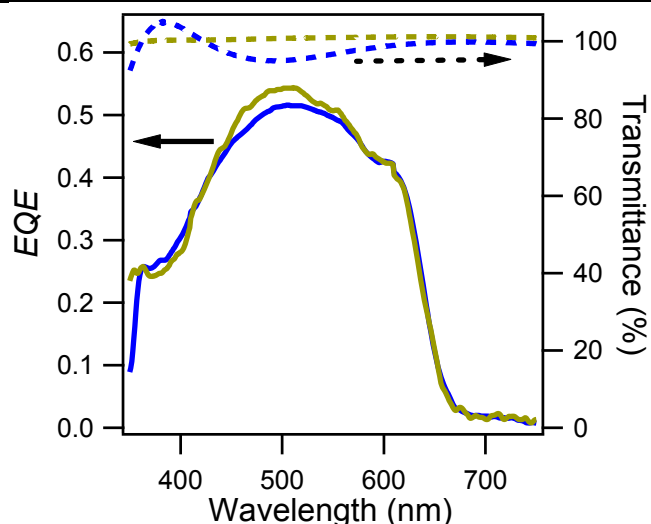
Figure 5.13: *EQE* for ITO / (hole extracting layer) / P3HT : PCBM / 8 nm BCP / Al, where the hole extracting layer is MoO$_x$ (blue line) and V$_2$O$_{x(sol,N2,N2)}$ (gold line). Transmittance data for the hole extracting layers (dotted lines).

P3HT : PCBM cells generate comparable η_p values of 3.17, 3.34 and 3.31 % with the incorporation of PEDOT : PSS, V$_2$O$_{x(sol,N2,N2)}$ and MoO$_x$ hole extracting layers respectively. These performance values highlight both the importance of the hole extracting layers to achieve relatively high efficiencies, and in addition suggest the V$_2$O$_{x(sol,N2,N2)}$ layer has potential as a solution processed alternative to PEDOT : PSS for polymer : fullerene cells.

5.2.3 P3HT : PCBM cell stability measurements

Whilst high initial cell performances are important for highlighting the maximum potential of a system, cell stability is an equally important factor to consider in OPV cell commercialisation. Section 3.2.5 focused on the impact the thermally evaporated MoO$_x$ layer has on the stability of a small molecule bilayer OPV cell compared to ITO. Here, the P3HT : PCBM system was tested over an hour of constant illumination for each of the four interfaces.

Figure 5.14 shows the stability of the key cell parameters for each hole extracting layer. After an hour of constant illumination, only 59 % of the original η_p was retained for the P3HT : PCBM cell deposited on bare ITO. This was due to a substantial loss of V_{oc} (26 % loss), a reduction of J_{sc} by 13 % and *FF* by 7 %. Cell fabrication on PEDOT : PSS suffered a performance reduction to 68 % of the original cell η_p, revealing losses of 19, 14 and 3 % in V_{oc}, J_{sc} and *FF* respectively. Cell stability was greatly improved on both metal oxide layers, with 89 and 94 % of the starting performance retained for cell fabrication on $V_2O_{x(sol,N2,N2)}$ and MoO_x layers. This indicates the enhanced V_{oc} stability of the metal oxides compared to ITO and PEDOT : PSS, with only 4 % and 3 % reductions for $V_2O_{x(sol,N2,N2)}$ and MoO_x. This, in addition to small losses of 8 % and 4 % of J_{sc} and a 0 % and 1 % loss of *FF* with $V_2O_{x(sol)}$ and MoO_x layers, illustrates the substantially improved stability of the cell integrating the metal oxide interface rather than the more commonly used bare ITO and PEDOT : PSS.
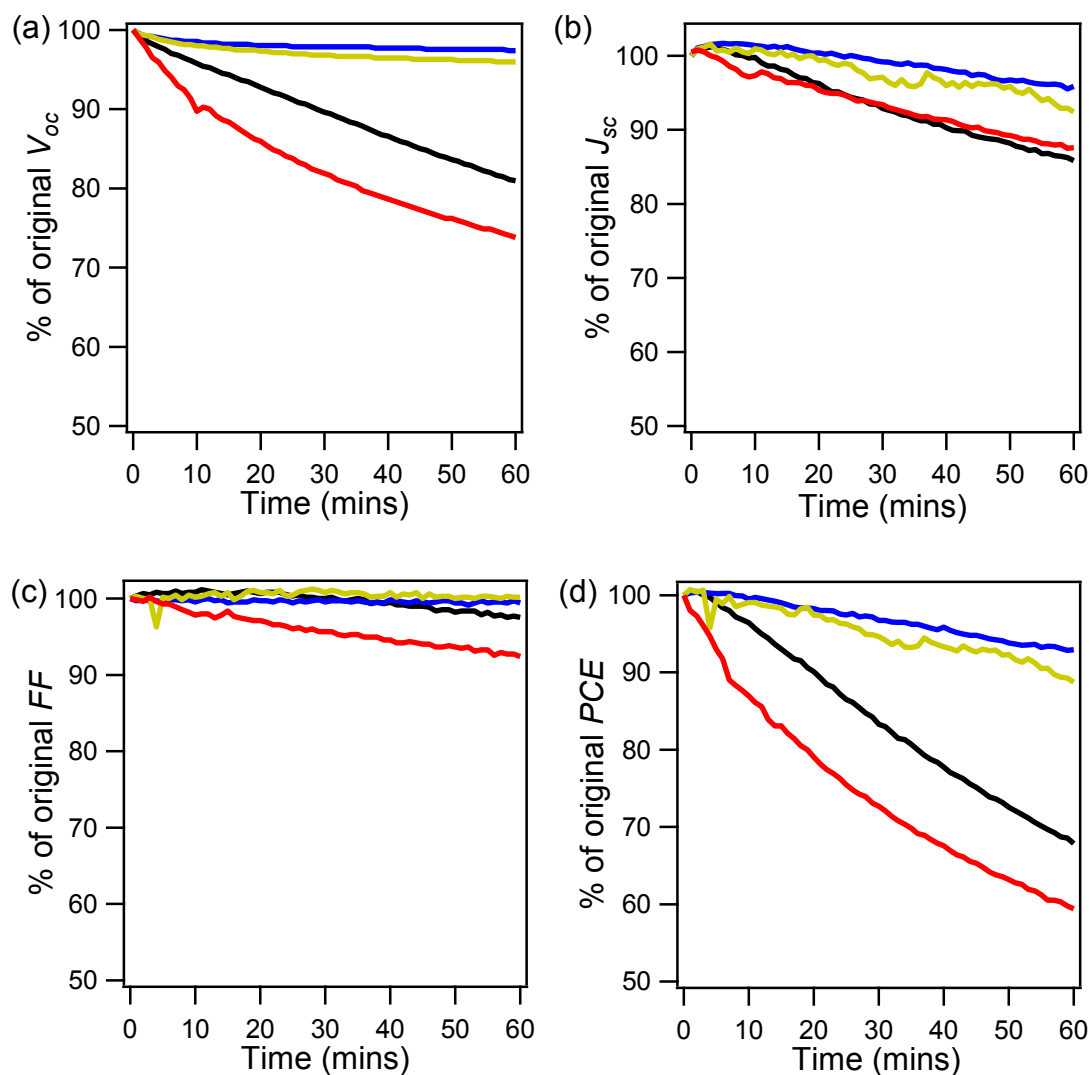
Figure 5.14: Stability of key cell performance parameters over 60 minutes constant illumination under an N_2 atmosphere for the P3HT : PCBM system on each hole extracting layer, where (a) V_{oc}, (b) J_{sc}, (c) FF, (d) η_p and hole extracting layers are ITO (red line), PEDOT : PSS (black line), MoO_x (blue line) and $V_2O_{x(sol,N2,N2)}$ (gold line).

In Section 3.2.5 the EQE data for a SubPc cell fabricated on MoO_x was shown to produce smaller losses across both donor and acceptor regions of current generation compared to the cell deposited on ITO. In order to determine if the same is true for a P3HT : PCBM cell deposited on $V_2O_{x(sol,N2,N2)}$ EQE measurements were taken before and after the 60 minute constant illumination tests, presented in Figure

5.15. The *EQE* profiles demonstrate that the reduction of current occurs equally across donor and acceptor regions of the blend when deposited on both the ITO and V$_2$O$_{x(sol,N2,N2)}$ surfaces. This broad loss is explicitly highlighted in Figure 5.15(c). The smaller loss in the *EQE* profile of the V$_2$O$_{x(sol,N2,N2)}$ complements the *J-V* degradation measurements, with V$_2$O$_{x(sol)}$ providing lower *J$_{sc}$* losses for the cells compared to ITO.
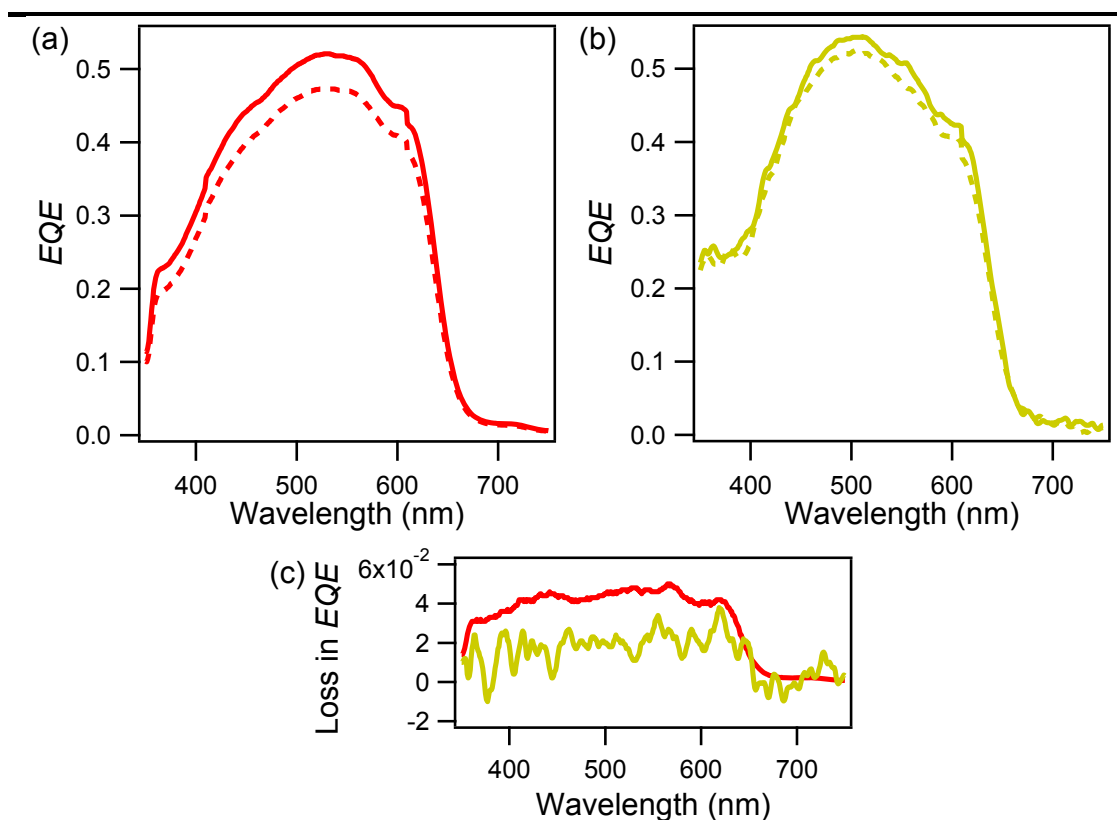
Figure 5.15: *EQE* data measured before (solid lines) and after (dashed lines) stability tests under 60 minutes constant illumination under an N$_2$ atmosphere for P3HT : PCBM OPV cells fabricated on (a) ITO and (b) V$_2$O$_{x(sol,N2,N2)}$. (c) indicates the loss in *EQE* for ITO (red line) and V$_2$O$_{x(sol,N2,N2)}$ (gold line).

The enhanced cell stability due to the V$_2$O$_{x(sol,N2,N2)}$ layer provided a further persuasive reason for the inclusion of the metal oxide in polymer : fullerene blend

cells. The stability measured for $V_2O_{x(sol,N2,N2)}$ was only marginally lower than that of the thermally evaporated MoO_x layer (11 % and 6 % losses overall respectively) and a considerable improvement over bare ITO and PEDOT : PSS, with losses of 41 % and 32 % repsectively. Thus, the beneficial stability and similar initial performance reveal the $V_2O_{x(sol,N2,N2)}$ film as a preferential solution processed hole extracting layer compared to PEDOT : PSS layer in this system.

5.3 Conclusion

The processing conditions for $V_2O_{x(sol)}$ were optimised, with the requirement of a short, relatively low temperature annealing step. The atmospheric conditions of fabrication of the $V_2O_{x(sol)}$ layer were shown to be vitally important in order to achieve high performances for OPV cells. When spin-coated in air, the band gap of the $V_2O_{x(sol)}$ was reduced, resulting in a yellow discolouration of the films. This negatively impacted on the J_{sc} of the cells due to the loss of transmittance. The variation of processing conditions led to changes of $V_2O_{x(sol)}$ stoichiometry, elucidated using XPS. $V_2O_{x(sol,N2,N2)}$ and $V_2O_{x(sol,N2,air)}$ layers were found to contain a reduced overall vanadium stoichiometry compared to $V_2O_{x(sol,air,air)}$ and $V_2O_{x(sol,air,N2)}$ layers. The spin-coating and annealing of the hole extracting layer under a N_2 atmosphere produced the most favourable results.

The N_2 processing resulted in a 5.5 nm thick $V_2O_{x(sol,N2,N2)}$ layer with a high work function of 5.6 eV. $V_2O_{x(sol,N2,N2)}$ demonstrates n-type character, with the oxygen deficiencies revealed by XPS accounting for the additional states seen in the valence band UPS spectra. This showed the $V_2O_{x(sol,N2,N2)}$ to be analogous to the thermally evaporated MoO_x and V_2O_x layers in terms of its impact on the performance of OPV cells.

Since the $V_2O_{x(sol,N2,N2)}$ offers a potential solution processed alternative to the thermally evaporated metal oxide layers, direct comparisons with MoO_x, ITO and the commonly used PEDOT : PSS were obtained for OPV devices. SubPc / C_{60} cells achieved performances of 2.33 and 2.38 % on MoO_x and $V_2O_{x(sol,N2,N2)}$ respectively. $V_2O_{x(sol,N2,N2)}$ obtained a marginally higher performance due to the favourable transmittance of the layer. Cells fabricated on PEDOT : PSS produced a η_p of 2.11 % and despite a marginally improved J_{sc} and a comparable FF to the metal oxides, a lower V_{oc} of 0.97 V resulted in the lower performance. With a measured work function of 5.3 eV, the V_{oc} of the cells deposited onto PEDOT : PSS was between that of those on ITO (work function 4.6 - 4.8 eV, $V_{oc} = 0.63$ V) and the metal oxides (work functions of 5.6, 6.4 eV, V_{oc} of 1.12, 1.11 V for $V_2O_{x(sol,N2,N2)}$, MoO_x respectively), due to the high ionisation potential of the donor.

Since $V_2O_{x(sol,N2,N2)}$ offered the ability to solution process a high work function metal oxide, the compatibility of the layer with solution processed bulk heterojunction P3HT : PCBM photo-active layers was investigated. The cell η_p of 3.34 % compellingly indicated $V_2O_{x(sol,N2,N2)}$ was a viable alternative to PEDOT : PSS, which achieved an η_p of 3.17 %. Thermally evaporated MoO_x offers a further option as a hole extracting layer for the system, obtaining an η_p of 3.31 %. Consequently, the cells fabricated on each interface were subjected to a stability test of 60 minutes constant illumination. The metal oxides showed a remarkable stability in comparison to PEDOT : PSS and ITO, with the solution processed $V_2O_{x(sol,N2,N2)}$ layer only marginally less stable than the MoO_x.

An advantage of the $V_2O_{x(sol,N2,N2)}$ layer was the ability to fabricate the hole extracting layer in an atmosphere suitable for the photo-active materials. From the integration of $V_2O_{x(sol,N2,N2)}$ layers in polymer : fullerene cells, future incorporation

into a variety of architectures of high ionisation potential polymer systems should be successful. Indeed, the layer can be expected to outperform PEDOT : PSS when used with the higher ionisation potential donor polymers, as demonstrated with the SubPc / C$_{60}$ small molecule OPV cells.

Chapter 6: Conclusions

The use of a hole extracting layer is vital to maximise the performance of OPV cells, providing an optimised contact. In this work metal oxide layers have been demonstrated to improve cell performance and stability. The three chapters have each explored the use of a different metal oxide hole extracting layer:

- Molybdenum oxide was utilised as a hole extracting layer with bilayer systems containing both high and low ionisation potential donor materials.

- Thermally evaporated vanadium oxide was determined to have wide band gap n-type characteristics and was suitable for use as a hole extracting layer.

- A method of solution processing vanadium oxide was optimised, obtaining similar cell performance to the thermally evaporated metal oxides.

6.1 The impact of a MoO_x hole extracting layer on OPV cells

The layer thickness of thermally evaporated MoO_x was varied between 2.5 - 50 nm with the optimum layer thickness determined to be 5 nm for a ClAlPc / C_{60} system. The η_p of the ClAlPc / C_{60} cells increased from 1.65 % on bare ITO to 2.60 % with the 5 nm MoO_x layer, primarily due to an enhancement in V_{oc} from 0.51 V to 0.82 V. The MoO_x layer was also used with another high ionisation potential donor material in SubPc / C_{60} cells. When utilised in this system, the cells containing MoO_x achieved a similar enhancement of cell performance with a η_p of 1.85 % on ITO and 2.53 % on MoO_x. The main cause of the performance enhancement was an increase in V_{oc} from 0.79 V on ITO to 1.08 V on the MoO_x layer.

However, when using the MoO_x layer in cells containing low ionisation potential donor materials there was a slight reduction in performance. A η_p of 1.11 % was achieved for the CuPc / C_{60} cells on ITO, with a η_p of only 1.03 % on the MoO_x layer. A similar trend was encountered for pentacene / C_{60} cells, achieving a η_p of 1.38 % on ITO and 1.24 % on MoO_x. In both systems the V_{oc} of the cells was comparable on both ITO and MoO_x, with small losses in J_{sc} attributed to the reduced transmittance of the metal oxide.

Studies of the organic layers using XRD, AFM and UV-vis absorption spectroscopy did not indicate noticeable changes to the structure or morphology of the donor layers with the insertion of the MoO_x, with changes to cell performance primarily due to the electronic properties of the MoO_x layer. Rather than the previously reported p-type behaviour, MoO_x layers exhibited n-type characteristics when measured *in-situ* using UPS, with the layer possessing a high work function value of 6.4 eV. The valence band onset resided 2.7 eV below the Fermi level of the metal oxide, resulting in an ionisation potential of 9.1 eV for the MoO_x layer. The MoO_x band gap was found to be 3.4 eV with additional features shown within the band gap close to the Fermi level due to the substoichiometric character of the layer, referred to as gap states.

Sequential thin film ClAlPc deposition and *in-situ* UPS characterisation indicated that the organic was pinned to the Fermi level of the MoO_x, exhibiting significant band bending. A dipole was formed between MoO_x and ClAlPc due to the difference in work function. The cells containing high ionisation potential donors suffered smaller reductions in V_{bi} with the insertion of the MoO_x, resulting in increased V_{oc} and therefore higher η_p. For the cells employing lower ionisation potential donor materials the ITO work function was large enough to avoid

compromising the V_{bi} of the cell and therefore the systems produced no increase of cell performance with MoO_x insertion.

The stability of the cells increased under both operational conditions and for shelf life tests with the inclusion of the MoO_x layer. A rapid loss of performance under constant illumination was revealed for cells deposited on ITO, retaining only 6 % of the original cell performance after 24 hours. When MoO_x was used 62 % of the original cell performance was retained in the same time period. The T80 shelf life time of cells deposited onto ITO was shown to be 33.8 days, whereas T80 was extrapolated to 106 days on the MoO_x surface. Despite the marginally lower overall cell performance for CuPc / C_{60} and pentacene / C_{60} cells, the systems benefited from the increased stability exhibited on MoO_x.

6.2 Use of a thermally evaporated V_2O_x layer in OPV cells

Thermally evaporated layers of V_2O_x were used as hole extracting films in OPV cells. A 5 nm layer thickness gave optimal cell performance enhancing the η_p of SubPc / C_{60} cells from 1.98 % on ITO to 2.50 %. The improved performance was due to an increase of V_{oc} from 0.81 V on ITO to 1.10 V on the V_2O_x layer. For the CuPc / C_{60} system the overall cell performance was reduced from 1.07 % on ITO to 0.93 % on the V_2O_x layer. Obvious parallels can be drawn between the results obtained for the same cell structures on the MoO_x layer compared to bare ITO.

The electronic characteristics of the V_2O_x layer were measured *in-situ* using UPS with the metal oxide exhibiting a large work function of 6.8 eV and an ionisation potential of 9.3 eV. A band gap of 2.9 eV was measured for V_2O_x,

indicating that the conduction band resided 0.4 eV above the Fermi level for the layer. Consequently, V_2O_x was found to be n-type with similar electronic characteristics to the MoO_x layer, despite previous reports of a low work function value and p-type properties. The additional gap states displayed within the MoO_x band gap were also exhibited by the V_2O_x film. Since the position of the valence band would create a barrier for hole extraction it was tentatively proposed that hole transport could be facilitated through these additional states.

Systematic studies were carried out to determine the electronic structure of SubPc and CuPc thin films deposited *in-situ* on to the ITO and V_2O_x surfaces. The high work function of the V_2O_x layer pinned each organic material to the Fermi level of the metal oxide. This was expected to maximise the V_{bi} of the cells for each system deposited on the V_2O_x layer. The deposition of SubPc onto ITO resulted in a large energy offset between the Fermi level of the electrode and the HOMO level of the organic layer, causing the V_{bi} reduction for the cells. For the CuPc thin films on ITO a slight pinning of the organic to the Fermi level of the electrode was shown, despite obtaining a smaller work function value than that revealed for the freshly cleaned and transferred ITO samples measured by KP and used in cell growth. Accordingly, a large increase in V_{oc} was seen with V_2O_x insertion for the SubPc / C_{60} system, but not for the CuPc / C_{60} system. Therefore, the V_2O_x layer could be used as a direct alternative to the MoO_x hole extracting layer.

6.3 A solution processed V_2O_x hole extracting layer in OPV cells

Solution processed thin films of V_2O_x were prepared for use as hole extracting layers in OPV cells. The spin-coating speed and subsequent annealing step

of the $V_2O_{x(sol)}$ layers were optimised for SubPc / C_{60} cells. Layer fabrication was carried out under a N_2 atmosphere and in ambient conditions and the effect of the atmospheric conditions on the $V_2O_{x(sol)}$ layer were characterised and tested in cells. When spin-coated in air the layer exhibited a yellow discolouration that was not present when spun under N_2, due to the band gap and transmittance profile of the metal oxide layer varying with fabrication conditions. A wider band gap and more favourable transmittance profiles were demonstrated for $V_2O_{x(sol,N2,N2)}$ and $V_2O_{x(sol,N2,air)}$ layers. XPS studies indicated that layers spin-coated under N_2 displayed an increase of V^{4+} content compared to layers prepared in ambient conditions. Therefore, the stoichiometric composition directly influenced the size of the band gap for the $V_2O_{x(sol)}$ layers.

SubPc / C_{60} cells were fabricated for each of the preparation conditions of $V_2O_{x(sol)}$. The cell η_p was greatest on the $V_2O_{x(sol,N2,N2)}$ layer, producing 2.11 %. The layer with the lowest η_p was $V_2O_{x(sol,air,air)}$ which gave a similar V_{oc} but lower J_{sc} and *FF* values. The optimised $V_2O_{x(sol,N2,N2)}$ layer thickness was measured to be 5.5 nm. The electronic characterisation of the $V_2O_{x(sol,N2,N2)}$ layer revealed a work function of 5.6 eV, with an ionisation potential of 8.1 eV. The layer was confirmed to be n-type with a band gap of 3.2 eV. The additional gap states present within the $V_2O_{x(sol,N2,N2)}$ band gap were due to the presence of the V^{4+} oxidation state, shown by XPS.

Both SubPc / C_{60} and P3HT : PCBM OPV cells were fabricated to allow direct performance comparison of thermally evaporated MoO_x, solution processed PEDOT : PSS and bare ITO to the $V_2O_{x(sol,N2,N2)}$ hole extracting layer. $V_2O_{x(sol,N2,N2)}$ and MoO_x provided the highest η_p values for the SubPc / C_{60} cells, at 2.38 and 2.33 % respectively. The η_p was reduced to 2.11 % for the cells containing the PEDOT : PSS layer, due to a reduction in V_{oc} from $\sim$ 1.11 V on the metal oxide layers to 0.97

V. ITO suffered a larger reduction in V_{oc}, culminating in a η_p of 1.34 %. The trend for V_{oc} was described by the *ICT* model with the layers possessing a larger work function value producing the higher V_{oc} values.

P3HT : PCBM cells incorporating the MoO_x, $V_2O_{x(sol,N2,N2)}$ and PEDOT : PSS layers obtained similar η_p values, with efficiencies of 3.31, 3.34 and 3.17 % respectively. Cells containing each layer also produced a similar V_{oc} value. ITO suffered a compromised cell performance mainly due to a reduction in V_{oc}. The P3HT : PCBM cells deposited onto the metal oxide layers demonstrated a significantly higher stability under an hour of constant illumination. PEDOT : PSS and ITO both encountered a significant reduction to cell performance under identical test conditions.

Consequently, $V_2O_{x(sol,N2,N2)}$ hole extracting layers exhibited an analogous performance to the thermally evaporated metal oxide layers in both small molecule / fullerene and polymer : fullerene cells. When used in combination with a high ionisation potential donor material, the $V_2O_{x(sol,N2,N2)}$ layer achieved a greater performance than the commonly used PEDOT : PSS. In P3HT : PCBM cells the initial cell performance was similar on both layers but the metal oxide displayed improved operational stability. As a result, the $V_2O_{x(sol,N2,N2)}$ layer was an excellent alternative to both thermally evaporated metal oxides and PEDOT : PSS.

Chapter 7: Future work

This work has shown how substoichiometric n-type metal oxide hole extracting layers can be used to improve the performance of an OPV cell compared to bare ITO electrodes. However, the hole extraction process is not fully understood for the metal oxides since transport through the valence band of the layers is energetically unfavourable. Therefore, further experiments could be carried out using a technique such as pulsed laser deposition to fabricate both stoichiometric and various compositional ratios of substoichiometric metal oxide layers to help clarify if the additional gap states are required for hole transport. All samples would need to be characterised by UPS, XPS and UV-vis absorption spectroscopy in order to reveal the electronic properties and composition of the layers. These layers can then be used in cell fabrication with high ionisation potential donor systems to allow direct comparisons between different layer stoichiometry. Additional work should include the fabrication of higher work function solution processed metal oxide layers than those presented here. This would facilitate the use of solution processed hole extracting layers with future higher ionisation potential donors.

The operational and shelf life stability of cells was shown to be improved with the insertion of the metal oxide layers in short term studies. However, long term OPV cell stability measurements are crucial and need to be designed to indicate the potential of cell commercialisation. This would require testing facilities that can measure stability over months rather than days and under various conditions, such as indoor and outdoor testing with variation of humidity and cell temperature. A method of inexpensive cell encapsulation is also needed. In order to reduce

performance losses, experiments are essential to further the understanding of the complex processes taking place during cell degradation. These could include degradation tests on cells exposed to isotopic labelled oxygen and water. Characterisation by techniques such as secondary ion mass spectroscopy would help to determine which layers in the OPV cell are most susceptible to degradation. By understanding the processes that are detrimental to cell stability we may be able to eliminate or minimise their contribution and hence improve cell lifetimes.

The factors behind the increase of cell performance in the first few minutes of testing the inverted SubPc / C_{60} structure on the BCP are not understood. However, these cells were fabricated to show inverted architectures are decoupled from the work function of the electrode materials when using interlayers. Inverted cell architectures are of interest as they open the possibility of using alternative electron extracting layers to BCP, such as the wide band gap metal oxides ZnO and TiO_x. These electron extracting layers are low cost and have been shown to increase cell stability and performance. Therefore, research into optimising and characterising promising new metal oxide layers which may replace BCP in the future would be preferential to increasing the understanding of the BCP layer in the inverted cells presented in this report.

References

1. *http://www.ipcc.ch/index.htm.*
2. *USA Pat.*, 1946.
3. http://www.nrel.gov/solar/.
4. *http://sharp-world.com/corporate/news/120531.html.*
5. F. T. Kong, S. Y. Dai and K. J. Wang., *Advances in Optoelectronics*, 2007, 75384.
6. L. Y. Han, A. Islam, H. Chen, C. Malapaka, B. Chiranjeevi, S. F. Zhang, X. D. Yang and M. Yanagida, *Energy & Environmental Science*, 2012, **5**, 6057-6060.
7. P. Docampo, S. Guldin, M. Stefik, P. Tiwana, M. C. Orilall, S. Huttner, H. Sai, U. Wiesner, U. Steiner and H. J. Snaith, *Advanced Functional Materials*, 2010, **20**, 1787-1796.
8. N. Espinosa, M. Hosel, D. Angmo and F. C. Krebs, *Energy & Environmental Science*, 2012, **5**, 5117-5132.
9. H. Kallmann and M. Pope, *J. Chem. Phys.*, 1959, **30**, 585.
10. A. K. Ghosh and T. Feng, *Journal of Applied Physics*, 1978, **49**, 5982-5989.
11. C. W. Tang, *Applied Physics Letters*, 1986, **48**, 183-185.
12. H. W. Kroto, J. R. Heath, S. C. Obrien, R. F. Curl and R. E. Smalley, *Nature*, 1985, **318**, 162-163.
13. P. Peumans and S. R. Forrest, *Applied Physics Letters*, 2001, **79**, 126-128.
14. C. W. Chu, Y. Shao, V. Shrotriya and Y. Yang, *Applied Physics Letters*, 2005, **86**, 243506.
15. S. Yoo, B. Domercq and B. Kippelen, *Applied Physics Letters*, 2004, **85**, 5427-5429.
16. R. F. Bailey-Salzman, B. P. Rand and S. R. Forrest, *Applied Physics Letters*, 2007, **91**, 013508.
17. V. Steinmann, N. M. Kronenberg, M. R. Lenze, S. M. Graf, D. Hertel, K. Meerholz, H. Buerckstuemmer, E. V. Tulyakova and F. Wuerthner, *Advanced Energy Materials*, 2011, **1**, 888-893.
18. G. Wei, S. Wang, K. Sun, M. E. Thompson and S. R. Forrest, *Advanced Energy Materials*, 2011, **1**, 184.
19. J. L. Yang, S. Schumann, R. A. Hatton and T. S. Jones, *Organic Electronics*, 2010, **11**, 1399-1402.
20. N. Beaumont, S. W. Cho, P. Sullivan, D. Newby, K. E. Smith and T. S. Jones, *Advanced Functional Materials*, 2012, **22**, 561-566.
21. P. Sullivan, A. Duraud, I. Hancox, N. Beaumont, G. Mirri, J. H. R. Tucker, R. A. Hatton, M. Shipman and T. S. Jones, *Advanced Energy Materials*, 2011, **1**, 352-355.
22. S. Uchida, J. G. Xue, B. P. Rand and S. R. Forrest, *Applied Physics Letters*, 2004, **84**, 4218-4220.
23. S. E. Shaheen, C. J. Brabec, N. S. Sariciftci, F. Padinger, T. Fromherz and J. C. Hummelen, *Applied Physics Letters*, 2001, **78**, 841-843.
24. M. Hiramoto, M. Suezaki and M. Yokoyama, *Chemistry Letters*, 1990, 327-330.

25.   J. G. Xue, S. Uchida, B. P. Rand and S. R. Forrest, *Applied Physics Letters*, 2004, **85**, 5757-5759.
26.   D. Cheyns, B. P. Rand and P. Heremans, *Applied Physics Letters*, 2010, **97**, 033301.
27.   *http://www.heliatek.com*.
28.   G. Yu, J. Gao, J. C. Hummelen, F. Wudl and A. J. Heeger, *Science*, 1995, **270**, 1789-1791.
29.   J. J. M. Halls, C. A. Walsh, N. C. Greenham, E. A. Marseglia, R. H. Friend, S. C. Moratti and A. B. Holmes, *Nature*, 1995, **376**, 498-500.
30.   M. D. Irwin, B. Buchholz, A. W. Hains, R. P. H. Chang and T. J. Marks, *Proceedings of the National Academy of Sciences of the United States of America*, 2008, **105**, 2783-2787.
31.   P. Schilinsky, C. Waldauf and C. J. Brabec, *Applied Physics Letters*, 2002, **81**, 3885-3887.
32.   G. Li, V. Shrotriya, Y. Yao and Y. Yang, *Journal of Applied Physics*, 2005, **98**, 043704.
33.   Y. Kim, S. A. Choulis, J. Nelson, D. D. C. Bradley, S. Cook and J. R. Durrant, *Applied Physics Letters*, 2005, **86**, 063502.
34.   A. J. Moule and K. Meerholz, *Advanced Materials*, 2008, **20**, 240-+.
35.   J. Y. Kim, S. H. Kim, H. H. Lee, K. Lee, W. L. Ma, X. Gong and A. J. Heeger, *Advanced Materials*, 2006, **18**, 572-576.
36.   G. Li, R. Zhu and Y. Yang, *Nature Photonics*, 2012, **6**, 153-161.
37.   B. P. Rand, J. Genoe, P. Heremans and J. Poortmans, *Progress in Photovoltaics*, 2007, **15**, 659-676.
38.   P. Atkins and J. de Paula, *Atkins' Physical Chemistry Seventh Ed.*, Oxford University Press, 2002.
39.   A. W. Hains, Z. Liang, M. A. Woodhouse and B. A. Gregg, *Chemical Reviews*, 2010, **110**, 6689-6735.
40.   J.-L. Bredas, J. E. Norton, J. Cornil and V. Coropceanu, *Accounts of Chemical Research*, 2009, **42**, 1691-1699.
41.   P. K. Nayak, G. Garcia-Belmonte, A. Kahn, J. Bisquert and D. Cahen, *Energy & Environmental Science*, 2012, **5**, 6022-6039.
42.   P. Sullivan, T. S. Jones, A. J. Ferguson and S. Heutz, *Applied Physics Letters*, 2007, **91**, 233114.
43.   P. Heremans, D. Cheyns and B. P. Rand, *Accounts of Chemical Research*, 2009, **42**, 1740-1747.
44.   M. Riede, T. Mueller, W. Tress, R. Schueppel and K. Leo, *Nanotechnology*, 2008, **19**, 424001.
45.   B. A. Gregg and M. C. Hanna, *Journal of Applied Physics*, 2003, **93**, 3605-3614.
46.   S. E. Gledhill, B. Scott and B. A. Gregg, *Journal of Materials Research*, 2005, **20**, 3167-3179.
47.   A. J. Heeger, *Chemical Society Reviews*, 2010, **39**, 2354-2371.
48.   R. Pacios, J. Nelson, D. D. C. Bradley, T. Virgili, G. Lanzani and C. J. Brabec, *Journal of Physics-Condensed Matter*, 2004, **16**, 8105-8116.
49.   R. Steim, F. R. Kogler and C. J. Brabec, *Journal of Materials Chemistry*, 2010, **20**, 2499-2512.
50.   L.-M. Chen, Z. Xu, Z. Hong and Y. Yang, *Journal of Materials Chemistry*, 2010, **20**, 2575-2598.

51.   J. H. Park, T.-W. Lee, B.-D. Chin, D. H. Wang and O. O. Park, *Macromolecular Rapid Communications*, 2010, **31**, 2095-2108.

52.   R. Po, C. Carbonera, A. Bernardi and N. Camaioni, *Energy & Environmental Science*, 2011, **4**, 285-310.

53.   E. L. Ratcliff, B. Zacher and N. R. Armstrong, *Journal of Physical Chemistry Letters*, 2011, **2**, 1337-1350.

54.   S. Braun, W. R. Salaneck and M. Fahlman, *Advanced Materials*, 2009, **21**, 1450-1472.

55.   S. Braun, W. Osikowicz, Y. Wang and W. R. Salaneck, *Organic Electronics*, 2007, **8**, 14-20.

56.   J. Nelson, *The Physics of Solar Cells*, Imperial College Press, 2004.

57.   R. M. Cook, L.-J. Pegg, S. L. Kinnear, O. S. Hutter, R. J. H. Morris and R. A. Hatton, *Advanced Energy Materials*, 2011, **1**, 440-447.

58.   A. Crispin, X. Crispin, M. Fahlman, M. Berggren and W. R. Salaneck, *Applied Physics Letters*, 2006, **89**, 213503.

59.   V. D. Mihailetchi, P. W. M. Blom, J. C. Hummelen and M. T. Rispens, *Journal of Applied Physics*, 2003, **94**, 6849-6854.

60.   Y. Hirose, A. Kahn, V. Aristov and P. Soukiassian, *Applied Physics Letters*, 1996, **68**, 217-219.

61.   F. C. Krebs, J. E. Carle, N. Cruys-Bagger, M. Andersen, M. R. Lilliedal, M. A. Hammond and S. Hvidt, *Solar Energy Materials and Solar Cells*, 2005, **86**, 499-516.

62.   M. O. Reese, M. S. White, G. Rumbles, D. S. Ginley and S. E. Shaheen, *Applied Physics Letters*, 2008, **92**, 053307.

63.   C. J. Brabec, S. E. Shaheen, C. Winder, N. S. Sariciftci and P. Denk, *Applied Physics Letters*, 2002, **80**, 1288-1290.

64.   G. Li, C. W. Chu, V. Shrotriya, J. Huang and Y. Yang, *Applied Physics Letters*, 2006, **88**, 253503.

65.   H.-H. Liao, L.-M. Chen, Z. Xu, G. Li and Y. Yang, *Applied Physics Letters*, 2008, **92**, 173303.

66.   J. Li, S. Kim, S. Edington, J. Nedy, S. Cho, K. Lee, A. J. Heeger, M. C. Gupta and J. T. Yates Jr, *Solar Energy Materials and Solar Cells*, 2011, **95**, 1123-1130.

67.   S. Schumann, R. Da Campo, B. Illy, A. C. Cruickshank, M. A. McLachlan, M. P. Ryan, D. J. Riley, D. W. McComb and T. S. Jones, *Journal of Materials Chemistry*, 2011, **21**, 2381-2386.

68.   H. Kim, J. H. Seo and S. Cho, *Applied Physics Letters*, 2011, **99**, 213302.

69.   C. Waldauf, M. Morana, P. Denk, P. Schilinsky, K. Coakley, S. A. Choulis and C. J. Brabec, *Applied Physics Letters*, 2006, **89**, 233517.

70.   S. H. Park, A. Roy, S. Beaupre, S. Cho, N. Coates, J. S. Moon, D. Moses, M. Leclerc, K. Lee and A. J. Heeger, *Nature Photonics*, 2009, **3**, 297-U295.

71.   B.-Y. Yu, A. Tsai, S.-P. Tsai, K.-T. Wong, Y. Yang, C.-W. Chu and J.-J. Shyue, *Nanotechnology*, 2008, **19**, 255202.

72.   P. Peumans, V. Bulovic and S. R. Forrest, *Applied Physics Letters*, 2000, **76**, 2650-2652.

73.   B. P. Rand, J. Li, J. G. Xue, R. J. Holmes, M. E. Thompson and S. R. Forrest, *Advanced Materials*, 2005, **17**, 2714-+.

74.   H. Gommans, B. Verreet, B. P. Rand, R. Muller, J. Poortmans, P. Heremans and J. Genoe, *Advanced Functional Materials*, 2008, **18**, 3686-3691.

75.   Q. L. Song, F. Y. Li, H. Yang, H. R. Wu, X. Z. Wang, W. Zhou, J. M. Zhao, X. M. Ding, C. H. Huang and X. Y. Hou, *Chemical Physics Letters*, 2005, **416**, 42-46.

76.   N. R. Armstrong, P. A. Veneman, E. Ratcliff, D. Placencia and M. Brumbach, *Accounts of Chemical Research*, 2009, **42**, 1748-1757.

77.   S. Schaefer, A. Petersen, T. A. Wagner, R. Kniprath, D. Lingenfelser, A. Zen, T. Kirchartz, B. Zimmermann, U. Wuerfel, X. Feng and T. Mayer, *Physical Review B*, 2011, **83**, 165311.

78.   J. C. Scott, J. H. Kaufman, P. J. Brock, R. DiPietro, J. Salem and J. A. Goitia, *Journal of Applied Physics*, 1996, **79**, 2745-2751.

79.   F. C. Krebs and K. Norrman, *Progress in Photovoltaics*, 2007, **15**, 697-712.

80.   M. Jorgensen, K. Norrman and F. C. Krebs, *Solar Energy Materials and Solar Cells*, 2008, **92**, 686-714.

81.   P. Sullivan and T. S. Jones, *Organic Electronics*, 2008, **9**, 656-660.

82.   Z. Yu, L. Li, Q. Zhang, W. Hu and Q. Pei, *Advanced Materials*, 2011, **23**, 4453-+.

83.   H. M. Stec, R. J. Williams, T. S. Jones and R. A. Hatton, *Advanced Functional Materials*, 2011, **21**, 1709-1716.

84.   G. B. Murdoch, S. Hinds, E. H. Sargent, S. W. Tsang, L. Mordoukhovski and Z. H. Lu, *Applied Physics Letters*, 2009, **94**, 213301.

85.   L. S. Roman, W. Mammo, L. A. A. Pettersson, M. R. Andersson and O. Inganas, *Advanced Materials*, 1998, **10**, 774-777.

86.   Y. Kim, A. M. Ballantyne, J. Nelson and D. D. C. Bradley, *Organic Electronics*, 2009, **10**, 205-209.

87.   T.-W. Lee and Y. Chung, *Advanced Functional Materials*, 2008, **18**, 2246-2252.

88.   M. M. de Kok, M. Buechel, S. I. E. Vulto, P. van de Weijer, E. A. Meulenkamp, S. de Winter, A. J. G. Mank, H. J. M. Vorstenbosch, C. H. L. Weijtens and V. van Elsbergen, *Physica Status Solidi a-Applied Research*, 2004, **201**, 1342-1359.

89.   F. Nuesch, G. Tornare, L. Zuppiroli, F. S. Meng, K. C. Chen and H. Tian, *Solar Energy Materials and Solar Cells*, 2005, **87**, 817-824.

90.   I. Yoo, M. Lee, C. Lee, D. W. Kim, I. S. Moon and D. H. Hwang, *Synthetic Metals*, 2005, **153**, 97-100.

91.   J. S. Huang, P. F. Miller, J. S. Wilson, A. J. de Mello, J. C. de Mello and D. D. C. Bradley, *Advanced Functional Materials*, 2005, **15**, 290-296.

92.   H. K. Lee, J.-K. Kim and O. O. Park, *Organic Electronics*, 2009, **10**, 1641-1644.

93.   Y. Zhou, Y. Yuan, J. Lian, J. Zhang, H. Pang, L. Cao and X. Zhou, *Chemical Physics Letters*, 2006, **427**, 394-398.

94.   F. L. Zhang, A. Gadisa, O. Inganas, M. Svensson and M. R. Andersson, *Applied Physics Letters*, 2004, **84**, 3906-3908.

95.   M. S. Kim, S. K. Park, Y.-H. Kim, J. W. Kang and J.-I. Han, *Journal of the Electrochemical Society*, 2009, **156**, H782-H785.

96.   F.-C. Chen, J.-L. Wu, C.-L. Lee, Y. Hong, C.-H. Kuo and M. H. Huang, *Applied Physics Letters*, 2009, **95**, 013305.

97.   B. Yin, Q. Liu, L. Yang, X. Wu, Z. Liu, Y. Hua, S. Yin and Y. Chen, *Journal of Nanoscience and Nanotechnology*, 2010, **10**, 1934-1938.

98.   M. P. de Jong, L. J. van Ijzendoorn and M. J. A. de Voigt, *Applied Physics Letters*, 2000, **77**, 2255-2257.

99. J. Ni, H. Yan, A. C. Wang, Y. Yang, C. L. Stern, A. W. Metz, S. Jin, L. Wang, T. J. Marks, J. R. Ireland and C. R. Kannewurf, *Journal of the American Chemical Society*, 2005, **127**, 5613-5624.

100. K. Kawano, R. Pacios, D. Poplavskyy, J. Nelson, D. D. C. Bradley and J. R. Durrant, *Solar Energy Materials and Solar Cells*, 2006, **90**, 3520-3530.

101. R. Pacios, A. J. Chatten, K. Kawano, J. R. Durrant, D. D. C. Bradley and J. Nelson, *Advanced Functional Materials*, 2006, **16**, 2117-2126.

102. S. Khodabakhsh, B. M. Sanderson, J. Nelson and T. S. Jones, *Advanced Functional Materials*, 2006, **16**, 95-100.

103. A. Sharma, A. Haldi, W. J. Potscavage, Jr., P. J. Hotchkiss, S. R. Marder and B. Kippelen, *Journal of Materials Chemistry*, 2009, **19**, 5298-5302.

104. K. Sarangerel, C. Ganzorig, M. Fujihira, M. Sakomura and K. Ueda, *Chemistry Letters*, 2008, **37**, 778-779.

105. N. Beaumont, I. Hancox, P. Sullivan, R. A. Hatton and T. S. Jones, *Energy & Environmental Science*, 2011, **4**, 1708-1711.

106. K. J. Reynolds, J. A. Barker, N. C. Greenham, R. H. Friend and G. L. Frey, *Journal of Applied Physics*, 2002, **92**, 7556-7563.

107. V. Shrotriya, G. Li, Y. Yao, C. W. Chu and Y. Yang, *Applied Physics Letters*, 2006, **88**, 073508.

108. C. G. Claessens, U. Hahn and T. Torres, *Chemical Record*, 2008, **8**, 75-97.

109. K. L. Mutolo, E. I. Mayo, B. P. Rand, S. R. Forrest and M. E. Thompson, *Journal of the American Chemical Society*, 2006, **128**, 8108-8109.

110. S. W. Cho, L. F. J. Piper, A. DeMasi, A. R. H. Preston, K. E. Smith, K. V. Chauhan, P. Sullivan, R. A. Hatton and T. S. Jones, *Journal of Physical Chemistry C*, 2010, **114**, 1928-1933.

111. T. Howells, E. New, P. Sullivan and T. S. Jones, *Advanced Energy Materials*, 2011, **1**, 1085-1088.

112. D. Y. Kim, J. Subbiah, G. Sarasqueta, F. So, H. J. Ding, Irfan and Y. L. Gao, *Applied Physics Letters*, 2009, **95**, 093304.

113. I. Hancox, K. V. Chauhan, P. Sullivan, R. A. Hatton, A. Moshar, C. P. A. Mulcahy and T. S. Jones, *Energy & Environmental Science*, 2010, **3**, 107-110.

114. A. Meller and A. Ossko, *Monatshefte Fur Chemie*, 1972, **103**, 150-&.

115. T. Torres, *Angewandte Chemie-International Edition*, 2006, **45**, 2834-2837.

116. C. G. Claessens, D. Gonzalez-Rodriguez and T. Torres, *Chemical Reviews*, 2002, **102**, 835-853.

117. H. Gommans, D. Cheyns, T. Aernouts, C. Girotto, J. Poortmans and P. Heremans, *Advanced Functional Materials*, 2007, **17**, 2653-2658.

118. P. Sullivan, S. Heutz, S. M. Schultes and T. S. Jones, *Applied Physics Letters*, 2004, **84**, 1210-1212.

119. P. Y. Stakhira, V. V. Cherpak and D. Y. Volynyuk, *Semiconductors*, 2009, **43**, 192-196.

120. M. Kitamura and Y. Arakawa, *Journal of Physics-Condensed Matter*, 2008, **20**, 184011.

121. J. C. Bernede, L. Cattin, S. O. Djobo, M. Morsli, S. R. B. Kanth, S. Patil, P. Leriche, J. Roncali, A. Godoy, F. R. Diaz and M. A. del Valle, *Physica Status Solidi a-Applications and Materials Science*, 2011, **208**, 1989-1994.

122. J. N. Haddock, X. H. Zhang, B. Domercq and B. Kippelen, *Organic Electronics*, 2005, **6**, 182-187.

123. Y. Kim, M. Shin, I. Lee, H. Kim and S. Heutz, *Applied Physics Letters*, 2008, **92**, 093306.
124. J. Y. Kim, K. Lee, N. E. Coates, D. Moses, T.-Q. Nguyen, M. Dante and A. J. Heeger, *Science*, 2007, **317**, 222-225.
125. P. G. Nicholson and F. A. Castro, *Nanotechnology*, 2010, **21**, 492001.
126. P. J. Brown, D. S. Thomas, A. Kohler, J. S. Wilson, J. S. Kim, C. M. Ramsdale, H. Sirringhaus and R. H. Friend, *Physical Review B*, 2003, **67**, 064203.
127. Y. Kim, S. Cook, S. M. Tuladhar, S. A. Choulis, J. Nelson, J. R. Durrant, D. D. C. Bradley, M. Giles, I. McCulloch, C. S. Ha and M. Ree, *Nature Materials*, 2006, **5**, 197-203.
128. H. Sirringhaus, N. Tessler and R. H. Friend, *Science*, 1998, **280**, 1741-1744.
129. R. F. Salzman, J. G. Xue, B. P. Rand, A. Alexander, M. E. Thompson and S. R. Forrest, *Organic Electronics*, 2005, **6**, 242-246.
130. W. L. Leong, G. C. Welch, L. G. Kaake, C. J. Takacs, Y. Sun, G. C. Bazan and A. J. Heeger, *Chemical Science*, 2012, **3**, 2103-2109.
131. S. R. Forrest, *Chemical Reviews*, 1997, **97**, 1793-1896.
132. M. Campione, M. Cartotti, E. Pinotti, A. Sassella and A. Borghesi, *Journal of Vacuum Science & Technology A*, 2004, **22**, 482-486.
133. R. Gutzler, W. M. Heckl and M. Lackinger, *Review of Scientific Instruments*, 2010, **81**, 015108.
134. L.-J. Pegg, S. Schumann and R. A. Hatton, *Acs Nano*, 2010, **4**, 5671-5678.
135. V. Shrotriya, G. Li, Y. Yao, T. Moriarty, K. Emery and Y. Yang, *Advanced Functional Materials*, 2006, **16**, 2016-2023.
136. B. P. Rand, D. P. Burk and S. R. Forrest, *Physical Review B*, 2007, **75**.
137. C. Uhrich, D. Wynands, S. Olthof, M. K. Riede, K. Leo, S. Sonntag, B. Maennig and M. Pfeiffer, *Journal of Applied Physics*, 2008, **104**, 043107.
138. J. D. Servaites, M. A. Ratner and T. J. Marks, *Energy & Environmental Science*, 2011, **4**, 4410-4422.
139. L. Kronik and Y. Shapira, *Surface and Interface Analysis*, 2001, **31**, 954-965.
140. H. Ishii, K. Sugiyama, E. Ito and K. Seki, *Advanced Materials*, 1999, **11**, 605-+.
141. D. Cahen and A. Kahn, *Advanced Materials*, 2003, **15**, 271-277.
142. R. Paynter, INRS-'Energie', Editon edn.
143. D. Briggs and J. T. Grant, *Surface Analysis by Auger and X-ray Photoelectron Spectroscopy*, IM Publications, Chichester, 2003.
144. D. A. Shirley, *Physical Review B*, 1972, **5**, 4709.
145. G. Binnig, C. F. Quate and C. Gerber, *Physical Review Letters*, 1986, **56**, 930-933.
146. L. S. C. Pingree, O. G. Reid and D. S. Ginger, *Nano Letters*, 2009, **9**, 2946-2952.
147. Y. Kinoshita, R. Takenaka and H. Murata, *Applied Physics Letters*, 2008, **92**, 243309.
148. L. Shen, S. Ruan, W. Guo, F. Meng and W. Chen, *Solar Energy Materials and Solar Cells*, 2012, **97**, 59-63.
149. M. C. Gwinner, R. Di Pietro, Y. Vaynzof, K. J. Greenberg, P. K. H. Ho, R. H. Friend and H. Sirringhaus, *Advanced Functional Materials*, 2011, **21**, 1432-1441.
150. K. V. Chauhan, P. Sullivan, J. L. Yang and T. S. Jones, *Journal of Physical Chemistry C*, 2010, **114**, 3304-3308.

151. G. L. Frey, K. J. Reynolds and R. H. Friend, *Advanced Materials*, 2002, **14**, 265-+.

152. N. Li, B. E. Lassiter, R. R. Lunt, G. Wei and S. R. Forrest, *Applied Physics Letters*, 2009, **94**, 023307.

153. D. W. Zhao, S. T. Tan, L. Ke, P. Liu, A. K. K. Kyaw, X. W. Sun, G. Q. Lo and D. L. Kwong, *Solar Energy Materials and Solar Cells*, 2010, **94**, 985-991.

154. C.-H. Chou, W. L. Kwan, Z. Hong, L.-M. Chen and Y. Yang, *Advanced Materials*, 2011, **23**, 1282-+.

155. E. L. Ratcliff, J. Meyer, K. X. Steirer, A. Garcia, J. J. Berry, D. S. Ginley, D. C. Olson, A. Kahn and N. R. Armstrong, *Chemistry of Materials*, 2011, **23**, 4988-5000.

156. N. E. Widjonarko, E. L. Ratcliff, C. L. Perkins, A. K. Sigdel, A. Zakutayev, P. F. Ndione, D. T. Gillaspie, D. S. Ginley, D. C. Olson and J. J. Berry, *Thin Solid Films*, 2012, **520**, 3813-3818.

157. K. Kanai, K. Koizumi, S. Ouchi, Y. Tsukamoto, K. Sakanoue, Y. Ouchi and K. Seki, *Organic Electronics*, 2010, **11**, 188-194.

158. C.-I. Wu, C.-T. Lin, G.-R. Lee, T.-Y. Cho, C.-C. Wu and T.-W. Pi, *Journal of Applied Physics*, 2009, **105**, 033717.

159. M. Vasilopoulou, G. Papadimitropoulos, L. C. Palilis, D. G. Georgiadou, P. Argitis, S. Kennou, I. Kostis, N. Vourdas, N. A. Stathopoulos and D. Davazoglou, *Organic Electronics*, 2012, **13**, 796-806.

160. Irfan, H. Ding, Y. Gao, D. Y. Kim, J. Subbiah and F. So, *Applied Physics Letters*, 2010, **96**, 073304.

161. J. Meyer, A. Shu, M. Kroeger and A. Kahn, *Applied Physics Letters*, 2010, **96**, 133308.

162. Y. Sun, C. J. Takacs, S. R. Cowan, J. H. Seo, X. Gong, A. Roy and A. J. Heeger, *Advanced Materials*, 2011, **23**, 2226-+.

163. M. Kroeger, S. Hamwi, J. Meyer, T. Riedl, W. Kowalsky and A. Kahn, *Applied Physics Letters*, 2009, **95**, 123301.

164. S. R. Hammond, J. Meyer, N. E. Widjonarko, P. F. Ndione, A. K. Sigdel, A. Garcia, A. Miedaner, M. T. Lloyd, A. Kahn, D. S. Ginley, J. J. Berry and D. C. Olson, *Journal of Materials Chemistry*, 2012, **22**, 3249-3254.

165. C. Girotto, E. Voroshazi, D. Cheyns, P. Heremans and B. P. Rand, *Acs Applied Materials & Interfaces*, 2011, **3**, 3244-3247.

166. J. Gao, C. L. Perkins, J. M. Luther, M. C. Hanna, H.-Y. Chen, O. E. Semonin, A. J. Nozik, R. J. Ellingson and M. C. Beard, *Nano Letters*, 2011, **11**, 3263-3266.

167. J.-P. Yang, Y. Xiao, Y.-H. Deng, S. Duhm, N. Ueno, S.-T. Lee, Y.-Q. Li and J.-X. Tang, *Advanced Functional Materials*, 2012, **22**, 600-608.

168. S. Y. Chiam, B. Dasgupta, D. Soler, M. Y. Leung, H. Liu, Z. E. Ooi, L. M. Wong, C. Y. Jiang, K. L. Chang and J. Zhang, *Solar Energy Materials and Solar Cells*, 2012, **99**, 197-203.

169. P.-S. Wang, I. W. Wu, W.-H. Tseng, M.-H. Chen and C.-I. Wu, *Applied Physics Letters*, 2011, **98**, 173302.

170. M. Vasilopoulou, L. C. Palilis, D. G. Georgiadou, P. Argitis, S. Kennou, L. Sygellou, I. Kostis, G. Papadimitropoulos, N. Konofaos, A. A. Iliadis and D. Davazoglou, *Applied Physics Letters*, 2011, **98**, 123301.

171. M. Vasilopoulou, L. C. Palilis, D. G. Georgiadou, S. Kennou, I. Kostis, D. Davazoglou and P. Argitis, *Applied Physics Letters*, 2012, **100**, 013311.

172. J. Subbiah, D. Y. Kim, M. Hartel and F. So, *Applied Physics Letters*, 2010, **96**, 063303.
173. Irfan, H. Ding, Y. Gao, C. Small, D. Y. Kim, J. Subbiah and F. So, *Applied Physics Letters*, 2010, **96**, 243307.
174. C. Kulshreshtha, J. W. Choi, J.-K. Kim, W. S. Jeon, M. C. Suh, Y. Park and J. H. Kwon, *Applied Physics Letters*, 2011, **99**, 023308.
175. P. Peumans, A. Yakimov and S. R. Forrest, *Journal of Applied Physics*, 2003, **93**, 3693-3723.
176. A. Rao, M. W. B. Wilson, J. M. Hodgkiss, S. Albert-Seifried, H. Baessler and R. H. Friend, *Journal of the American Chemical Society*, 2010, **132**.
177. S. W. Cho, L. F. J. Piper, A. DeMasi, A. R. H. Preston, K. E. Smith, K. V. Chauhan, R. A. Hatton and T. S. Jones, *Journal of Physical Chemistry C*, 2010, **114**, 18252 – 18257.
178. E. L. Ratcliff, P. A. Lee and N. R. Armstrong, *Journal of Materials Chemistry*, 2010, **20**, 2672-2679.
179. M. Girtan and M. Rusu, *Solar Energy Materials and Solar Cells*, 2010, **94**, 446-450.
180. C. H. Peters, I. T. Sachs-Quintana, J. P. Kastrop, S. Beaupre, M. Leclerc and M. D. McGehee, *Advanced Energy Materials*, 2011, **1**, 491-494.
181. M. O. Reese, A. J. Morfa, M. S. White, N. Kopidakis, S. E. Shaheen, G. Rumbles and D. S. Ginley, *Solar Energy Materials and Solar Cells*, 2008, **92**, 746-752.
182. Y. Zhou, J. W. Shim, C. Fuentes-Hernandez, A. Sharma, K. A. Knauer, A. J. Giordano, S. R. Marder and B. Kippelen, *Physical Chemistry Chemical Physics*, 2012, **14**, 12014-12021.
183. L.-M. Chen, Z. Hong, G. Li and Y. Yang, *Advanced Materials*, 2009, **21**, 1434-1449.
184. J.-C. Wang, W.-T. Weng, M.-Y. Tsai, M.-K. Lee, S.-F. Horng, T.-P. Perng, C.-C. Kei, C.-C. Yu and H.-F. Meng, *Journal of Materials Chemistry*, 2010, **20**, 862-866.
185. M. Wang, F. Xie, J. Du, Q. Tang, S. Zheng, Q. Miao, J. Chen, N. Zhao and J. B. Xu, *Solar Energy Materials and Solar Cells*, 2011, **95**.
186. S. A. Gevorgyan, M. Jorgensen, F. C. Krebs and K. O. Sylvester-Hvid, *Solar Energy Materials and Solar Cells*, 2011, **95**.
187. M. O. Reese, S. A. Gevorgyan, M. Jorgensen, E. Bundgaard, S. R. Kurtz, D. S. Ginley, D. C. Olson, M. T. Lloyd, P. Moryillo, E. A. Katz, A. Elschner, O. Haillant, T. R. Currier, V. Shrotriya, M. Hermenau, M. Riede, K. R. Kirov, G. Trimmel, T. Rath, O. Inganas, F. Zhang, M. Andersson, K. Tvingstedt, M. Lira-Cantu, D. Laird, C. McGuiness, S. Gowrisanker, M. Pannone, M. Xiao, J. Hauch, R. Steim, D. M. DeLongchamp, R. Roesch, H. Hoppe, N. Espinosa, A. Urbina, G. Yaman-Uzunoglu, J.-B. Bonekamp, A. J. J. M. van Breemen, C. Girotto, E. Voroshazi and F. C. Krebs, *Solar Energy Materials and Solar Cells*, 2011, **95**, 1253-1267.
188. M. Wang, Y. Li, H. Huang, E. D. Peterson, W. Nie, W. Zhou, W. Zeng, W. Huang, G. Fang, N. Sun, X. Zhao and D. L. Carroll, *Applied Physics Letters*, 2011, **98**, 103305.
189. J. Meyer, K. Zilberberg, T. Riedl and A. Kahn, *Journal of Applied Physics*, 2011, **110**, 033710.
190. Q. Chen, B. J. Worfolk, T. C. Hauger, U. Al-Atar, K. D. Harris and J. M. Buriak, *Acs Applied Materials & Interfaces*, 2011, **3**, 3962-3970.

191. W.-T. Chiang, S.-H. Su, Y.-F. Lin and M. Yokoyama, *Japanese Journal of Applied Physics*, 2010, **49**.
192. Z. R. Hong, C. J. Liang, X. Y. Sun and X. T. Zeng, *Journal of Applied Physics*, 2006, **100**, 093711.
193. M. T. Lloyd, C. H. Peters, A. Garcia, I. V. Kauvar, J. J. Berry, M. O. Reese, M. D. McGehee, D. S. Ginley and D. C. Olson, *Solar Energy Materials and Solar Cells*, 2011, **95**.
194. T. T. Larsen-Olsen, E. Bundgaard, K. O. Sylvester-Hvid and F. C. Krebs, *Organic Electronics*, 2011, **12**, 364-371.
195. K. Zilberberg, S. Trost, J. Meyer, A. Kahn, A. Behrendt, D. Luetzenkirchen-Hecht, R. Frahm and T. Riedl, *Advanced Functional Materials*, 2011, **21**, 4776-4783.
196. K. Zilberberg, S. Trost, H. Schmidt and T. Riedl, *Advanced Energy Materials*, 2011, **1**, 377-381.
197. M. Demeter, M. Neumann and W. Reichelt, *Surface Science*, 2000, **454**, 41-44.
198. J. Mendialdua, R. Casanova and Y. Barbaux, *Journal of Electron Spectroscopy and Related Phenomena*, 1995, **71**, 249-261.
199. Q. H. Wu, A. Thissen, W. Jaegermann and M. L. Liu, *Applied Surface Science*, 2004, **236**, 473-478.
200. A. Talledo and C. G. Granqvist, *Journal of Applied Physics*, 1995, **77**, 4655-4666.
201. Q. H. Wu, A. Thissen and W. Jaegermann, *Solid State Ionics*, 2004, **167**, 155-163.